Development and Application of Analysis Methods for Hyperpolarized Carbon-13 Imaging for Quantitative Metabolic Characterization

by

Jasmine Hu

DISSERTATION
Submitted in partial satisfaction of the requirements for degree of
DOCTOR OF PHILOSOPHY
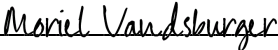
in

Bioengineering

in the

GRADUATE DIVISION

of the

UNIVERSITY OF CALIFORNIA, SAN FRANCISCO
AND
UNIVERSITY OF CALIFORNIA, BERKELEY

Approved:

DocuSigned by:

Danil B Vigneron _____ Daniel Vigneron
DA5485F9C42341E...
                                                                                    Chair

DocuSigned by:

Peder Larson _____ Peder Larson
...941E...

DocuSigned by:

Michael Ohliger _____ Michael Ohliger
...45F...

DocuSigned by:

Moriel Vandsburger _____ Moriel Vandsburger
4FC23D70A4C0458...

_____
                                                                    Committee Members

Dedicated to my family:

Jenny Graham, John Graham, and Bing Hu

Acknowledgments

Contributions

Chapters 4 and 5 are previously published papers cited below. I contributed to the methodology, formal analysis, investigation, data curation, writing, review, and editing of Chapter 4. For Chapter 5 I contributed to the data collection, review, and editing.

Chapter 4:

Jasmine Y Hu, Yaewon Kim, Adam W Autry, Mary M Frost, Robert A Bok, Javier E Villanueva-Meyer, Duan Xu, Yan Li, Peder EZ Larson, Daniel B Vigneron, and Jeremy W Gordon. Kinetic Analysis of Multi-Resolution Hyperpolarized ^{13}C Human Brain MRI to Study Cerebral Metabolism. *Magnetic Resonance in Medicine.* November 2022. DOI: 10.1002/mrm.29354

Chapter 5:

Nikolaj Bøgh, Jeremy W Gordon, Esben SS Hansen, Robert A Bok, Jakob U Blicher, Jasmine Y Hu, Peder EZ Larson, Daniel B Vigneron, and Christoffer Laustsen. Initial Experience on Hyperpolarized [1-^{13}C]Pyruvate MRI Multicenter Reproducibility—Are Multicenter Trials Feasible? *Tomography.* March 2022. DOI: 10.3390/tomography8020048

Abstract

Development and Application of Analysis Methods for Hyperpolarized Carbon-13 Imaging for

Quantitative Metabolic Characterization

Jasmine Hu

Hyperpolarized [1-^{13}C]pyruvate magnetic resonance imaging is a novel imaging modality used to study real-time metabolic conversions in vivo. The ^{13}C label is conserved in downstream metabolites of pyruvate, including lactate and bicarbonate in the brain, and the measurement of these metabolic conversions provides unique measurements of cerebral bioenergetics that can provide biomarkers of brain tumor metabolic reprogramming and response to therapy. Upregulated pyruvate to lactate conversion via glycolysis, known as the Warburg effect, is associated with cancer cell metabolism. Hyperpolarized [1-^{13}C]pyruvate magnetic resonance imaging provides a valuable technique for measuring metabolic activity, but it comes with challenges due to the rapid decay of nonrenewable polarization. Hyperpolarization enhances the signal of [1-^{13}C]pyruvate 10,000-fold compared to thermal equilibrium but the signal decays after pyruvate is taken out of the polarizer according to a decay constant characterized by T_1, which is approximately one minute. This dissertation presents novel and improved analysis methods for hyperpolarized ^{13}C imaging demonstrated in multiple clinical studies, including metabolic quantification of multi-resolution images, reproducible metabolic measurement methods across multiple research sites, and cerebral perfusion measurement using hyperpolarized [1-^{13}C]pyruvate imaging. Further methods to improve the acquisition of hyperpolarized [1-^{13}C]pyruvate imaging are also presented, including the characterization of polarizer quality control statistics, frequency response of spatial-spectral pulses, and the signal effects of reconstructing hyperpolarized [1-^{13}C]pyruvate data with different types of sensitivity maps.

Table of Contents

List of Figures

List of Tables

Chapter 1

Introduction

Magnetic resonance imaging (MRI) is a non-invasive imaging technique that produces detailed images of soft tissues often used for diagnosis and treatment monitoring. Most clinical MRI studies acquire signal from the hydrogen (^{1}H) atom, which is sensitive to magnetic fields and the most abundant atom in the human body. Carbon-13 (^{13}C) signal can also be acquired by MRI and used to measure metabolism, but it has low signal in the human body due to its magnetic properties and low abundance. To enhance ^{13}C magnetic signal and measure metabolism in vivo, ^{13}C enriched molecules can be hyperpolarized (HP) and injected into a human body. The most widely studied ^{13}C molecule in clinical studies to date is [1-^{13}C]pyruvate, which has favorable magnetic properties and is a key molecule in tracking multiple metabolic pathways. Pyruvate to lactate conversion is a measure of glycolysis, which produces cellular energy. Pyruvate to bicarbonate conversion is a measure of oxidative phosphorylation, which is a more efficient method of producing energy than glycolysis. In cancer cells, altered metabolism known as the Warburg effect results in upregulation of the conversion of pyruvate to lactate. HP [1-^{13}C]pyruvate MRI enables the imaging and quantitative measurement of metabolism, which can be used to monitor changes in disease progression and response. This dissertation focuses on the development and application of analysis methods for the quantification of hyperpolarized ^{13}C metabolic MRI.

Chapter 2 provides a background on the principles of magnetic resonance imaging and HP ^{13}C MRI. Chapter 3 and Chapter 4 describe a multi-resolution acquisition approach for HP [1-^{13}C]pyruvate MRI applied in simulation and clinical brain studies respectively. The multi-resolution acquisition

allowed for increased spatial resolution of the injected pyruvate while maintaining adequate signal for lactate and bicarbonate, the downstream metabolites of pyruvate. Increased pyruvate spatial resolution reduced partial volume effects of extracellular HP [1-^{13}C]pyruvate that bias intracellular metabolism measurements.

Chapter 5 describes the first multi-center HP [1-^{13}C]pyruvate MRI brain study that assessed reproducibility of HP [1-^{13}C]pyruvate MRI results across two institutions. Pyruvate-to-lactate conversion (k_{PL}) and the lactate Z-score were the most reproducible metabolic quantification measurements. The results of this study inform the design of future multicenter studies, which are necessary to cement the clinical utility of HP ^{13}C MRI.

Chapter 6 describes the use of high-resolution HP [1-^{13}C]pyruvate MRI to obtain perfusion measurements of the human brain. Pyruvate perfusion metrics were positively correlated to arterial spin labeling (ASL) perfusion metrics, which were used as a standard reference. This study showed that HP [1-^{13}C]pyruvate MRI can be used to assess cerebral metabolism and perfusion within the same study.

Chapter 7 describes further methods to characterize and improve HP ^{13}C MRI acquisition and analysis. This includes the characterization of historical HP pyruvate quality control measurements, which are critical to the successful acquisition of HP ^{13}C MRI. Also important for acquisition is the spatial-spectral (SPSP) excitation pulse, which was redesigned to improve subject comfort by reducing peripheral nerve stimulation. The new SPSP pulse was characterized to ensure the frequency responses match expectations and that the pulse does not have unintended effects like excitation of an undesirable molecule. On the HP analysis side, sensitivity maps were used to

optimally reconstruct images from the multiple MRI coil channels. I experimented with different sensitivity map interpolation methods and orders of processing to identify which of them routinely produces the highest quality HP ^{13}C MR images and that, in turn, facilitates improved measurements of metabolic conversion.

Chapter 2

Background

This chapter provides background information of magnetic resonance imaging and hyperpolarized ^{13}C magnetic resonance imaging.

2.1 Magnetic Resonance Imaging Fundamentals

2.1.1 Spins, Resonance, and Polarization

Magnetic resonance imaging (MRI) is based on atoms with a nonzero nuclear spin angular momentum. This spin arises from an odd number of protons or neutrons and gives rise to a magnetic moment. These magnetic-sensitive nuclei, also called "spins", have a net magnetic moment of zero in the absence of an external magnetic field (Figure 2.1a).
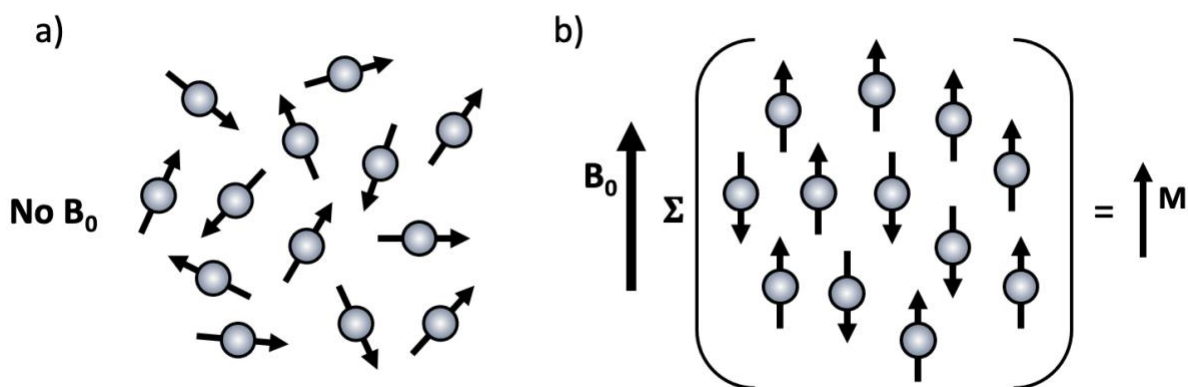
Figure 2.1. Spin magnetic moments with and without an external magnetic field. (a) Spins are randomly oriented in absence of an external field. (b) Spins are oriented in the direction of an external field B_0 resulting in a magnetic moment M.

In an external magnetic field denoted B_0, the spins will tend to align in the direction of B_0, arising in a net magnetic moment M (Figure 2.1b), and the spins will also exhibit resonance at a particular

frequency. This resonance frequency is called the Larmor frequency ω, and it is related to the applied

magnetic field by the gyromagnetic ratio γ.

$$\omega = \gamma B \tag{2.1}$$

The gyromagnetic ratio is a constant value that is specific to each atom. For ^{1}H, the MR sensitive

atom with the highest natural abundance in the human body, $\gamma / 2\pi$ = 42.58 MHz/Tesla. At a

magnetic field strength of 1.0 T, the proton resonance frequency is 42.58 MHz, and at a clinical field

strength of 3.0 T the resonance frequency is 127.74 MHz. ^{13}C is an atom of great biologic interest,

due to carbon forming the basis for organic life, and its gyromagnetic ratio is 10.78 MHz/T which

gives a resonance frequency of 32.34 MHz at 3.0 T. In an external magnetic field, spins will exhibit a

net magnetic moment aligned with the external field and resonate at the Larmor frequency.

The magnetic moment observed in MR signals is comprised of an unequal number of spins oriented

in the parallel (n$^+$) and antiparallel (n$^-$) directions of the external magnetic field. The parallel direction

is lower energy since it is aligned with the external field, and the ratio of the parallel and antiparallel

spin populations is described by the Boltzmann equilibrium.

$$\frac{n^+}{n^-} = e^{\frac{\gamma \hbar B_0}{k_B T}} \tag{2.2}$$

The numerator of the exponent represents the difference in energy between the parallel and

antiparallel spin populations, where γ is the gyromagnetic ratio, $\hbar$ is Planck's constant (1.054 ×

10^{-34} J/s), and B_0 is the external magnetic field. The exponent denominator consists of k_B the

Boltzmann constant (1.381 × 10^{-23} J/K) and T the absolute temperature in Kelvin. This equation can

be transformed to describe polarization at thermal equilibrium P_{th}, which normalizes the net

magnetization by the total number of spins.

$$P_{th} = \frac{n^+ - n^-}{n^+ + n^-} = tanh\left(\frac{\gamma \hbar B_0}{2k_B T}\right) \tag{2.3}$$

These relationships help describe the expected amount of signal in an MR experiment, which is proportional to the number of spins, the gyromagnetic ratio, and the polarization. Polarization is a function of the gyromagnetic ratio, the main field strength, and temperature. This implies that polarization and thus the observable MR signal can be increased by increasing the magnetic field strength and decreasing the temperature.

2.1.2 Relaxation

To observe the spin population, the equilibrium polarization must be excited by a radiofrequency (RF) pulse, after which the spins will relax back to their equilibrium state in the transverse and longitudinal axes. These relaxation processes are described by two time-constants shown in Figure Figure 2.2, T_1 and T_2.
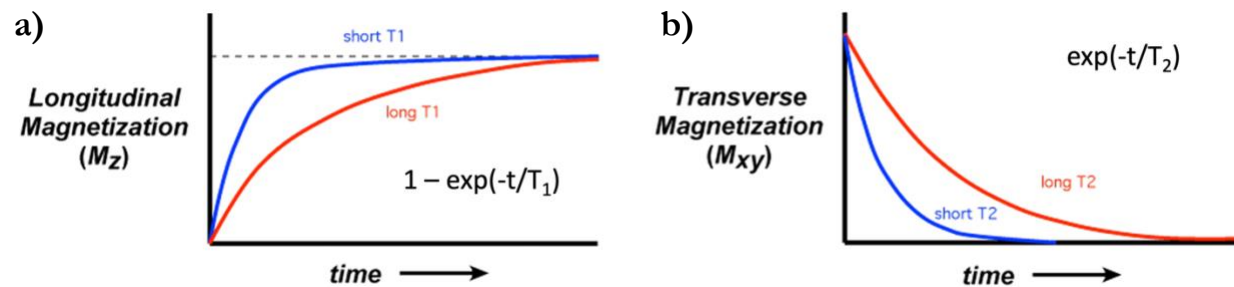
Figure 2.2. Longitudinal and transverse magnetization decay. (a) After excitation tips magnetization into the transverse plane to receive signal, longitudinal magnetization recovers along the z axis characterized by time constant T_1. (b) Transverse magnetization recovers along the xy axes characterized by time constant T_2. Figure adapted from Elster AD[1].

Longitudinal relaxation, also known as T_1 relaxation, is the return of magnetization parallel to the external field. This process involves the transfer of energy from excited spins to nearby nuclei and atoms where the speed of energy transfer, described by T_1, depends on tissue structure and external field strength. T_1 relaxation is the fastest when molecular motion is close to the Larmor frequency. Stronger external fields will increase the Larmor frequency above typical rates of molecular motion, increasing observed T_1 times.

Transverse relaxation or T_2 relaxation is the decay of magnetization perpendicular to the external field. This decay includes both T_1 relaxation, where energy is transferred to the surrounding environment, and dephasing due to local magnetic field disturbances. In an ideal MR experiment with a perfect external field, the local field disturbances would be due to natural interactions of atoms or molecules, such as proximity to an electronegative oxygen atom or diffusion by an iron-containing molecule. In a real MR experiment T_2 decays faster than would be predicted by natural mechanisms due to inhomogeneities in the external magnetic field; this rate is denoted T_2^*.

T_2^* effects can be from defects in the main magnet or from susceptibility-induced field distortions from objects within the field. Magnetic susceptibility is a measure of how much of a material will become magnetized in a magnetic field, which can take the form of either paramagnetism (concentrates the field) or diamagnetism (disperses the field). Certain atoms such as iron and calcium exhibit relatively strong susceptibility effects in a biological context and affect MR signal frequencies.

2.1.3 Bloch Equation

The Bloch equation describes the behavior of magnetization M in a magnetic field B where t is time, $M = [M_x, M_y, M_z]^T$ is the magnetization vector, γ is the gyromagnetic ratio, M_0 is the equilibrium magnetization, i, j, and k are unit vectors in x, y, and z directions respectively, and T_1 and T_2 are the longitudinal and transverse relaxation time constants.

$$\frac{dM}{dt} = M \times \gamma B - \frac{M_x i + M_y j}{T_2} - \frac{(M_z + M_0)k}{T_1} \tag{2.4}$$

The cross-product describes the precession of the magnetization vector about the magnetic field. The magnetic field includes the static external field B_0, RF excitation field B_1, and linear gradient fields G which are described in Section 2.1.4. B_0 is 1,000 times greater in magnitude than the other two fields, so B_0 is the main factor affecting magnetization and relaxation time constants.

2.1.4 RF Excitation and Gradients

Signal can be obtained from spins by exciting them with a RF pulse tuned to the Larmor frequency. This RF pulse, denoted B_1, tips spins out of equilibrium with B_0 and into the xy (transverse) plane where the magnetization can induce a signal in a RF receiver coil (Figure 2.3). The excitation tip amount is described by flip angle θ, which depends on the gyromagnetic ratio and the intensity and duration of B_1 as shown in Equation 2.5.

$$\theta = \int_0^T \gamma B_1 t \, (dt) \tag{2.5}$$
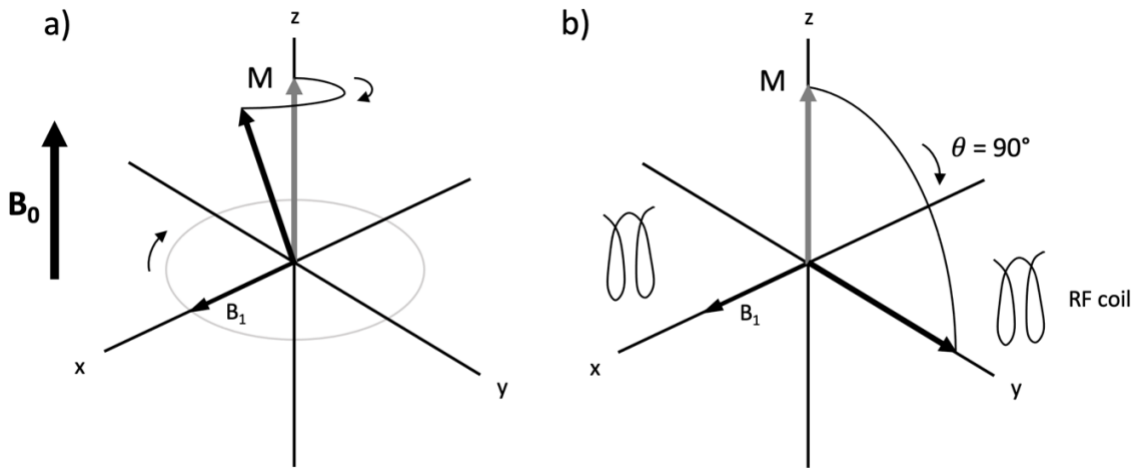
Figure 2.3. Manipulation and reception of a magnetization vector using a radiofrequency pulse and receiver coil. (a) A B_1 radiofrequency (RF) field turned to the Larmor frequency and applied in the transverse (xy) plane tips the magnetization vector M out of equilibrium with the main field B_0. (b) A 90° flip angle is applied, rotating M into the transverse plane where the magnetization can induce a signal in a RF receiver coil. Figure adapted from Nishimura[2].

A 90° flip angle will completely tip the magnetization into the transverse plane and a 180° flip will flip the magnetization vector in the opposite direction of B_0. After the excitation field ends, the spins will relax back to equilibrium with B_0. This magnetic relaxation is described in terms of two time-constants described previously: T_1 for relaxation along the z (longitudinal) axis and T_2 for decay of the magnetization vector in the xy (transverse) plane. In humans, T_1 values are in the range of 100-

2000 ms and T_2 values are 10-300 ms. These time constants are important for MR imaging because they can be used to distinguish different tissues.

A third type of magnetic field is necessary to spatially localize magnetic signals: linear gradient fields. With only B_0 and B_1, the magnetic signals received will be a bulk reading of all the spins at the specified resonance frequency. Linear gradient fields, denoted by G, can be applied along the x, y, and z directions to change the frequency of spins by a function of their spatial location. For example, a linear gradient applied in the x-direction G_x will result in an applied field of $B_0 + G_x x$ and the frequency of the spins becomes $\omega(x) = \gamma(B_0 + G_x x)$. For an object 10 cm wide and $G_x = 10$ mT/m, the frequencies across the object vary as 4.258 kHz/cm for ^{1}H resulting in a frequency bandwidth of 42.58 kHz. A mathematical transformation, called the Fourier transform, from the frequency domain to the spatial domain can then map each frequency to an x-position. This mapping is used in multiple dimensions to acquire MR images.

2.1.5 Spatial Encoding & Sampling

The magnetic field can be purposefully manipulated into an inhomogeneous field to obtain known frequencies, which can be translated to spatial positions using the Fourier transform. The Fourier transform in one dimension is shown in Equation 2.6, where $F(k_x)$ is the frequency spectrum of the function $f(x)$.

$$F(k_x) = \int_{-\infty}^{\infty} f(x)e^{-i2\pi k_x x} \, dx$$
$$= \int_{-\infty}^{\infty} f(x)cos2\pi k_x x \, dx - i \int_{-\infty}^{\infty} f(x)sin2\pi k_x x \, dx \qquad (2.6)$$

The Fourier transform exponent can be decomposed into cosine and sine components as shown in the second line of the equation, which helps "show" the frequencies in the transform.

$$F\left(k_x, k_y\right) = \int_{-\infty}^{\infty} f(x,y)e^{-i2\pi(k_x x + k_y y)} \, dxdy$$

$$= \int_{-\infty}^{\infty} f(x,y)cos2\pi(k_x x + k_y y) \, dxdy - i\int_{-\infty}^{\infty} f(x,y)sin2\pi(k_x x + k_y y) \, dxdy \quad (2.7)$$

The Fourier transform can be extended to two dimensions as shown in Equation 2.7. This representation includes variables k_x and k_y that represent the spatial frequency domain, which is analogous to the spatial domain represented by x and y. The spatial frequency domain is also called k-space. In MRI, these concepts are used to excite spins in a particular spatial location and transform the resulting frequency signals into images. To selectively excite a slice of spins, we can apply a B_1 RF sinc pulse along with a gradient G_z to exite a plane perpendicular to z. The Fourier transform of a sinc function is a rect function, so the sinc pulse selects a rectangular profile of spatial frequencies. To acquire a line within a slice of k-space, gradients Gx and Gy are added to selective excitation as shown in Figure 2.4. The manipulation of gradient amplitude, shape, and timing allow different spatial positions, sampling trajectories, and types of signal contrast to be acquired.

Figure 2.4. Sequence diagram of selective excitation with radiofrequency (RF) excitation, G_z slice selection, and readout of lines in k-space with G_y and G_z.

To form an image from k-space data, enough data needs to be sampled both in terms of resolution and coverage. The spacing of points in k-space (Δk) is inversely related to the field of view (FOV) in image space, and the sample coverage in k-space ($n\Delta k$ where n is the number of samples) is inversely related to the spatial resolution in image space (δ).

$$FOV = \frac{1}{\Delta k} \qquad (2.8)$$

$$\delta = \frac{1}{n\Delta k} \qquad (2.9)$$

To accurately represent signal frequencies, the sampling rate must be at least twice the highest signal frequency according to the Nyquist sampling theorem. If the sampling rate is below the Nyquist rate then incorrect frequency measurements, known as aliasing, occurs (Figure 2.5). Because frequencies are used to encode spatial locations in MRI, aliasing can manifest in the form of image artifacts. For example, when the dimensions of an object exceed the sampled FOV, the image gets folded over in the direction with insufficient sampling. Another type of sampling artifact called Gibbs ringing is due to the use of a limited number of sinusoidal frequencies to represent signals (Figure 2.5). When there is a sharp transition in signal, such as the edges of the brain, the highest frequencies will overshoot the actual signal profile which results in multiple fine parallel lines immediately next to the sharp transition.
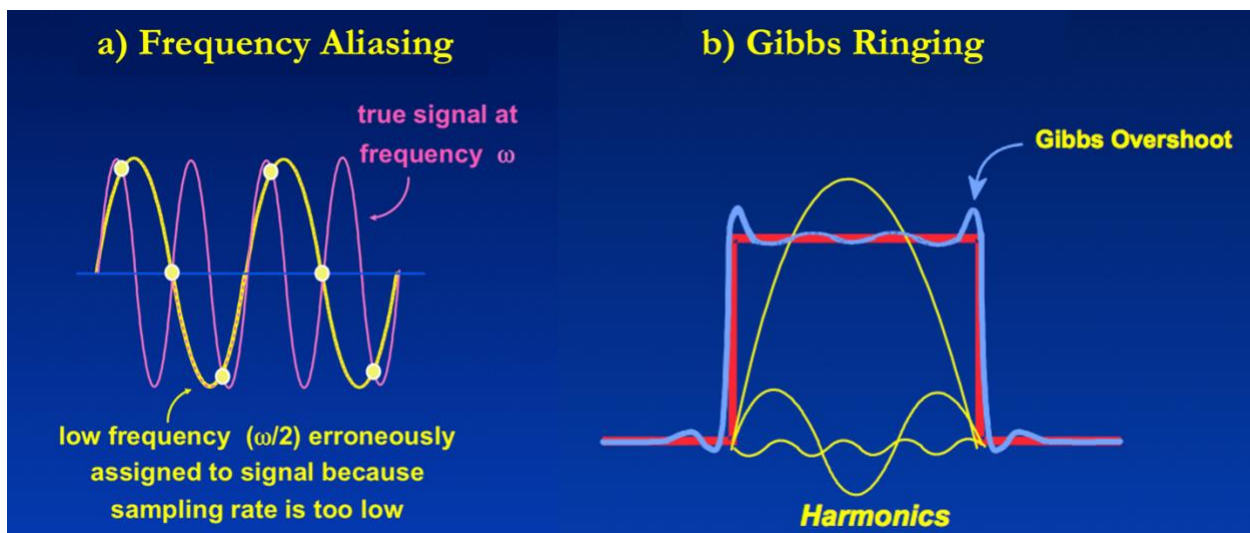
Figure 2.5. Signal artifacts arise from inadequate sampling rates or a limited number of frequency representations. (a) Frequency aliasing occurs when the sampling rate is less than twice the highest signal frequency, which results in incorrect frequency measurement. (b) Gibbs ringing occurs when a limited number of sinusoidal functions are used to represent a sharp transition, which results in overshoots at the signal boundary. Figure adapted from Elster AD[1].

2.1.6 Image Contrast

MR imaging uses repeated excitations and gradients, called a sequence, to obtain images. The timing and amplitude of the sequence changes the sensitivity to different parts of the MR signal. Two main sequence parameters include the repetition time (TR), the time between each RF excitation, and echo time (TE), the time from the RF excitation to when the gradients traverse the center of k-space. TR determines the extent of T_1 relaxation, so changing TR modulates the amount of T_1-weighting in the image. The center of k-space provides the bulk of image intensity data from transverse magnetization, so changing TE modulates the amount of T_2-weighting in the image. For example, a spin-echo sequence, which uses 90° and 180° RF pulses to excite and refocus spins into an echo, has image contrast I summarized as:

$$I = Gain * Proton\ Density * [1 - e^{-TR/T_1}] * e^{-TE/T_2} \tag{2.10}$$

For spin echo imaging, short TR and TE result in T_1-weighted images. This is because $e^{-TE/T_2} \approx 1$, so the image contrast will depend on T_1. Long TR and long TE will result in T_2 weighted images since $[1 - e^{-TR/T_1}] \approx 1$ and image contrast will depend more on T_2. Long TR and short TE will result in proton-density weighted images, and short TR and long TE are limited and do not provide good contrast for biological tissues.

2.2 Hyperpolarized ^{13}C Magnetic Resonance Imaging

While conventional MRI focuses on ^{1}H, ^{13}C MRI is sensitive to carbon molecules which are central to almost all metabolic processes. The MR-active ^{13}C isotope has low natural abundance (<1% of all carbon) and low gyromagnetic ratio (1/4 of ^{1}H) so hyperpolarization and concentrated injections are used to boost ^{13}C signal in biological tissues. A typical HP ^{13}C study involves hyperpolarizing a ^{13}C-labeled compound in a polarizer and transferring the polarized compound to the MR scanner for

injection. Once the ^{13}C-labeled compound leaves the polarizer, its polarization will decay irreversibly to thermal equilibrium over a time characterized by the compound's T_1. To be able to image the ^{13}C signal before it decays the T_1 needs to be long enough, which for clinical HP agents is on the order of 1-2 minutes. Fast imaging methods are required to capture the signal of the ^{13}C molecule and its metabolites. After the HP ^{13}C images are acquired, image processing and kinetic modeling are done to quantify metabolism. A summary of the steps of a HP ^{13}C imaging study are shown in Figure 2.6.
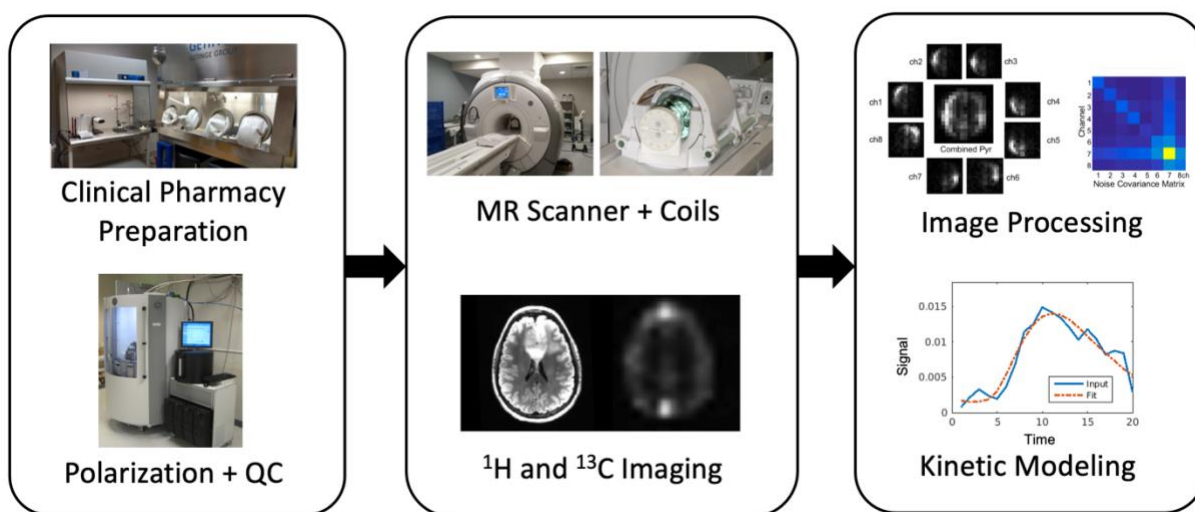
Figure 2.6. Summary of a hyperpolarized ^{13}C MRI study. Quality control is abbreviated as QC. Figure adapted from Crane JC[3].

2.2.1 Hyperpolarization Physics & Methods

Hyperpolarization increases polarization by increasing the proportion of spins aligned with the external magnetic field. As mentioned in Section 2.1.1, polarization is a function of the gyromagnetic ratio, the main field strength, and temperature. Thus, increasing the magnetic field strength and decreasing temperature will increase polarization. In addition to these conditions, a common hyperpolarization method called dynamic nuclear polarization (DNP) transfers polarization from electron spins to nuclear spins. DNP takes advantage of the higher gyromagnetic ratio of electrons in free radicals (28,025 MHz/T, approximately 2,600 times greater than ^{13}C) and uses microwave

irradiation to transfer the polarization to the target nuclei as shown in Figure 2.7. DNP increases ^{13}C

polarization to approximately 40%, over 10,000 times ^{13}C thermal polarization[4].
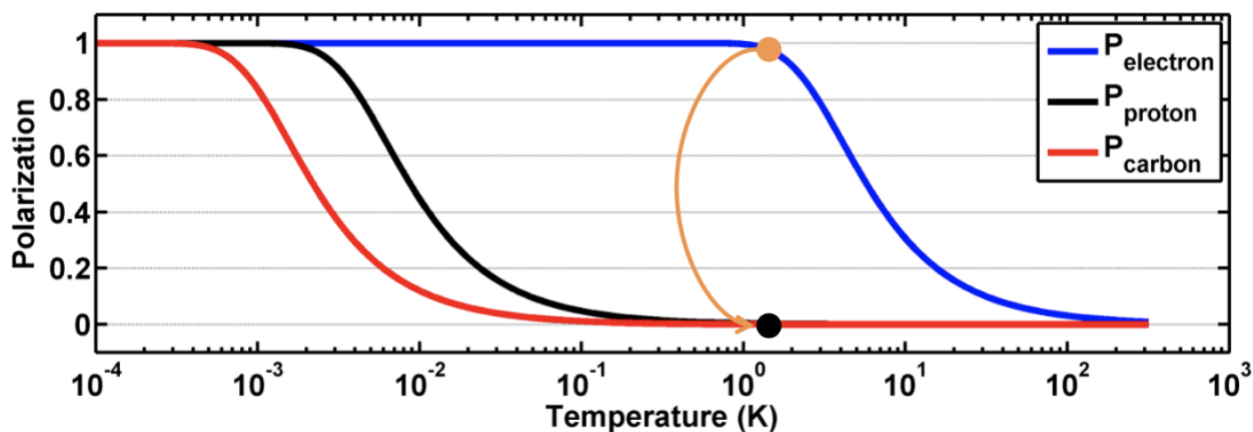
Figure 2.7. Polarization levels for electrons, protons, and carbon nuclei over temperature. The yellow arrow indicates the DNP transfer of polarization from electrons to nuclei using microwave irradiation at high magnetic field strength and low temperature. Used with permission from Gordon JW.

DNP takes place at a temperature near 1 Kelvin, so the hyperpolarized compound is in a solid state.

To obtain an injectable, biologically compatible solution and maintain high levels of polarization, the

hyperpolarized compound is quickly dissolved using superheated water, combined with buffer, and

filtered for free radical molecules before transferring it for injection. To ensure that the

hyperpolarized compound is safe and worth injecting into a subject, a pharmacist verifies quality

control measurements for high ^{13}C-labeled molecule (usually pyruvate) concentration, high

polarization, neutral pH, minimal free radical concentration, near-body temperature, filter integrity,

and sufficient solution volume. If the pH is extreme, free radical concentration too high, solution

temperature too extreme, or filter is not intact then the ^{13}C compound is not safe for injection into a

subject. If pyruvate concentration, polarization or solution volume is low, then the ^{13}C signal would

be under the measurement threshold and the compound would not be worth injecting into a subject.

In addition, the time from dissolution to injection must be minimal (<60 seconds) because as soon

as the hyperpolarized compound is taken out of the polarizer for dissolution, its polarization starts

to decay irreversibly according to its T_1. All the polarization and dissolution steps must be coordinated and efficient to get hyperpolarized ^{13}C compound to the MR scanner.

2.2.2 Acquisition Methods

Once the hyperpolarized ^{13}C compound is at the MR scanner, fast imaging techniques are employed to make use of the decaying ^{13}C signal. Some common trajectories include echo-planar and spiral, which have sufficient k-space coverage to collect multiple metabolite images in three dimensions within 3 seconds. Some additional considerations for HP ^{13}C MRI include efficient RF utilization and imaging multiple metabolites. Because the hyperpolarization is nonrenewable after dissolution, utilization of the magnetization by RF pulses also contributes to signal decay. So small flip angles, in the range of 5° to 30° are common for HP ^{13}C MRI sequences. HP ^{13}C MRI measures metabolism by exciting resonance frequencies specific to the metabolites of interest. These metabolite-specific excitations are possible because of chemical shift, a difference in resonance frequency between nuclei due to differences in their local molecular environments. Each atom has electrons circulating around a nucleus, which produces a local magnetic field that opposes the external magnetic field. Nuclei on the same molecule will experience the local fields of each other, slightly changing their resonance frequencies based on geometry and type of nucleus. A single molecule will have a frequency "signature" based on the shifted frequencies of its nuclei. Bringing together all these considerations, a spectral-spatial RF pulse combined with echo-planar imaging (EPI) was used for the HP ^{13}C MRI studies in this dissertation.
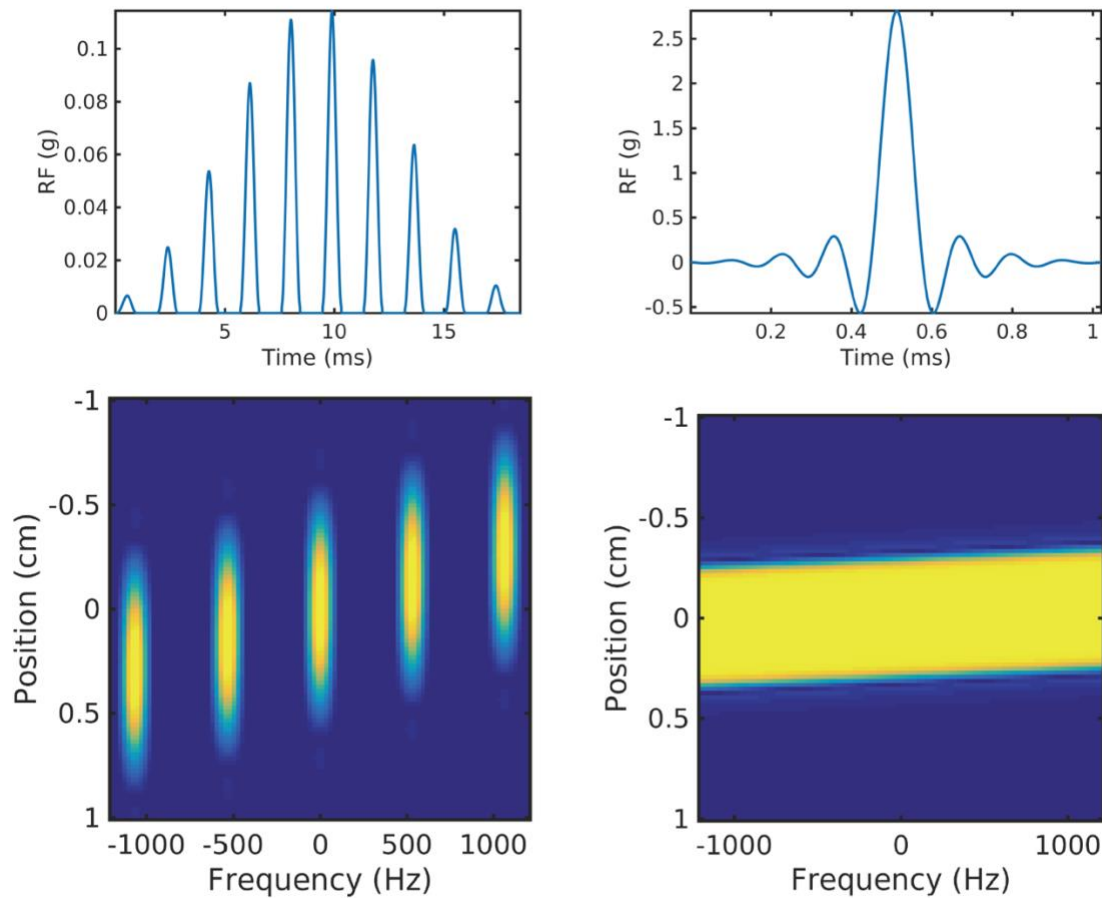
Figure 2.8. Two components of a spectral-spatial pulse. The spectral component is the inner frequency while the spatial component of the RF pulse is encoded in the pulse envelope. Used with permission from Gordon JW.

As shown in Figure 2.7, spatial-spectral pulses are designed to select specific spectral and spatial frequencies that correspond to the metabolite frequencies of interest. This pulse is combined with symmetric EPI as shown in Figure 2.8 for a sequence that can select multiple metabolites and collect sufficient k-space data within one RF excitation. In addition, the acquired resolution for each metabolite can be varied using scaled amplitudes of the readout gradients[5] as shown in Figure 2.9.
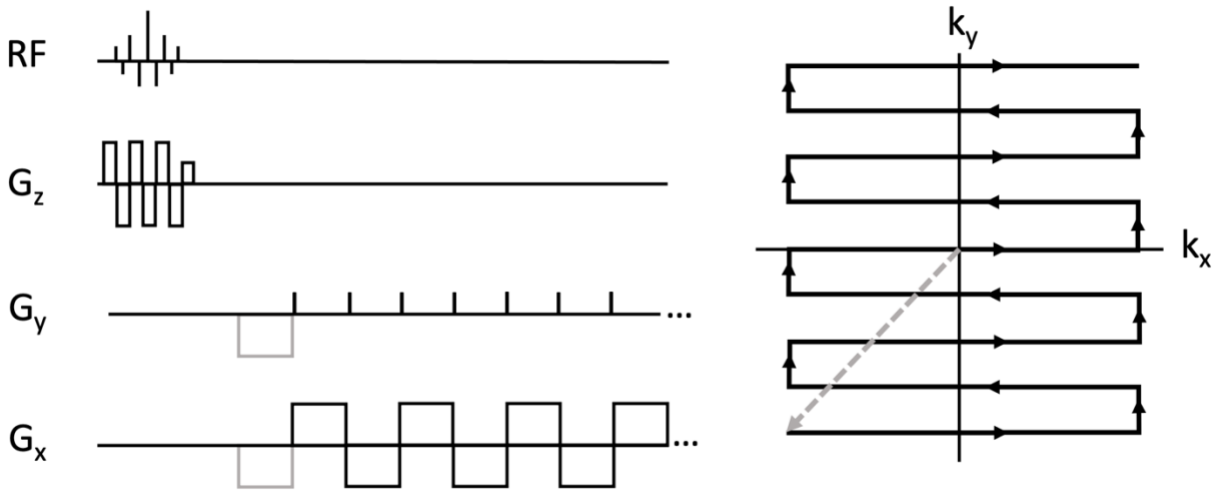
Figure 2.9. Sequence diagram of a spectral-spatial RF pulse and echo-planar readout trajectory. The echo-planar readout is characterized by the "blips" in the gradient G_y, which increment in k_y while data is acquired along k_x lines with symmetric G_x lobes.
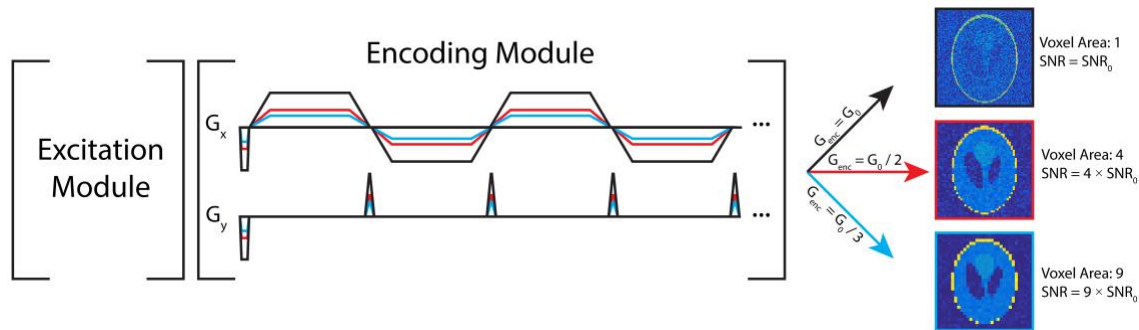
Figure 2.10. Pulse sequence diagram for variable resolution imaging using an echo-planar readout. A spectral-spatial RF pulse is used to independently excite each metabolite. The readout waveform, shown here as an echo-planar trajectory in the encoding module, can then be scaled to yield a voxel size based on the SNR for each metabolite. Adapted from Gordon et al.[5]

Variable resolution imaging is used to maximize the signal of metabolites while improving spatial resolution. In HP ^{13}C MRI the injected ^{13}C molecule has high signal but its metabolites have much lower signal due to low concentrations, slow transport in the cell, and short T_1 times. MRI voxels, which define a three-dimensional unit of space, capture signal in the specified unit of space. When there is less signal present, larger voxel sizes are used to acquire sufficient signal over background noise (defined as signal-to-noise ratio, SNR). SNR is directly proportional to the voxel size. Variable

17

resolution maximizes the SNR of downstream metabolites using coarse resolution acquisition, while taking advantage of the inherently high SNR of the injected molecule using high resolution acquisition.

2.2.3 Hyperpolarized [1-^{13}C]Pyruvate Magnetic Resonance Imaging

Of the ^{13}C compounds suitable for hyperpolarization and biocompatibility, pyruvate is the most ideal and has been used to measure metabolism extensively in preclinical and clinical studies. Pyruvate is naturally occurring in the human body as a part of the glycolysis pathway, has a long T_1 of ~60 seconds and high polarizability, and its metabolic products have sufficient chemical shift to distinguish each other. [1-^{13}C]pyruvate, the focus of this work, provides a measure of metabolic preference for either oxidative phosphorylation, which generates bicarbonate, or glycolytic metabolism, which generates lactate (Figure 2.10).
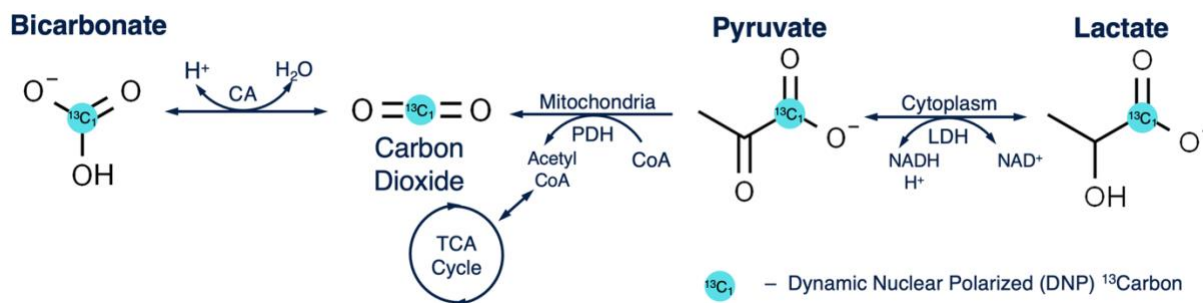
Figure 2.11. Metabolic pathways for [1-^{13}C]pyruvate to lactate and bicarbonate.

Pyruvate, lactate, and bicarbonate are well-suited for MR quantification because of their chemical shift separation as shown in Figure 2.11. Lactate and pyruvate are separated by 12 ppm (388 Hz at 3 T) and pyruvate and bicarbonate are separated by 11 ppm (355 Hz at 3 T). Pyruvate hydrate, which forms in the injection solution at conditions of pH 7.5-8.2[6], is also sufficiently separated from lactate and pyruvate by 4 and 8 ppm (129 Hz and 259 Hz at 3 T) respectively. Though as discussed in Chapter 7.2, it is important to ensure that the excitation pulse has limited bandwidth and the

reception frequencies are properly set to avoid acquiring pyruvate hydrate signal in metabolite-specific imaging.
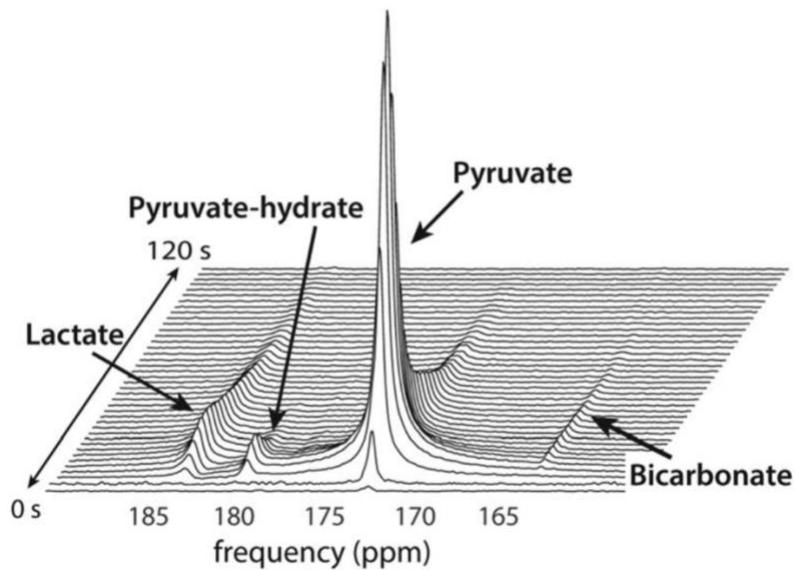
Figure 2.12. Hyperpolarized [1-^{13}C]pyruvate spectrum from a brain tumor patient. Adapted from Park et al.[7]

Normal human brains produce both lactate and bicarbonate and diseases can change their levels, such as increased lactate and decreased bicarbonate production in brain tumor lesions[8,9]. HP [1-^{13}C]pyruvate is an emerging biomarker of brain tumor metabolic reprogramming and response to therapy. In addition to brain tumors, HP [1-^{13}C]pyruvate is currently studied in research institutions worldwide with applications in prostate cancer, renal cancer, cardiac disease, pancreatic cancer, traumatic brain injury and breast cancer[10-17].

References

1. Elster AD. MRIquestions.com. Accessed January 2023.

2. Nishimura DG. *Principles of Magnetic Resonance Imaging.* Stanford University; 2010.

3. Crane JC, Gordon JW, Chen H, et al. Hyperpolarized [13] C MRI data acquisition and analysis in prostate and brain at University of California, San Francisco. *NMR in Biomedicine.* 2021;34(5). doi:10.1002/nbm.4280

4. Ardenkjær-Larsen JH, Golman K, Gram A, et al. Increase of signal-to-noise of more than 10,000 times in liquid state NMR. Discov Med. 2003;100(18):10158-10163.

5. Gordon JW, Autry AW, Tang S, et al. A variable resolution approach for improved acquisition of hyperpolarized [13] C metabolic MRI. *Magn Reson Med.* 2020;84(6):2943-2952. doi:10.1002/mrm.28421

6. Golman K, in 't Zandt R, Thaning M. Real-time metabolic imaging. *Proceedings of the National Academy of Sciences.* 2006 Jul 25;103(30):11270-5.

7. Park I, Larson PE, Gordon JW, Carvajal L, Chen HY, Bok R, Van Criekinge M, Ferrone M, Slater JB, Xu D, Kurhanewicz J. Development of methods and feasibility of using hyperpolarized carbon-13 imaging data for evaluating brain metabolism in patient studies. *Magnetic resonance in medicine.* 2018 Sep;80(3):864-73.

8. Miloushev VZ, Granlund KL, Boltyanskiy R, et al. Metabolic Imaging of the Human Brain with Hyperpolarized [13] C Pyruvate Demonstrates [13] C Lactate Production in Brain Tumor Patients. *Cancer Res.* 2018;78(14):3755-3760. doi:10.1158/0008-5472.CAN-18-0221

9. Autry AW, Gordon JW, Chen HY, et al. Characterization of serial hyperpolarized 13C metabolic imaging in patients with glioma. *NeuroImage: Clinical.* 2020;27:102323. doi:10.1016/j.nicl.2020.102323

10. Apps A, Lau JYC, Miller JJJJ, et al. Proof-of-Principle Demonstration of Direct Metabolic Imaging Following Myocardial Infarction Using Hyperpolarized 13C CMR. *JACC: Cardiovascular Imaging*. 2021;14(6):1285-1288. doi:10.1016/j.jcmg.2020.12.023

11. Gallagher FA, Woitek R, McLean MA, et al. Imaging breast cancer using hyperpolarized carbon-13 MRI. *Proc Natl Acad Sci USA*. 2020;117(4):2092-2098. doi:10.1073/pnas.1913841117

12. Granlund KL, Tee SS, Vargas HA, et al. Hyperpolarized MRI of Human Prostate Cancer Reveals Increased Lactate with Tumor Grade Driven by Monocarboxylate Transporter 1. *Cell Metabolism*. 2020;31(1):105-114.e3. doi:10.1016/j.cmet.2019.08.024

13. Hackett EP, Pinho MC, Harrison CE, et al. Imaging Acute Metabolic Changes in Patients with Mild Traumatic Brain Injury Using Hyperpolarized [1-13C]Pyruvate. *iScience*. 2020;23(12):101885. doi:10.1016/j.isci.2020.101885

14. Miloushev VZ, Granlund KL, Boltyanskiy R, et al. Metabolic Imaging of the Human Brain with Hyperpolarized ^{13} C Pyruvate Demonstrates ^{13} C Lactate Production in Brain Tumor Patients. *Cancer Res*. 2018;78(14):3755-3760. doi:10.1158/0008-5472.CAN-18-0221

15. Stødkilde-Jørgensen H, Laustsen C, Hansen ESS, et al. Pilot Study Experiences With Hyperpolarized [1‑ ^{13} C]pyruvate MRI in Pancreatic Cancer Patients. *J Magn Reson Imaging*. 2020;51(3):961-963. doi:10.1002/jmri.26888

16. Tang S, Meng MV, Slater JB, et al. Metabolic imaging with hyperpolarized ^{13} C pyruvate magnetic resonance imaging in patients with renal tumors—Initial experience. *Cancer*. 2021;127(15):2693-2704. doi:10.1002/cncr.33554

17. Tran M, Latifoltojar A, Neves JB, et al. First-in-human *in vivo* non-invasive assessment of intra-tumoral metabolic heterogeneity in renal cell carcinoma. *BJR|case reports*. 2019;5(3):20190003. doi:10.1259/bjrcr.20190003

Chapter 3

Simulation of a Variable Resolution Hyperpolarized ^{13}C MRI Approach for Improved Quantification of Brain Metabolism

Jasmine Y Hu, Peder EZ Larson, Daniel B Vigneron, Jeremy W Gordon

3.1 Abstract

Downstream metabolic products from hyperpolarized ^{13}C-pyruvate, such as lactate and bicarbonate, are acquired with coarse resolution for adequate SNR. However, the injected pyruvate exhibits high signal and can be acquired with higher resolution. In this project, a simulation framework was developed to perform multi-resolution acquisitions of hyperpolarized [1-^{13}C]pyruvate, which analyzes SNR and kinetic rate fits for differing resolution schemes. Utilizing the multi-resolution acquisition, lactate and bicarbonate showed respective SNR improvement of 3.3-fold and 5.7-fold compared to constant resolution (15 $\times$ 15 mm^2) resolution images. Kinetic fits for multi-resolution images accurately estimated ground truth values. This simulation framework performed and analyzed variable resolution acquisitions to improve metabolic quantification.

3.2 Introduction

Hyperpolarized substrates have been used to non-invasively image metabolism in preclinical[1] and clinical research applications[2], but SNR is a limiting factor in imaging metabolic products like ^{13}C bicarbonate for [1-^{13}C]pyruvate or TCA metabolites for [2-^{13}C]pyruvate. These metabolic products can exhibit reduced signal due to slow transport, low conversion rates, and short T1 times. Unlike ionizing imaging modalities, SNR scales with voxel volume for MRI, but voxel averaging after acquisition only increases SNR by the square root of voxel volume[3]. Acquiring at a coarser resolution can increase SNR and improve quantification of hyperpolarized ^{13}C MRI studies. However, acquiring high resolution pyruvate data is important to minimize partial volume effects between vascular and tissue compartments that confound quantification. Independent imaging for metabolites is possible with metabolite-specific imaging, which is implemented with a spectral-spatial pulse and single-shot echo planar readout[4]. A multi-resolution acquisition, with higher resolution for pyruvate and coarser resolutions for metabolic products, could improve metabolic quantification by decreasing partial volume effects in pyruvate images and by maintaining adequate SNR for metabolic products. To explore the accuracy of metabolic quantification from multi-resolution versus constant resolution images, a simulation framework to perform and analyze variable resolution acquisitions of [1-^{13}C]pyruvate was developed and investigated in the normal brain.

3.3 Methods

The simulation framework uses functions in the hyperpolarized-mri-toolbox from the LarsonLab GitHub[5] to generate metabolite signals and simulate acquisition of a digital phantom. Gray matter and vascular regions of interest (ROIs) in the phantom were extracted from a normal brain model from the BrainWeb Simulated Brain Database[6]. Conversion of pyruvate-to-lactate and bicarbonate (k_{PL} = 0.01 s^{-1}, k_{PB} = 0.007 s^{-1}) was mapped to the brain phantom as illustrated in Figure 1. This

brain phantom was simulated with a metabolite-selective imaging approach[4], using a single-shot echoplanar readout for encoding and a single channel coil for receive. Noise levels and conversion rates were determined based on prior studies in healthy brains. The first experiment acquired data at 5 x 5 mm^2 constant in-plane resolution, the second experiment acquired data at 15 x 15 mm^2 constant in-plane resolution, and the third experiment acquired data at variable resolutions (5 x 5 mm^2 for pyruvate, 10×10 mm^2 for lactate, 15×15 mm^2 for bicarbonate). For analysis, SNR gain, area under the curve (AUC) ratios, and kinetic rates were calculated.
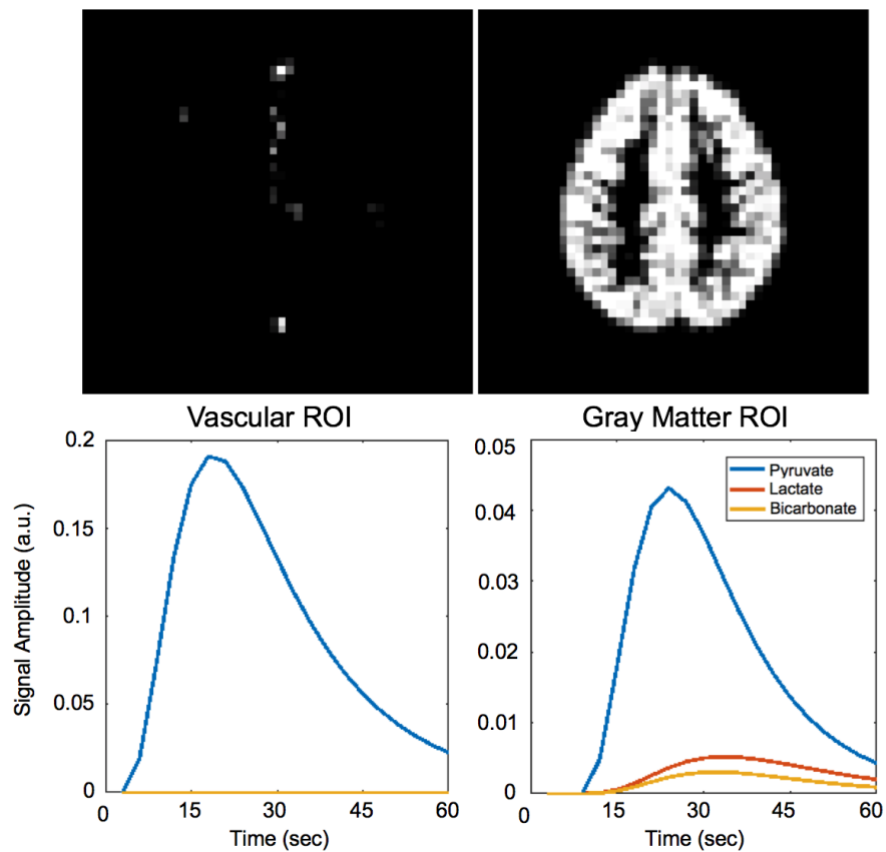
Figure 3.1 Vascular and gray matter ROIs with respective simulated hyperpolarized [1-^{13}C]pyruvate, lactate, and bicarbonate signals over time. These metabolite time course signals were mapped to the ROIs, which served as the phantom for this study.

3.4 Results

The benefits of the multi-resolution approach can be seen in the single timepoint of pyruvate to lactate and bicarbonate metabolism in Figure 2. High pyruvate signal intensity in the vascular ROIs led to ringing artifacts and partial volume effects in the constant low resolution (15×15 mm^2) pyruvate image. Lactate and bicarbonate multi-resolution images exhibited improved mean SNR by 3.3-fold and 5.7-fold in comparison to the constant high resolution (5×5 mm^2) images. With these SNR gains, kinetic rates calculated from multi-resolution images accurately estimated the ground truth values for both lactate and bicarbonate as seen in Figure 3. The high resolution kinetic rates were overestimated due to non-zero mean noise in the low SNR images. The vascular ROIs, with high pyruvate signal and no conversion to other metabolites, contributed to partial volume effects and ringing artifacts in the low resolution maps. The AUC ratios exhibited similar results, with overestimation for high resolution signals due to the non-zero mean noise in the magnitude images and a high noise floor that exceeded the bicarbonate signal level.
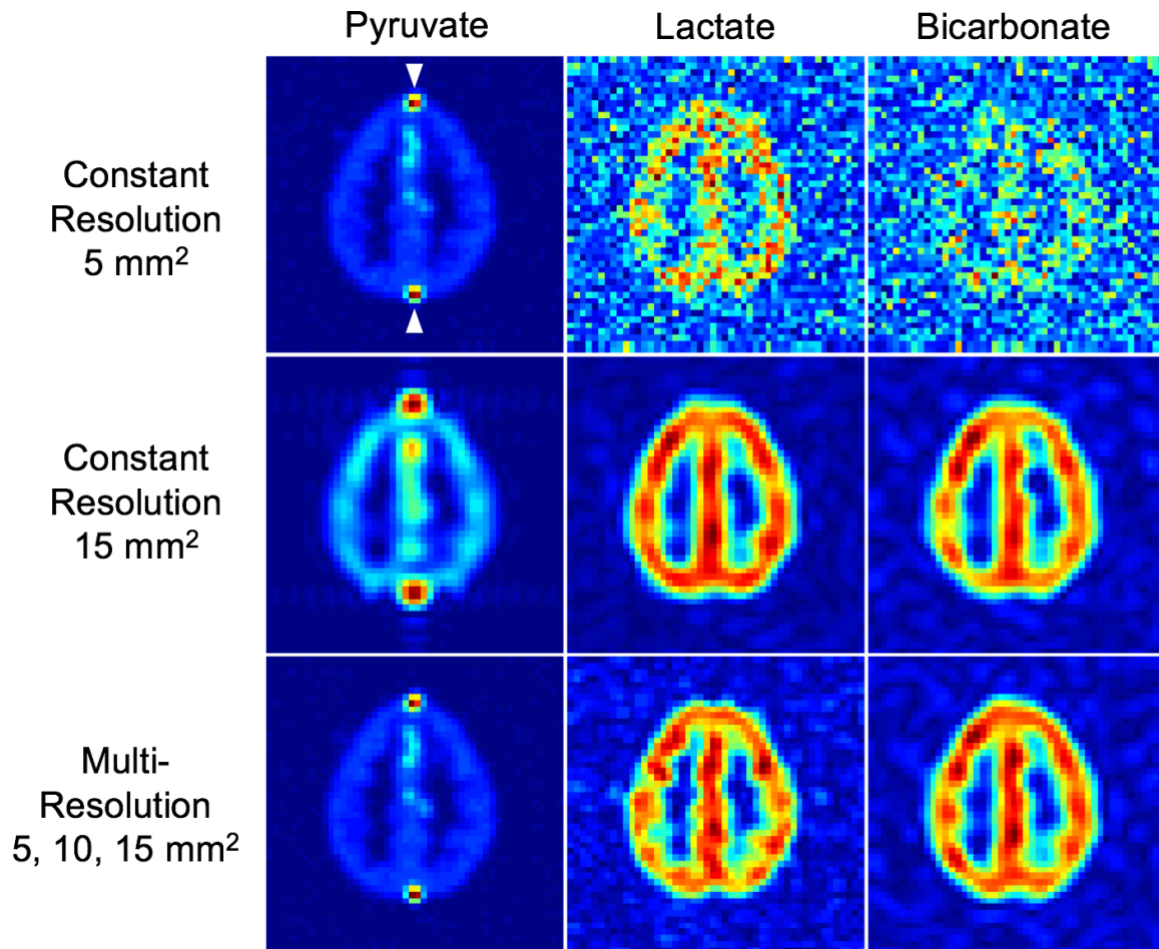
Figure 3.2. Simulated brain phantoms of hyperpolarized [1-^{13}C]pyruvate, lactate, and bicarbonate signals from 30 seconds after pyruvate bolus delivery. The white arrows in the top left image indicate vascular ROIs with high pyruvate signal and no lactate or bicarbonate signal. The multi-resolution images of lactate (10×10 mm^2) and bicarbonate (15×15 mm^2) have a respective mean SNR gain of 3.3-fold and 5.7-fold compared to the constant high resolution (5×5 mm^2) images.
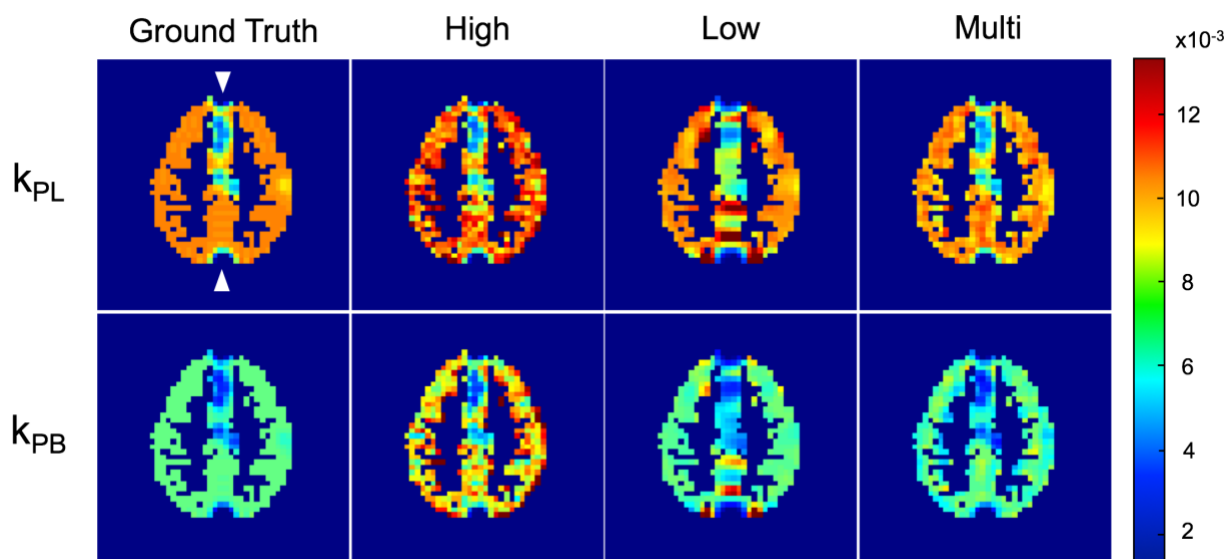
Figure 3.3. Kinetic rate maps for pyruvate-to-lactate and pyruvate-to-bicarbonate using images with different resolution schemes. The zero magnitude areas as indicated by the white arrows in the top left panel are vascular ROIs with high pyruvate signal and no conversion to lactate or bicarbonate. The multi-resolution maps yielded the most accurate estimations of the true kinetic rates.

3.5 Discussion and Conclusion

Utilizing coarser spatial resolution for low SNR metabolites, including HP ^{13}C-lactate and ^{13}C-bicarbonate, enables more accurate quantification that would otherwise be affected by high noise levels. The SNR gains from acquiring at coarser resolution were lower than theoretical gains, which is likely due to both the low SNR of the high resolution images used for comparison and also to partial volume effects in coarser resolution images. On the other hand, using higher spatial resolution for the injected substrate minimizes partial volume effects from vascular signals, particularly ringing artifacts that result from the combination of sharp transitions in signal amplitude around vessels and coarse spatial resolution. A multi-resolution approach combines the benefits of coarse and high resolution acquisitions while mitigating effects from partial volumes and low magnitude metabolite signals. But the partial volume effects of vascular pyruvate are still not clear, as

clinical data suggests that the majority of the pyruvate signal is in the vessels. Vascular pyruvate could have a large impact on the quantification of metabolite signal in nearby voxels since the typical resolution for hyperpolarized acquisitions is much larger than blood vessel diameters. Separating out the vascular pyruvate signal could also allow calculation of pyruvate perfusion, which would be a valuable input to kinetic modeling and to our understanding of hyperpolarized pyruvate dynamics in the human body. Ongoing work includes using MR angiography segmentations and simulated phantoms to separate out the vascular pyruvate signal for calculation of pyruvate perfusion in human studies. This simulation framework enabled quantitative analysis of different resolution schemes for future hyperpolarized [1-^{13}C]pyruvate studies, such that the acquisition for eventual clinical studies can maximize metabolite SNR and allow for accurate quantification.

Acknowledgements

References

1. Golman K, Thaning M. Real-time metabolic imaging. Proceedings of the National Academy of Sciences. 2006 Jul 25;103(30):11270-5.

2. Nelson SJ, Kurhanewicz J, Vigneron DB, Larson PE, Harzstark AL, Ferrone M, Van Criekinge M, Chang JW, Bok R, Park I, Reed G. Metabolic imaging of patients with prostate cancer using hyperpolarized [1-13C] pyruvate. *Science translational medicine*. 2013 Aug 14;5(198):198ra108-.

3. Edelstein WA, Glover GH, Hardy CJ, Redington RW. The intrinsic signal-to-noise ratio in NMR imaging. Magnetic resonance in medicine. 1986 Aug;3(4):604-18.

4. Gordon JW, Milshteyn E, Vigneron Daniel B, Larson Peder EZ. Variable Resolution Echo-Planar Imaging for Improved Quantification of Hyperpolarized 13C Metabolism. In Proceedings of the 26th Annual Meeting of ISMRM, Paris, France, 2018 Abstract 3053.

5. LarsonLab Github. https://github.com/LarsonLab/hyperpolarized-mri-toolbox. Accessed October 31, 2019.

6. BrainWeb Simulated Database. https://brainweb.bic.mni.mcgill.ca/brainweb/. Accessed October 15, 2019.

Chapter 4

Kinetic Analysis of Multi-Resolution Hyperpolarized ^{13}C Human Brain MRI to Study Cerebral Metabolism

Jasmine Y Hu, Yaewon Kim, Adam W Autry, Mary M Frost, Robert A Bok, Javier E Villanueva-Meyer, Duan Xu, Yan Li, Peder EZ Larson, Daniel B Vigneron, and Jeremy W Gordon. *Magnetic Resonance in Medicine.* November 2022. DOI: 10.1002/mrm.29354

4.1 Abstract

The purpose of this study was to investigate multi-resolution hyperpolarized (HP) ^{13}C-pyruvate MRI for measuring kinetic conversion rates in the human brain. HP [1-^{13}C] MRI was acquired with a multi-resolution EPI sequence with a 7.5×7.5 mm^2 resolution for pyruvate and 15×15 mm^2 resolution for the metabolites lactate and bicarbonate. With the same lactate data, two quantitative maps of pyruvate-to-lactate conversion (k_{PL}) maps were generated: one using 7.5×7.5 mm^2 resolution pyruvate data and the other using synthetic 15×15 mm^2 resolution pyruvate data to simulate a standard constant resolution acquisition. To examine local k_{PL} values across six subjects, four voxels were manually selected in each study representing brain tissue near arteries, brain tissue near veins, white matter and gray matter.

High resolution 7.5×7.5 mm^2 pyruvate images increased the spatial delineation of brain structures and decreased partial volume effects compared to coarser resolution 15×15 mm^2 pyruvate images. Voxels near arteries, veins and in white matter exhibited higher calculated k_{PL} for multi-resolution images, indicating reduced pyruvate signal contributions from blood vessels.

Acquiring HP [1-^{13}C]pyruvate metabolic data with a multi-resolution approach minimized partial volume effects from vascular pyruvate signals while maintaining the SNR of downstream metabolites. Higher resolution pyruvate images for kinetic fitting resulted in increased kinetic rate values, particularly around the superior sagittal sinus and cerebral arteries, by reducing extracellular pyruvate signal contributions from adjacent blood vessels. This HP ^{13}C study showed that acquiring pyruvate with finer resolution improved the quantification of kinetic rates throughout the human brain.

4.2 Introduction

Hyperpolarized (HP) carbon-13 MR has been investigated in animals since 2006 to provide a unique window into cellular metabolism, enabling the quantification of enzyme-catalyzed conversion rates that inform on critical cellular biochemistry in both normal and pathologic conditions[1–3]. A first-in-human proof of concept clinical trial of HP [1-^{13}C]pyruvate completed in 2013 demonstrated feasibility and safety in patients[4]. The subsequent development of commercial research polarizers enabled new technical developments and initial human studies over the past 5 years in a variety of applications including prostate cancer, brain tumors, renal cancer, cardiac disease, pancreatic cancer, traumatic brain injury and breast cancer[5–14].

Since 2018, numerous studies have focused on investigating cerebral energy metabolism in the normal brain and neuro-pathologies, demonstrating novel insights into brain bioenergetics by measuring HP pyruvate conversions to lactate and bicarbonate[6,10,11,15–17]. Conversion from pyruvate to lactate and to bicarbonate provides a measure of metabolic preference for either oxidative phosphorylation, which generates bicarbonate, or glycolytic metabolism which generates lactate. The normal brain produces both lactate and bicarbonate, and increased lactate and decreased bicarbonate production were observed in brain tumor lesions[6,15]. These studies support the utility of HP pyruvate metabolism as a biomarker of brain tumor metabolic reprogramming and response to therapy.

Recent technical advances for HP studies have shown that metabolic quantification could be further improved through specialized acquisition and denoising techniques[18–21]. These techniques provide improved SNR and finer spatial resolution, enabling better localization of metabolism. In particular, a multi-resolution HP ^{13}C EPI approach was developed that enables the acquisition of the injected HP [1-^{13}C]pyruvate at a higher spatial resolution than its metabolic products lactate and bicarbonate with their lower inherent SNR[18]. The purpose of this study was to apply for the first time this multi-resolution approach and specialized analysis to investigate HP pyruvate-to-lactate conversion rates, k_{PL}, in the normal brain with the motivation that higher pyruvate resolution could reduce partial volume effects of extracellular HP pyruvate in cerebral blood vessels that could cause errors in intracellular k_{PL} measurements.

4.3 Methods

HP brain studies were performed in six healthy human volunteer subjects with informed consent according to University of California San Francisco IRB and FDA IND approved protocols. Before each study, a pharmacist prepared samples containing 1.47 g of Good Manufacturing Practice grade

[1-^{13}C]pyruvic acid (MilliporeSigma Isotec) and 15 mM trityl electron paramagnetic agent (EPA; AH111501, GE Healthcare). The samples were polarized using a SPINlab polarizer (GE Healthcare) operating at 5 T and 0.8 K for > 2 hours. After dissolution of the polarized samples, the EPA was removed by filtration, the solution was neutralized with a Tris-buffered NaOH solution, and the quality control parameters of pH, pyruvate and residual EPA concentrations, polarization, and temperature were measured prior to injection. In parallel, the sterile filter (0.2 μm, ZenPure, Manassas, VA) was tested in agreement with manufacturer specifications prior to injection. After release by a pharmacist, a 0.43 mL/kg dose of ~250 mM pyruvate was injected at a rate of 5 mL/s, followed by a 20 mL sterile saline flush (0.9% sodium chloride, Baxter Healthcare Corporation).

Studies were performed on a 3T MR scanner (MR750, GE Healthcare) using an integrated 8 channel ^{1}H/24 channel ^{13}C phased array receiver with an 8-rung low-pass ^{13}C volume transmit coil (Rapid Biomedical, Würzburg, Germany). Hyperpolarized ^{13}C data were acquired with a metabolite-selective imaging approach, using a singleband spectral-spatial RF pulse for excitation (passband FWHM = 130 Hz, stopband = 868 Hz) and a single-shot symmetric echoplanar readout for encoding[22]. Scan parameters were 125 ms TR, 30.7 ms TE, 32 × 32 matrix size, ±19.23 kHz BW, 1.064 ms echo-spacing, eight slices with an axial orientation. Data acquisition started 5 s after the end of the saline injection for the first three subjects and immediately after the end of the saline injection for the latter three subjects. Pyruvate was excited with a 20° flip angle and lactate and bicarbonate were excited with a 30° flip angle. The slice thickness was 20 mm for the first subject and 15 mm for the other five subjects. The in-plane spatial resolution for each metabolite was changed by independently scaling the encoding gradients, resulting in 7.5 × 7.5 mm^2 resolution for pyruvate and 15 × 15 mm^2 resolution for lactate and bicarbonate. Twenty time points were acquired with a 3 second temporal resolution for a total scan time of one minute. Immediately following imaging, a non-localized

spectrum was acquired to confirm the center frequency was set correctly. For anatomic reference, ^{1}H 3D inversion-recovery spoiled gradient-recalled echo (IR-SPGR) was acquired with the dual-tuned coil. ^{1}H 3D IR-SPGR scan parameters were 6.7 ms TR, 2.5 ms TE, 450 ms IR time, $25.6 \times 25.6 \times 18.6$ cm^2 FOV, $256 \times 256 \times 124$ matrix size ($1 \times 1 \times 1.5$ mm^3 resolution).

The ^{13}C EPI data were reconstructed using the Orchestra toolbox (GE Healthcare). Multichannel data were pre-whitened[23] and then coil combined using pyruvate to estimate the coil weights[24]. Denoising was performed on the coil-combined data using global-local higher-order singular value decomposition (GL-HOSVD) as described in Kim et al. for hyperpolarized MRI[20]. To quantify the reduction in partial volume effects with variable-resolution EPI, a synthetic 15×15 mm^2 pyruvate data set was obtained by cropping the central 16×16 region of k-space, zeropadding to the original matrix size (32×32), Fermi filtering to minimize Gibbs ringing, and transforming back to the image domain. Lactate and bicarbonate images were cropped and zeropadded to match the pyruvate FOV and matrix size, and signal values were normalized to voxel volume to account for the different acquisition resolution. Proton images were used in the FSL FAST algorithm[25] to generate brain masks, and the proton images were also summed in the slice dimension to match the carbon slice thickness.

Kinetic rate constants for each voxel were computed using an inputless two-site model to generate quantitative maps of pyruvate-to-lactate conversion (k_{PL})[26]. With the same lactate data, multi-resolution and constant-resolution k_{PL} maps were generated: one using the 7.5×7.5 mm^2 resolution pyruvate data and the other using the synthetic 15×15 mm^2 resolution pyruvate data. Kinetic rate maps were respectively thresholded by metabolite total SNR > 5 summed over time and nonlinear least squares residuals fit error < 30%. Due to typically low and variable SNR across these studies,

k_{PB} maps were not considered for this analysis. k_{PL} percent differences between the different resolutions were calculated by taking the difference of multi-resolution k_{PL} and constant-resolution k_{PL} and dividing by the constant-resolution k_{PL} on a voxel-wise basis. To examine local kinetic values across the six subjects for both resolution schemes, four voxels were manually selected in each study representing brain near arteries, brain near veins, white matter and gray matter. Statistical analysis with two-sided Wilcoxon signed rank tests was used to compare the paired multi-resolution and constant resolution voxels.

4.4 Results

High resolution 7.5×7.5 mm^2 pyruvate images increased spatial delineation of brain structures and decreased partial volume effects compared to the coarse resolution 15×15 mm^2 pyruvate images as shown in Figure 4.1. In particular, high pyruvate signals from the gray matter, cerebral arteries, and sagittal sinus spilled over into surrounding brain areas in the coarser resolution images. The lactate and bicarbonate images exhibited adequate SNR > 5 at 15×15 mm^2 resolution.

In this study, dynamic high resolution pyruvate images also improved identification of pyruvate arrival in cerebral blood vessels. In Figure 4.2 the pyruvate bolus is seen first in the internal carotid and middle cerebral arteries, followed by the transverse and sagittal sinuses after one 3-second time frame. The arterial pyruvate signal fades after 15 seconds, whereas the venous pyruvate signal is maintained for the duration of the 60-second acquisition.
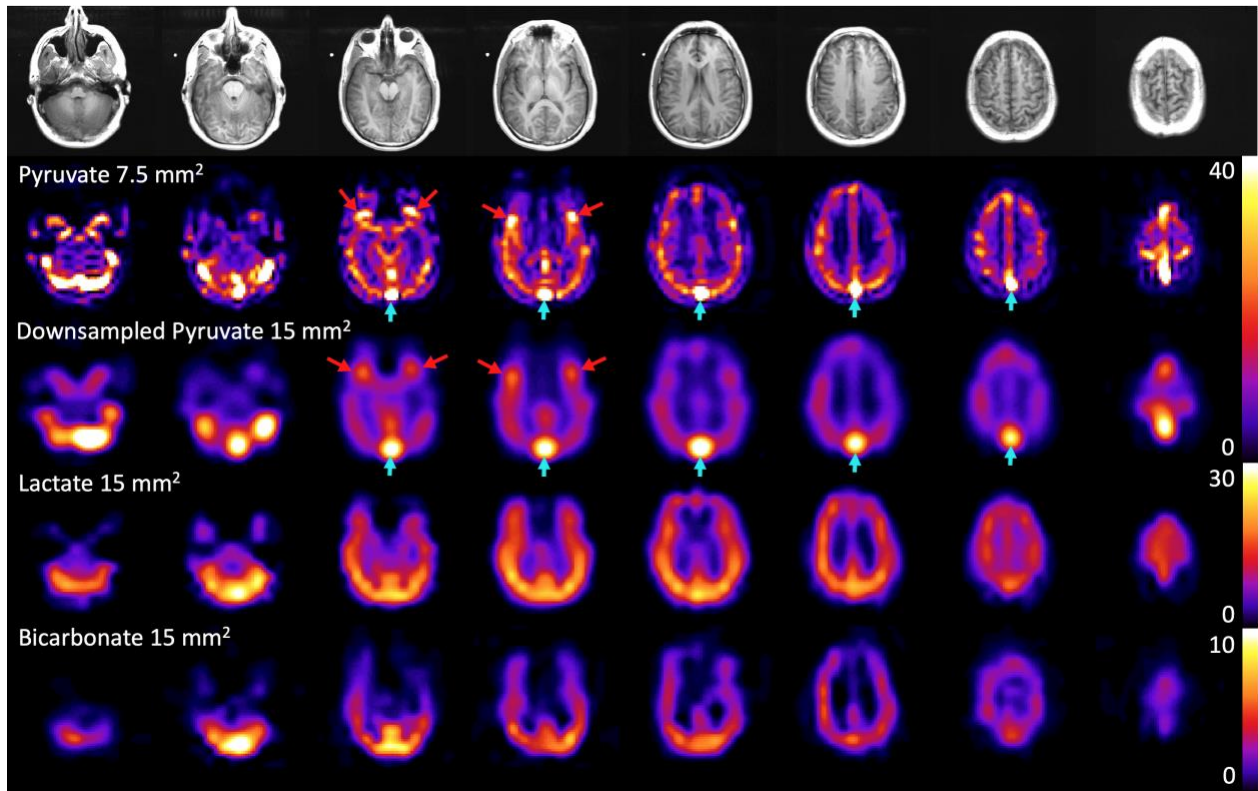
Figure 4.1. Hyperpolarized ^{13}C pyruvate, lactate and bicarbonate signals summed over 60 seconds with reference proton images of subject 2. The 15×15 mm^2 pyruvate data set was obtained by cropping 7.5×7.5 mm^2 pyruvate k-space data, zerofilling, and applying a Fermi filter. The downsampled pyruvate images exhibit partial volume spillover of signal particularly in the vasculature, including the middle cerebral arteries in slices 3-4 and the superior sagittal sinus in slices 3-8. Carbon images are zerofilled once for display.

The increased spatial delineation of high resolution pyruvate images is also apparent in the multi-resolution k_{PL} maps in Figure 4.3. The k_{PL} values were higher for multi-resolution kinetic maps, especially for the pons in the most inferior slice and white matter in the 3rd and 4th slices. The partial volume effect of decreased k_{PL} was most apparent near the ventricles and sagittal sinus, regions where high pyruvate signal spilled over from highly perfused gray matter and the sagittal sinus. The average percent k_{PL} difference for whole brain slices was 3% higher in multi-resolution maps than in constant-resolution maps.
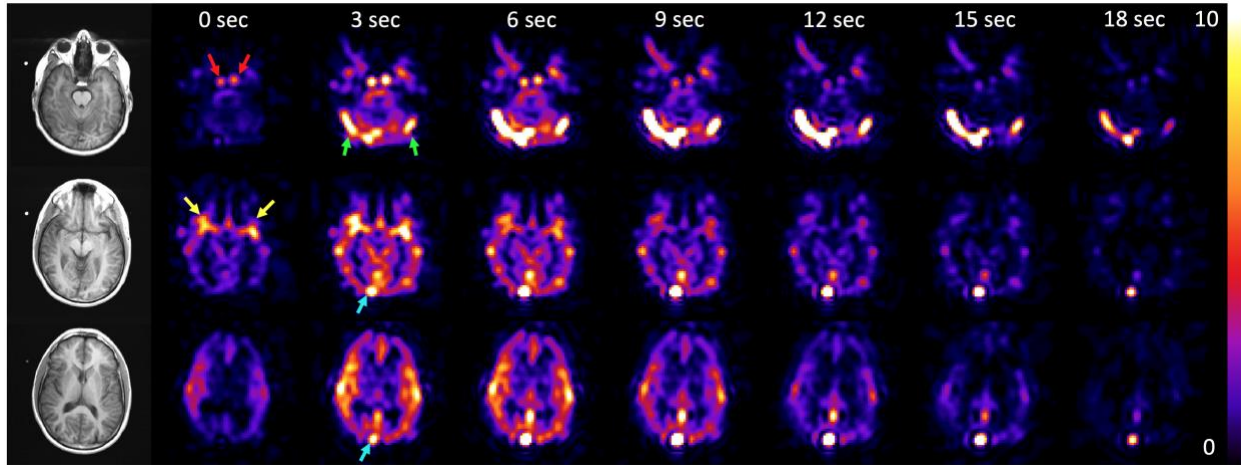
Figure 4.2. Hyperpolarized ^{13}C pyruvate dynamic images of pyruvate delivery in the brain with reference proton images of subject 5. The blue arrows point out arrival of pyruvate in the anterior cerebral circulation and transit into the superior sagittal and transverse dural venous sinuses. The arterial pyruvate signal disappears approximately 15 seconds after arrival, while the venous pyruvate signal remains high and visible towards the end of the acquisition. Images are independently scaled and zerofilled once for display.
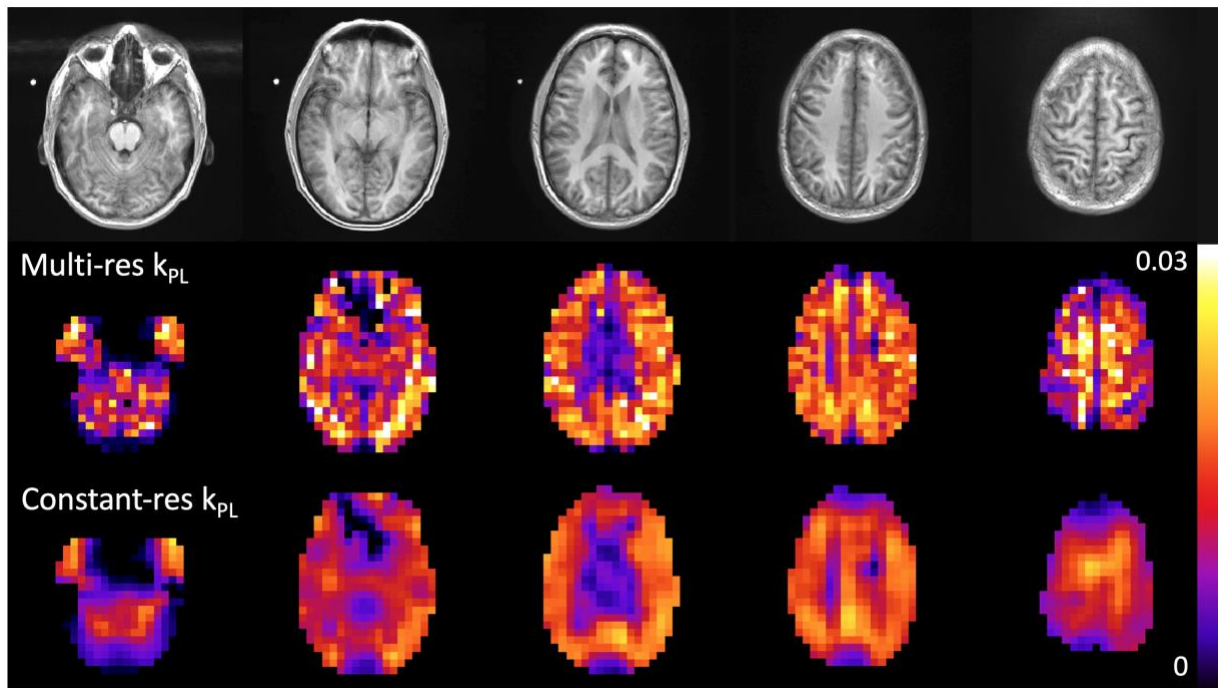
Figure 4.3 Kinetic rate maps for pyruvate-to-lactate conversion (k_{PL}) in subject 1, using 15×15 mm^2 lactate signals with 7.5×7.5 mm^2 pyruvate (multi-resolution) and synthetic 15×15 mm^2 pyruvate (constant-resolution) brain-masked images, along with reference proton images. The constant-resolution k_{PL} map showed smoothing and loss of fine detail of the kinetic rates in the brain as compared to the multi-resolution k_{PL} map.

To compare k_{PL} between multi-resolution and constant-resolution datasets on a regional basis, we selected voxels in each subject near the arteries and veins, in addition to voxels in white and gray matter. Figure 4.4 shows the selected voxel positions in proton images and k_{PL} maps as well as a table of voxel k_{PL} values for one subject. In this particular volunteer, multi-resolution k_{PL} values were 52, 77, and 47 percent higher than constant-resolution k_{PL} values for voxels near arteries, near veins and in white matter respectively. These differences are also present for the voxels for all subjects ($p < 0.05$), summarized in Table 4.1. This difference in k_{PL} values indicates that less extracellular pyruvate signal was present in the higher-resolution pyruvate voxels than in the coarse-resolution pyruvate voxels, since the lactate signal used for the multi-resolution and constant-resolution k_{PL} maps was identical.
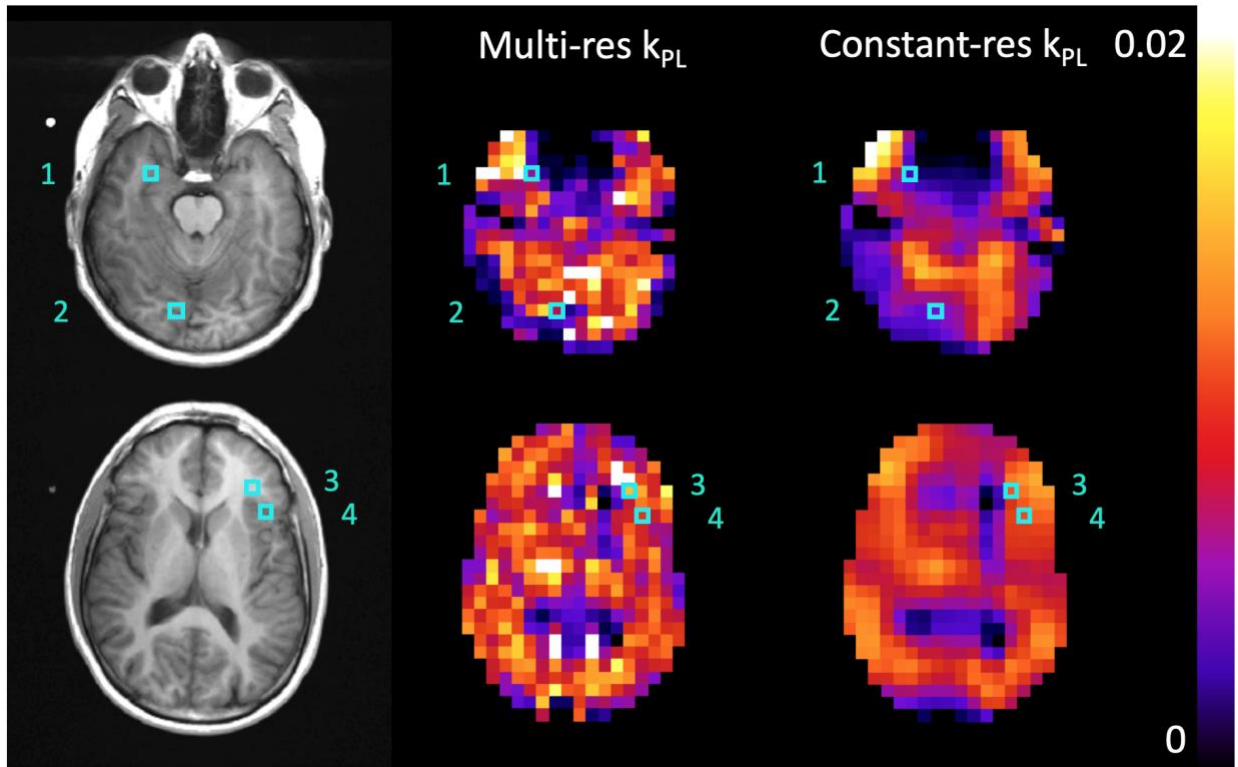
Figure 4.4 Kinetic rate maps for pyruvate-to-lactate conversion (k_{PL}) for subject 1, with selected k_{PL} values displayed with percent difference between multi-resolution and constant-resolution maps. Voxels near arteries, veins and in white matter exhibited higher k_{PL} for multi-resolution maps, indicating less pyruvate signal contributions from blood vessels. The voxel in gray matter showed less k_{PL} differences, indicating less change in the regional pyruvate signal between higher and coarser resolutions.

Table 4.1. Summary of percent differences in k_{PL} between multi-resolution and constant-resolution data from 6 subjects. Single voxels near arteries, veins, in white matter and in gray matter were selected manually. Multi-resolution k_{PL} was consistently higher for voxels near arteries and veins and voxels in white matter ($p < 0.05$), showing a decrease in partial volume spillover of vascular pyruvate. There were inconsistent differences for gray matter voxels. Subject 4 values were an average of two HP ^{13}C pyruvate injections in the same exam and stars indicate statistical significance ($p < 0.05$).

Subject	Near Arteries % k_{PL} Difference	Near Veins % k_{PL} Difference	White Matter % k_{PL} Difference	Gray Matter % k_{PL} Difference
1	52	77	47	1
2	57	96	75	46
3	37	106	57	51
4	32	73	27	-16
5	169	65	44	-7
6	153	30	71	-12
Mean ± SD	83 ± 61*	75 ± 27*	54 ± 18*	10 ± 30

4.5 Discussion

In this study, we investigated a multi-resolution acquisition to determine if higher pyruvate resolution could reduce the inclusion of extracellular pyruvate signals in blood vessels that is not metabolized, unlike intracellular pyruvate in the brain, and thus can cause errors in k_{PL} quantification. Higher spatial resolution for pyruvate (7.5×7.5 mm^2 versus 15×15 mm^2) decreased the partial volume spillover of vascular pyruvate signals into nearby brain voxels, and as a result the k_{PL} of those voxels calculated from multi-resolution data was higher than those calculated from constant-resolution data. Although the average k_{PL} difference between resolutions for whole brain slices was only 3%, for voxels near cerebral arteries the average k_{PL} difference was up to 83%. This partial volume effect was most apparent for voxels in white matter and voxels near cerebral arteries and veins. Using multi-resolution images for kinetic quantification provided more accurate k_{PL} estimates, especially near cerebral blood vessels with large amounts of pyruvate that are not available for metabolic conversion.

In addition, the multi-resolution acquisition scheme takes advantage of the high pyruvate SNR inherent to HP pyruvate studies by acquiring the injected substrate at higher resolution. These higher resolution pyruvate images improve the visualization of neuro-vascular structures and could potentially be used to extract perfusion-weighted information in addition to metabolic conversion[27]. The GL-HOSVD denoising also improves SNR for all metabolites[20], potentially enabling even further improvements in spatial resolution in future studies. Combining a multi-resolution acquisition with spatiotemporal denoising provides both high SNR and high spatial resolution, which in turn improves the accuracy of metabolic quantification.

In relation to previous HP studies on normal brain metabolism, this work studies the impact of multi-resolution acquisition on k_{PL} values. Prior studies have reported on the regional distribution of HP lactate production in terms of lactate-to-pyruvate ratio, lactate z-score, and k_{PL}[16,17]. While there are multiple metrics that can be used to quantify HP data, using multi-resolution images improves k_{PL} metabolic quantification due to reduced partial volume effects. The multi-resolution EPI approach is also flexible, as the resolutions and flip angles can be customized to each metabolite depending on SNR. Other metabolite-selective methods used for HP imaging such as spiral and balanced steady state free precession offer benefits in terms of speed and SNR and are also compatible with a multi-resolution imaging scheme.

Acquiring pyruvate with finer resolution allows for improved visualization of neurovascular structures and more accurate quantification of metabolite kinetics, but the multi-resolution acquisition comes with certain drawbacks. For this study, the metabolite signals were normalized to their respective voxel volumes for quantification. This method of matching the different resolutions assumes uniform signal distribution throughout voxels, which is not true for every voxel. Increasing

the pyruvate resolution with a single-shot readout entails a longer readout time, which can lead to increased geometric distortion in regions of high B0 inhomogeneity. This could be ameliorated by incorporating a field map into the reconstruction or alternating the blip direction during the dynamic acquisition[28,29]. Limitations of this study also include the lack of *in vivo* constant-resolution data to directly compare to the acquired multi-resolution data. Previous studies with constant-resolution echoplanar and spiral trajectories had different echo times, which may affect the calculated kinetic rates due to differences in T_2^{*}[30] and may require a correction to directly compare with the values from this study.

4.6 Conclusion

Acquiring hyperpolarized [1-^{13}C]pyruvate studies with a multi-resolution approach minimized partial volume effects from vascular pyruvate signals while maintaining the SNR of downstream metabolites. Utilizing higher resolution pyruvate images for kinetic fitting reduced partial volume effects and increased the calculated kinetic rate values, particularly around the superior sagittal sinus and cerebral arteries where high pyruvate signals spill over from the large blood vessels. This hyperpolarized ^{13}C data showed that acquiring pyruvate with finer resolution improved the quantification of kinetic rates throughout the human brain.

4.7 Supplementary Information

Supplementary Table S4.1. Voxel k_{PL} values for multi-resolution and constant-resolution ^{13}C-pyruvate data from four regions in the brain. Single voxels near arteries, veins, in white matter and in gray matter were selected manually. Multi-resolution k_{PL} was consistently higher for voxels near arteries and veins and voxels in white matter ($p < 0.05$), showing a decrease in partial volume spillover of vascular pyruvate. There were inconsistent differences for gray matter voxels. Subject 4 values were an average of two HP [1-^{13}C]pyruvate injections in the same exam and stars indicate statistical significance ($p < 0.05$).

ROI	Near Arteries*		Near Veins*		White Matter*		Gray Matter	
Subject	Multi	Constant	Multi	Constant	Multi	Constant	Multi	Constant
1	0.0079	0.0052	0.0124	0.007	0.016	0.0109	0.0198	0.0197
2	0.0105	0.0067	0.0159	0.0081	0.0105	0.006	0.013	0.0089
3	0.0078	0.0057	0.0173	0.0084	0.0077	0.0049	0.0201	0.0133
4	0.0125	0.0095	0.0126	0.0072	0.0140	0.0109	0.0114	0.0136
5	0.0191	0.0071	0.0076	0.0046	0.0148	0.0103	0.0094	0.0101
6	0.0192	0.0076	0.0103	0.0079	0.0147	0.0086	0.0111	0.0126
Mean	0.0128	0.0070	0.0127	0.0072	0.0129	0.0086	0.0141	0.0130
SD	0.0052	0.0015	0.0036	0.0014	0.0032	0.0026	0.0046	0.0038

Supplementary Table S4.2. Lactate-to-pyruvate area-under-curve (AUC) ratios for multi-resolution and constant-resolution ^{13}C-pyruvate data from four regions in the brain. Single voxels near arteries, veins, in white matter and in gray matter were selected manually. Multi-resolution AUC ratios were consistently higher for voxels near arteries and veins and voxels in white matter ($p < 0.05$), showing a decrease in partial volume spillover of vascular pyruvate. There were inconsistent differences for gray matter voxels. Subject 4 values were an average of two HP ^{13}C-pyruvate injections in the same exam and stars indicate statistical significance ($p < 0.05$).

ROI	Near Arteries*		Near Veins*		White Matter*		Gray Matter	
Subject	Multi	Constant	Multi	Constant	Multi	Constant	Multi	Constant
1	0.23	0.12	0.38	0.23	0.54	0.35	0.58	0.57
2	0.26	0.16	0.43	0.22	0.31	0.16	0.33	0.23
3	0.19	0.14	0.48	0.23	0.21	0.14	0.62	0.37
4	0.32	0.24	0.35	0.19	0.36	0.28	0.30	0.35
5	0.49	0.16	0.19	0.11	0.38	0.26	0.24	0.25
6	0.43	0.16	0.23	0.17	0.31	0.18	0.24	0.27
Mean	0.32	0.16	0.34	0.19	0.35	0.23	0.38	0.34
SD	0.12	0.04	0.11	0.05	0.11	0.08	0.17	0.13

Supplementary Table S4.3. Maximum values and standard deviation (SD) of k_{PL} and lactate-to-pyruvate area-under-curve (AUC) ratios for multi-resolution and constant-resolution ^{13}C-pyruvate data from three center slices in the brain.

Subject	k_{PL}				AUC ratio			
	Max		SD		Max		SD	
	Multi	Constant	Multi	Constant	Multi	Constant	Multi	Constant
1	0.081	0.024	0.0073	0.0044	4.43	0.73	0.3182	0.1281
2	0.046	0.020	0.0054	0.0031	2.38	0.50	0.1633	0.0791
3	0.059	0.021	0.0058	0.0043	1.53	0.56	0.1679	0.1151
4.1	0.043	0.020	0.0052	0.0034	1.51	0.50	0.16	0.0934
4.2	0.031	0.019	0.005	0.0033	0.82	0.48	0.1422	0.0901
5	0.049	0.018	0.0054	0.0033	4.27	0.40	0.2176	0.0778
6	0.067	0.029	0.0071	0.0054	1.78	0.80	0.1605	0.1121
Mean	0.054	0.021	0.006	0.004	2.389	0.566	0.190	0.099
SD	0.017	0.004	0.001	0.001	1.416	0.146	0.061	0.019
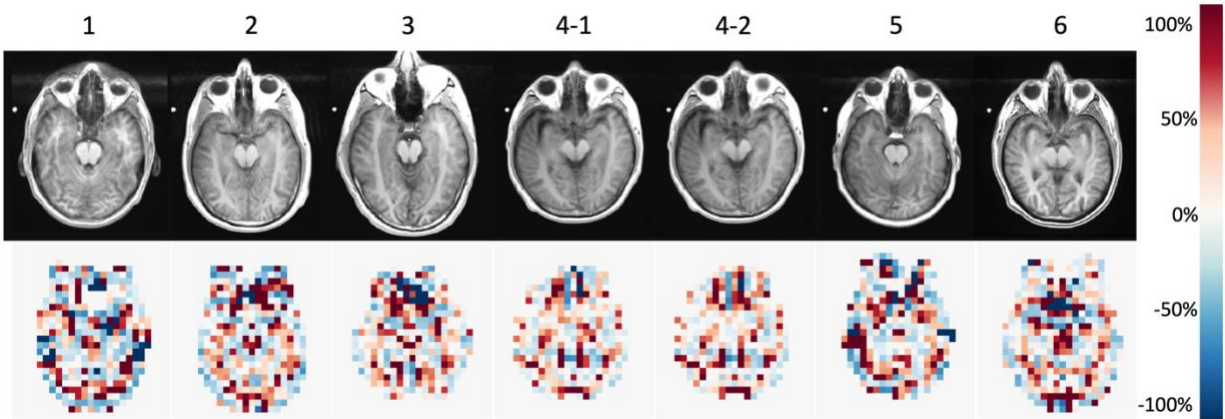
Supplementary Figure S4.1. Percent pyruvate-to-lactate conversion (k_{PL}) difference maps between constant-resolution and multi-resolution data for six subjects. Representative proton brain images are included for anatomic reference of slice location. Across subjects, the k_{PL} is higher in white matter and lower in gray matter for multi-resolution than for constant-resolution. Two hyperpolarized ^{13}C-pyruvate injections were acquired in Subject 4 within the same exam.
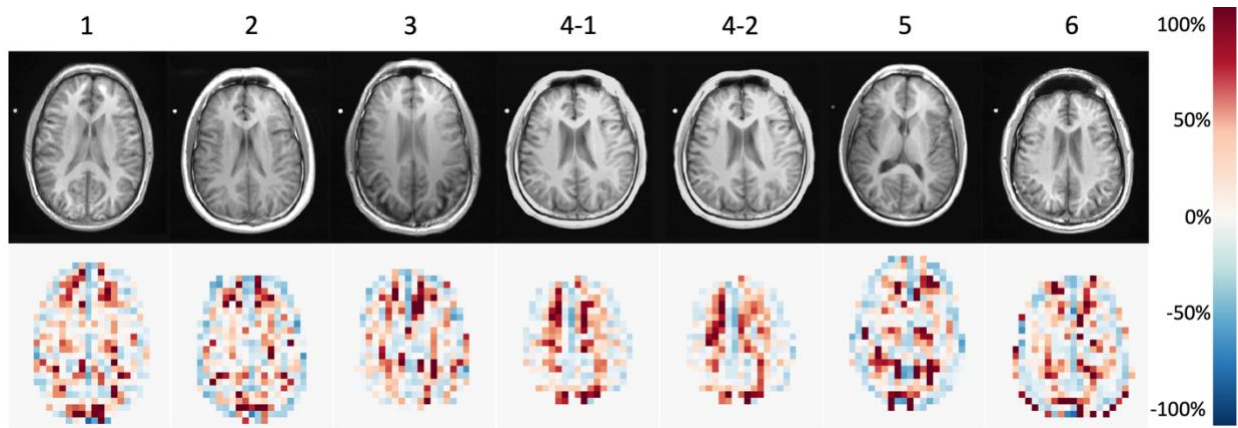
Supplementary Figure S4.2. Percent pyruvate-to-lactate conversion (k_{PL}) difference maps between constant-resolution and multi-resolution data for six subjects. Representative proton brain images are included for anatomic reference of slice location. Across subjects, the k_{PL} is higher in white matter and lower in gray matter for multi-resolution than for constant-resolution. Two hyperpolarized ^{13}C-pyruvate injections were acquired in Subject 4 within the same exam.

References

1. Golman K, in 't Zandt R, Thaning M. Real-time metabolic imaging. *Proceedings of the National Academy of Sciences*. 2006;103(30):11270-11275. doi:10.1073/pnas.0601319103

2. Kurhanewicz J, Vigneron DB, Ardenkjaer-Larsen JH, et al. Hyperpolarized 13C MRI: Path to Clinical Translation in Oncology. *Neoplasia*. 2019;21(1):1-16. doi:10.1016/j.neo.2018.09.006

3. Wang ZJ, Ohliger MA, Larson PEZ, et al. Hyperpolarized [13] C MRI: State of the Art and Future Directions. *Radiology*. 2019;291(2):273-284. doi:10.1148/radiol.2019182391

4. Nelson SJ, Kurhanewicz J, Vigneron DB, et al. Metabolic Imaging of Patients with Prostate Cancer Using Hyperpolarized [1-13C]Pyruvate. *Science Translational Medicine*. 2013;5(198):198ra108-198ra108. doi:10.1126/scitranslmed.3006070

5. Apps A, Lau JYC, Miller JJJJ, et al. Proof-of-Principle Demonstration of Direct Metabolic Imaging Following Myocardial Infarction Using Hyperpolarized 13C CMR. *JACC: Cardiovascular Imaging*. 2021;14(6):1285-1288. doi:10.1016/j.jcmg.2020.12.023

6. Autry AW, Gordon JW, Chen HY, et al. Characterization of serial hyperpolarized 13C metabolic imaging in patients with glioma. *NeuroImage: Clinical*. 2020;27:102323. doi:10.1016/j.nicl.2020.102323

7. Crane JC, Gordon JW, Chen H, et al. Hyperpolarized [13] C MRI data acquisition and analysis in prostate and brain at University of California, San Francisco. *NMR in Biomedicine*. 2021;34(5). doi:10.1002/nbm.4280

8. Gallagher FA, Woitek R, McLean MA, et al. Imaging breast cancer using hyperpolarized carbon-13 MRI. *Proc Natl Acad Sci USA*. 2020;117(4):2092-2098. doi:10.1073/pnas.1913841117

9. Granlund KL, Tee SS, Vargas HA, et al. Hyperpolarized MRI of Human Prostate Cancer Reveals Increased Lactate with Tumor Grade Driven by Monocarboxylate Transporter 1. *Cell Metabolism*. 2020;31(1):105-114.e3. doi:10.1016/j.cmet.2019.08.024

10. Hackett EP, Pinho MC, Harrison CE, et al. Imaging Acute Metabolic Changes in Patients with Mild Traumatic Brain Injury Using Hyperpolarized [1-13C]Pyruvate. *iScience*. 2020;23(12):101885. doi:10.1016/j.isci.2020.101885

11. Miloushev VZ, Granlund KL, Boltyanskiy R, et al. Metabolic Imaging of the Human Brain with Hyperpolarized [13]C Pyruvate Demonstrates [13]C Lactate Production in Brain Tumor Patients. *Cancer Res*. 2018;78(14):3755-3760. doi:10.1158/0008-5472.CAN-18-0221

12. Stødkilde-Jørgensen H, Laustsen C, Hansen ESS, et al. Pilot Study Experiences With Hyperpolarized [1-^{13}C]pyruvate MRI in Pancreatic Cancer Patients. *J Magn Reson Imaging*. 2020;51(3):961-963. doi:10.1002/jmri.26888

13. Tang S, Meng MV, Slater JB, et al. Metabolic imaging with hyperpolarized ^{13}C pyruvate magnetic resonance imaging in patients with renal tumors—Initial experience. *Cancer*. 2021;127(15):2693-2704. doi:10.1002/cncr.33554

14. Tran M, Latifoltojar A, Neves JB, et al. First-in-human *in vivo* non-invasive assessment of intra-tumoral metabolic heterogeneity in renal cell carcinoma. *BJR|case reports*. 2019;5(3):20190003. doi:10.1259/bjrcr.20190003

15. Park I, Larson PEZ, Gordon JW, et al. Development of methods and feasibility of using hyperpolarized carbon-13 imaging data for evaluating brain metabolism in patient studies: Hyperpolarized Carbon-13 Metabolic Imaging of Patients With Brain Tumors. *Magn Reson Med*. 2018;80(3):864-873. doi:10.1002/mrm.27077

16. Grist JT, McLean MA, Riemer F, et al. Quantifying normal human brain metabolism using hyperpolarized [1–13C]pyruvate and magnetic resonance imaging. *NeuroImage*. 2019;189:171-179. doi:10.1016/j.neuroimage.2019.01.027

17. Lee CY, Soliman H, Geraghty BJ, et al. Lactate topography of the human brain using hyperpolarized 13C-MRI. *NeuroImage*. 2020;204:116202. doi:10.1016/j.neuroimage.2019.116202

18. Gordon JW, Autry AW, Tang S, et al. A variable resolution approach for improved acquisition of hyperpolarized [13] C metabolic MRI. *Magn Reson Med*. 2020;84(6):2943-2952. doi:10.1002/mrm.28421

19. Chen H, Autry AW, Brender JR, et al. Tensor image enhancement and optimal multichannel receiver combination analyses for human hyperpolarized [13] C MRSI. *Magn Reson Med*. 2020;84(6):3351-3365. doi:10.1002/mrm.28328

20. Kim Y, Chen HY, Autry AW, et al. Denoising of hyperpolarized 13 C MR images of the human brain using patch-based higher-order singular value decomposition. *Magn Reson Med*. Published online June 25, 2021. doi:10.1002/mrm.28887

21. Ma J, Park JM. Super-Resolution Hyperpolarized 13C Imaging of Human Brain Using Patch-Based Algorithm. *Tomography*. 2020;6(4):343-355. doi:10.18383/j.tom.2020.00037

22. Gordon JW, Chen HY, Autry A, et al. Translation of Carbon-13 EPI for hyperpolarized MR molecular imaging of prostate and brain cancer patients. *Magn Reson Med*. 2019;81(4):2702-2709. doi:10.1002/mrm.27549

23. Pruessmann KP, Weiger M, Börnert P, Boesiger P. Advances in sensitivity encoding with arbitrary k-space trajectories. *Magn Reson Med*. 2001;46(4):638-651. doi:10.1002/mrm.1241

24. Zhu Z, Zhu X, Ohliger MA, et al. Coil combination methods for multi-channel hyperpolarized 13C imaging data from human studies. *Journal of Magnetic Resonance*. 2019;301:73-79. doi:10.1016/j.jmr.2019.01.015

25. Zhang Y, Brady M, Smith S. Segmentation of brain MR images through a hidden Markov random field model and the expectation-maximization algorithm. *IEEE Trans Med Imaging*. 2001;20(1):45-57. doi:10.1109/42.906424

26. Mammoli D, Gordon J, Autry A, et al. Kinetic Modeling of Hyperpolarized Carbon-13 Pyruvate Metabolism in the Human Brain. *IEEE Trans Med Imaging*. 2020;39(2):320-327. doi:10.1109/TMI.2019.2926437

27. Park I, Lupo JM, Nelson SJ. Correlation of Tumor Perfusion Between Carbon-13 Imaging with Hyperpolarized Pyruvate and Dynamic Susceptibility Contrast MRI in Pre-Clinical Model of Glioblastoma. *Mol Imaging Biol*. 2019;21(4):626-632. doi:10.1007/s11307-018-1275-y

28. Jezzard P, Balaban RS. Correction for geometric distortion in echo planar images from B0 field variations. *Magnetic Resonance in Medicine*. 1995;34(1):65-73. doi:10.1002/mrm.1910340111

29. Miller JJ, Lau AZ, Tyler DJ. Susceptibility-induced distortion correction in hyperpolarized echo planar imaging. *Magnetic Resonance in Medicine*. 2018;79(4):2135-2141. doi:10.1002/mrm.26839

30. Chen HY, Gordon JW, Bok RA, et al. Pulse sequence considerations for quantification of pyruvate-to-lactate conversion k_{PL} in hyperpolarized ^{13}C imaging. *NMR in Biomedicine*. 2019;32(3):e4052. doi:10.1002/nbm.4052

Chapter 5

Initial Experience on Hyperpolarized [1-^{13}C]Pyruvate MRI Multicenter Reproducibility — Are Multicenter Trials Feasible?

Nikolaj Bøgh, Jeremy W Gordon , Esben SS Hansen , Robert A Bok, Jakob U Blicher, Jasmine Y Hu, Peder EZ Larson, Daniel B Vigneron, and Christoffer Laustsen. *Tomography*. March 2022. DOI: 10.3390/tomography8020048.

I contributed to the data collection, review, and editing of this manuscript.

5.1 Abstract

Magnetic resonance imaging (MRI) with hyperpolarized [1-^{13}C]pyruvate allows real-time and pathway specific clinical detection of otherwise unimageable in vivo metabolism. However, the comparability between sites and protocols is unknown. Here, we provide initial experiences on the agreement of hyperpolarized MRI between sites and protocols by repeated imaging of same healthy volunteers in Europe and the US. Three healthy volunteers traveled for repeated multicenter brain MRI exams with hyperpolarized [1-^{13}C]pyruvate within one year. First, multisite agreement was assessed with the same echo-planar imaging protocol at both sites. Then, this was compared to a

variable resolution echo-planar imaging protocol. In total, 12 examinations were performed. Common metrics of ^{13}C-pyruvate to ^{13}C-lactate conversion were calculated, including the k_{PL}, a model-based kinetic rate constant, and its model-free equivalents. Repeatability was evaluated with intraclass correlation coefficients (ICC) for absolute agreement computed using two-way random effects models. The mean k_{PL} across all examinations in the multisite comparison was $0.024 \pm 0.0016 \, s^{-1}$. The ICC of the k_{PL} was 0.83 (p = 0.14) between sites and 0.7 (p = 0.09) between examinations of the same volunteer at any of the two sites. For the model-free metrics, the lactate Z-score had similar site-to-site ICC, while it was considerably lower for the lactate-to-pyruvate ratio. Estimation of metabolic conversion from hyperpolarized [1-^{13}C]pyruvate to lactate using model-based metrics such as k_{PL} suggests close agreement between sites and examinations in volunteers. Our initial results support harmonization of protocols, support multicenter studies, and inform their design.

5.2 Introduction

Hyperpolarization is an emerging research technology that can add dynamic metabolic imaging to the MRI toolbox by enhancing the signal of ^{13}C-enriched molecules[1]. The hyperpolarized molecule and its metabolites are detected after intravenous administration. The observable metabolites of [1-^{13}C]pyruvate are lactate, bicarbonate, and alanine, providing information on key metabolic pathways within a single scan. As increased glucose uptake and lactate production in the presence of sufficient oxygen, known as the Warburg effect, are often observed in cancer, MRI with hyperpolarized [1-^{13}C]pyruvate can aid prediction of aggression and therapy response[2,3]. Accordingly, in addition to studies in healthy individuals[4,5], cancer was the focus of the initial neuroimaging studies in disease[6-9]. Preclinically, the technology has shown promise in cancer as well as non-cancerous conditions, including vascular, traumatic, and inflammatory disease[10-13].

The conversion of hyperpolarized [1-^{13}C]pyruvate to lactate is quantifiable through mode-free approaches or kinetic fitting of the dynamic pyruvate and lactate images. Multisite trials or pooling of data should accelerate larger studies that will drive the technology to clinical use. However, it is unknown whether it suffers from the same reproducibility difficulties as some quantitative MRI technologies[14], or whether it is as reproducible as others such as diffusion weighted imaging[15]. Since the first trial in 2013[16], over 600 human examinations have been performed. The studies have been single-site efforts of several different organs and pathologies with just a few patients for each[6-9], and differences in acquisition and quantification strategies make it difficult to aggregate data. Therefore, a recent whitepaper deemed multisite trials a prerequisite to successful translation of hyperpolarized MRI[17].

Good repeatability is warranted for collaborative trials; however, no data exist to evaluate the multisite comparability of MRI with hyperpolarized [1-^{13}C]pyruvate. In order to prepare for the necessary large-scale multicenter studies, we conducted a traveling healthy volunteer pilot study to investigate the reproducibility of hyperpolarized brain imaging across sites using the same volunteers at both sites.

5.3 Materials and Methods

5.3.1 Study Design and Volunteers

Although coronavirus pandemic restrictions implemented soon after the initiation of this project in 2020 limited the travel and therefore the number of subjects in this multisite study, three healthy male volunteers (mean age of 34.7 years, span 29 to 38) were successfully imaged with hyperpolarized [1-^{13}C]pyruvate MRI of the brain on 3T systems (MR750, GE Healthcare) at the two sites. They were asked to limit caffeine to two cups of coffee and avoid alcohol from the night

before the examinations. The examinations at site 1 were performed from November 2019 to December 2019, while the examinations at site 2 were performed in November 2020. In total, 12 examinations were performed (3, 4, and 5 in each participant, respectively), of which one examination from each participant were published previously[12]. The studies were approved by the Institutional Review Board at the University of California, San Francisco, the Committee on Health Research Ethics for Central Denmark, and the Danish Medicines Agency.

5.3.2 Coil Comparison

Three different ^{13}C coils were used in this study (please refer to the section below). To compare the similarity of hardware between sites, the signal-to-noise ratio (SNR) and B1$^+$ profile of the coils employed were estimated on thermal phantoms. A spherical (Ø = 16 cm) gadolinium-doped dimethyl silicone phantom with natural ^{13}C-abundance was used (GE Healthcare). Power calibration was performed using an FID-CSI sequence with a 90° hard pulse. The phantom experiments utilized spectral-spatial excitation of a single resonance with an echo-planar imaging (EPI) readout. The B1$^+$ mapping was performed using a double-angle protocol (30°/60°) with a 5 cm slice thickness, 24 × 24 cm field of view (FOV), 16 × 16 matrix size, 3 s TR, and 20 min total scan time. The SNR experiments were performed with 10 slices of 2 cm thickness, 24 × 24 cm FOV, 16 × 16 matrix size, 62° flip angle, 0.75 s TR, and NEX = 400, yielding a total scan time of 5 min. The SNR was calculated as the mean signal across the phantom divided by signal standard deviation (SD) in a slice of noise located outside the phantom.

5.3.3 Hyperpolarized MRI

Pyruvate (1.47 g of [1-^{13}C]pyruvic acid, Sigma-Aldrich) was hyperpolarized with 15 mM AH111501 (Syncom or GE Healthcare) in a 5T SPINlab (GE Healthcare) polarizer[1]. The sample was dissolved with super-heated water, filtered, buffered, and pH, temperature, polarization, volume, and

concentrations of pyruvate and radical were measured before injection (0.43 mL/kg chased by 20 mL of saline at 5 mL/s). Imaging was started 2 s after the end of saline flush, corresponding to before the arrival of the pyruvate bolus.

The multi-site examinations followed a single protocol with metabolite-selective spectral-spatial excitation (Protocol 1, Table 1). This protocol used a published EPI sequence[18] and comparable volume transceiver coils (home-built, UCSF-MGH at site 1; PulseTeq, UK at site 2). To evaluate agreement between differing protocols, another four examinations were performed using a variable-resolution EPI with different flip angles (Protocol 2, Table 1) using a 24-channel ^{13}C receive coil (RAPID Biomedical) at site 1[19]. The [1-^{13}C]pyruvate center frequency was estimated from the proton frequency[20] and confirmed with a non-localized spectrum acquired after imaging. Before each imaging session, transmit power was calibrated on an ethylene glycol head phantom loading equally to a human head. Reference anatomical images were acquired using a spoiled gradient echo sequence (TR/TE = 7/2.4 ms, flip angle = 12°, matrix = 256 × 256, FOV = 256 × 256 mm^2, 1.5 mm slices) just before ^{13}C-imaging without moving the participant. Similarly, a B_0 field map was obtained using an Iterative Decomposition of water and fat with Echo Asymmetry and Least squares estimation sequence (IDEAL IQ, 10.9 ms TR, 4.1 ms TE, 3 echo train length). Blood flow data were obtained using pseudo-continuous arterial spin labeling (3D, 3.6 mm^3 isotropic resolution, 2025 ms post label-delay).

5.3.4 Data Reconstruction and Analysis

All ^{13}C-data were reconstructed in MATLAB (MathWorks). The EPI data were phase corrected and Fourier transformed[18,19]. Multichannel data were coil combined with weights determined from the pyruvate data[22]. Model-based and model-free analyses were performed for quantification. Rate constants of pyruvate-to-lactate conversion (k_{PL}) were fitted in a voxel-wise fashion using a two-site

metabolic exchange model[23]. No assumptions were made regarding the input function, and only the forward reaction was considered. The initial k_{PL} estimate was 0.02 s^{-1}. Fitting was performed using the Hyperpolarized MRI Toolbox (available at github.com/LarsonLab/hyperpolarized-mri-toolbox, doi: 10.5281/zenodo.1198915). We calculated the lactate-to-pyruvate ratio and the Z-score of lactate SDs from the whole-brain mean based on manually drawn regions of interest, representing frequently used model free quantifications[5,9]. Region of interest (ROI) analyses were performed on ^{13}C-images overlaid on anatomical reference scans in Horos (The Horos Project, horosproject.org) for the whole brain, the cortex, and deep white matter at the level of the ventricular bodies. The whole brain region excluded the sinuses and scalp but included the ventricles that are not expected to give raise to metabolic signal. SNR was calculated as whole brain signal divided by the SD of signal in a large region of noise outside the head.

In a sub-analysis, we adjusted for the echo time differences between the sequences of Protocol 1 and 2. This was based on a global T_2^* of pyruvate and lactate that was determined from the full width at half maximum in the non-localized, post-imaging spectra. Then, correction factors were determined using $S_0 = \frac{S}{\exp{(-\frac{TE}{T2*})}}$, where S is the observed signal and S_0 is the corrected signal. In one case, a spectrum was not acquired, and the average correction factor for examinations under the same protocol was applied. The correction was not applied for the Z-score, as only the ^{13}C-lactate signal is used.

5.3.5 Statistics

Data are presented as mean ± SD. Repeatability was assessed between sites, where all examinations made at a single site were averaged. In addition, repeatability was assessed between examinations of the same participant, regardless of the site at which the examination was performed. The intraclass

correlation coefficient (ICC) for absolute agreement of the average of the cortical and deep white matter regions of interest was determined with a two-way random effects model as suggested by Koo et al.[24]. Generally, an ICC below 0.5 is considered poor, between 0.5 and 0.75 is considered moderate, and between 0.75 and 0.9 is considered good[24]. T-tests were used for comparison of means of SNR and apparent rate constants. Statistical analysis was performed in R (R Core Team 2014, R-project.org).

5.4 Results

5.4.1 Comparability of Coils

The phantom SNR was 21.7 ± 4.3 at site 1 and 22.2 ± 4.7 at site 2 using the volume transceiver coils. The SNR of the 24-channel coil used at site 1 was 33 ± 11. The $B1^+$-fields of the volume transceivers were largely homogenous, while it was slightly more variable for the 24-channel setup ($31 \pm 2°$ vs. $33 \pm 3°$ vs. $29 \pm 5.7°$). Maps of SNR and $B1^+$ are presented in Figure 5.1.
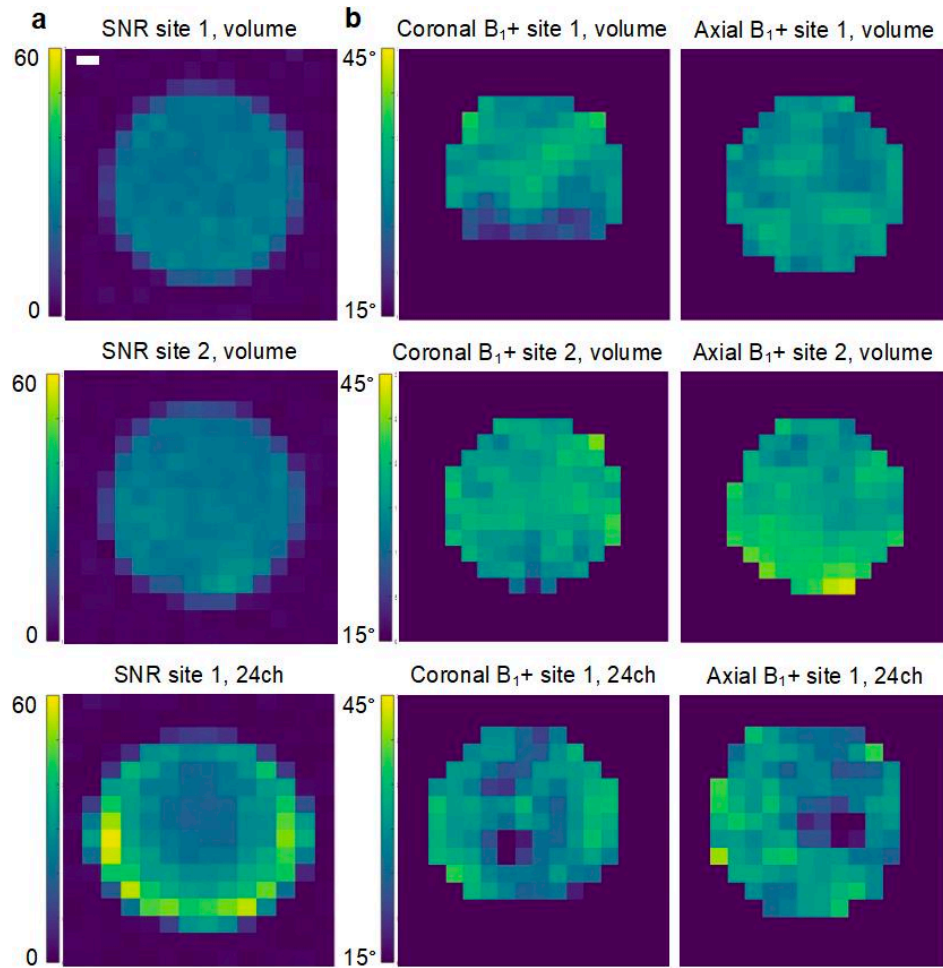
Figure 5.1. Comparison of the coils used at the two sites. The tests were performed on a natural abundance dimethyl silicone phantom by excitation of a single resonance with an echo-planar imaging readout. The signal-to-noise ratio (SNR, (a)) was determined over a 5 min scan. The $B1^+$ profile (b) was determined using the double angle method. The white scale is 2 cm.

5.4.2 Metadata of Human Examinations

Time from dissolution to injection was 51.8 ± 1.9 s at site 1 versus 86.2 ± 23.3 s at site 2 (N = 12). In all examinations, the center frequency was prescribed within 20 Hz accuracy, well within the excitation passband. The mean B_0 SD at the proton frequency over the entire brain was 23.7 ± 1.8 Hz under Protocol 1 (n = 6) and 40.4 ± 6.9 Hz under Protocol 2 (n = 4). As bicarbonate was only detected at site 1 using Protocol 2, which employed a more sensitive 24-channel ^{13}C-coil, it was not considered further (the bicarbonate SNR was 2.4 ± 0.9 under Protocol 1). The in vivo SNR of

pyruvate and lactate summed over time were 10.9 ± 4 and 13.8 ± 12.4 under Protocol 1 ($p > 0.1$ for the effect of site; $n = 8$). The brain-wide cerebral blood flow was 38.9 ± 7.4 mL/100 mL/min ($p > 0.1$ for site; $n = 10$). Data examples are presented in Figure 5.2, showing the large pyruvate pool within the vasculature, primarily the venous system, and lactate production predominantly confined to the metabolically active cortex as also observed in previous studies[4,5,18].
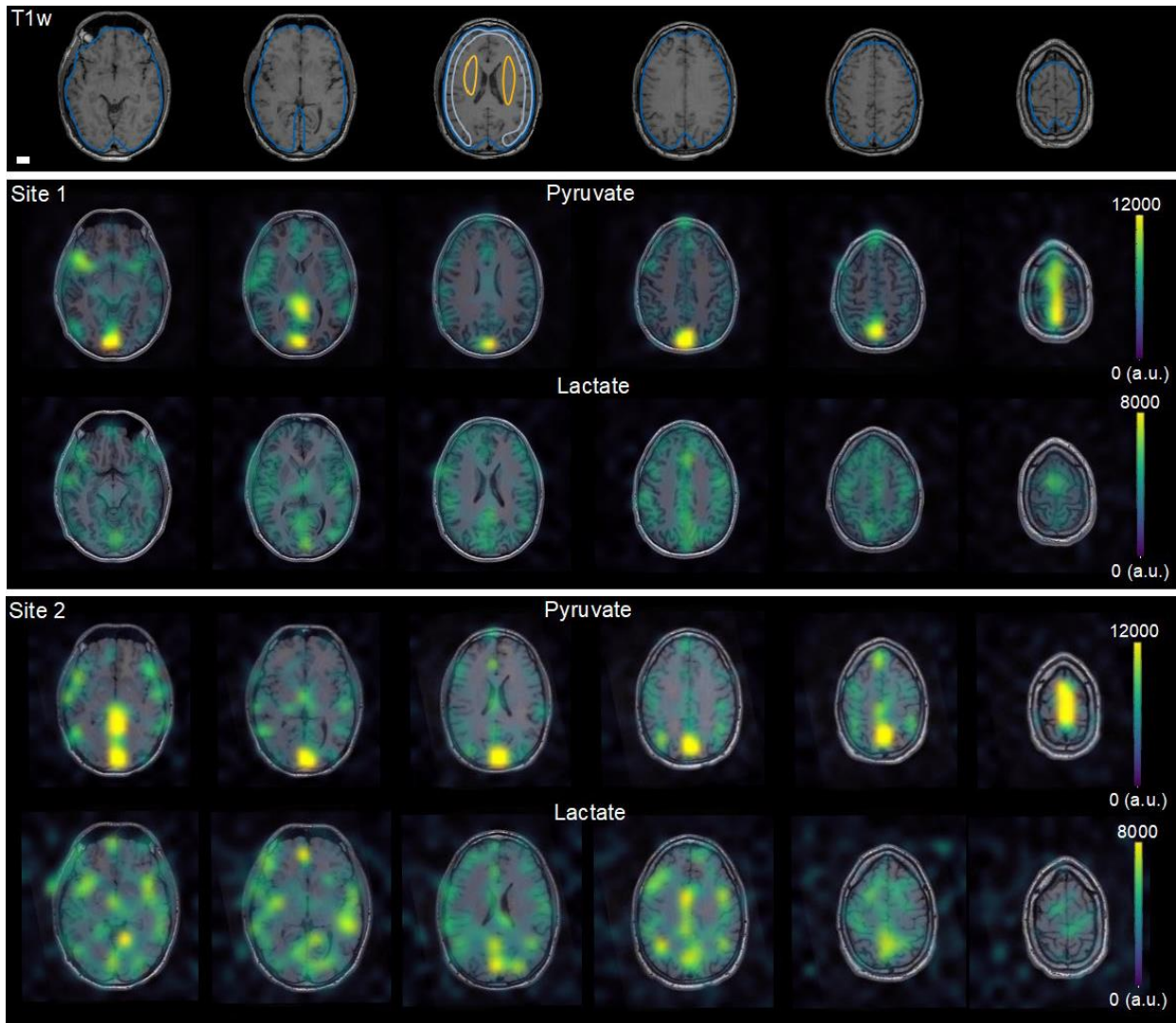
Figure 5.2. Comparison of hyperpolarized [1-^{13}C]pyruvate MRI data from each site in the same participant. After injection of hyperpolarized [1-^{13}C]pyruvate, dynamic images of [1-^{13}C]pyruvate and [1-^{13}C]lactate and were acquired in the same subjects at two sites. The six most cranial summed images are shown overlaid on T_1 weighted (T1w) images from site 2, highlighting comparability between sites. Example regions of interest are shown for the whole brain (blue), deep white matter (yellow), and cortex (grey). The white scale equals 2 cm.

5.4.3 Multisite Agreement of Hyperpolarized MRI

Our initial analyses focused on data acquired with the same protocol at two sites (Protocol 1, three scans in two participants and two in one participant; Figure 3, and Table 2). We observed no significant differences in lactate-to-pyruvate conversion metrics between the sites in any of the three regions of interest. The average k_{PL} across the whole brain, cortex, and deep white matter regions of interest at site 1 were 0.024 ± 0.0018, 0.025 ± 0.0019 and, 0.029 ± 0.0033 s^{-1}, respectively, versus 0.024 ± 0.0021, 0.026 ± 0.0013, and 0.028 ± 0.0016 s^{-1}, respectively, at site 2 ($p > 0.2$ for all comparisons). The average SD of k_{PL} within the whole brain ROI (538 ± 49 voxels at site 1, 463 ± 47 voxels at site 2) was 0.008 ± 0.0004 s^{-1} at site 1 versus 0.0085 ± 0.0003 s^{-1} at site 2 ($p = 0.09$). Within the cortex ROI, the average k_{PL} SD was 0.0069 ± 0.0009 s^{-1} at site 1 versus 0.0079 ± 0.0013 s^{-1} at site 2 ($p = 0.4$; 55 ± 5 versus 58 ± 3 voxels). Lastly, in the deep white matter ROI, it was 0.0053 ± 0.0006 s^{-1} at site 1 versus 0.006 ± 0.0005 s^{-1} at site 2 ($p = 0.13$; 32 ± 2 versus 29 ± 2 voxels). The site-to-site ICCs were 0.83 ($p = 0.14$), 0.64 ($p = 0.27$), and 0.76 ($p = 0.2$) for k_{PL}, the lactate-to-pyruvate ratio, and the lactate Z-score, respectively. Under Protocol 1, the examination-to-examination ICCs, disregarding the site in the calculation, were 0.70 ($p = 0.09$) for k_{PL}, 0.57 ($p = 0.18$) for the lactate-to-pyruvate ratio, and 0.59 ($p = 0.04$) for the lactate Z-score.
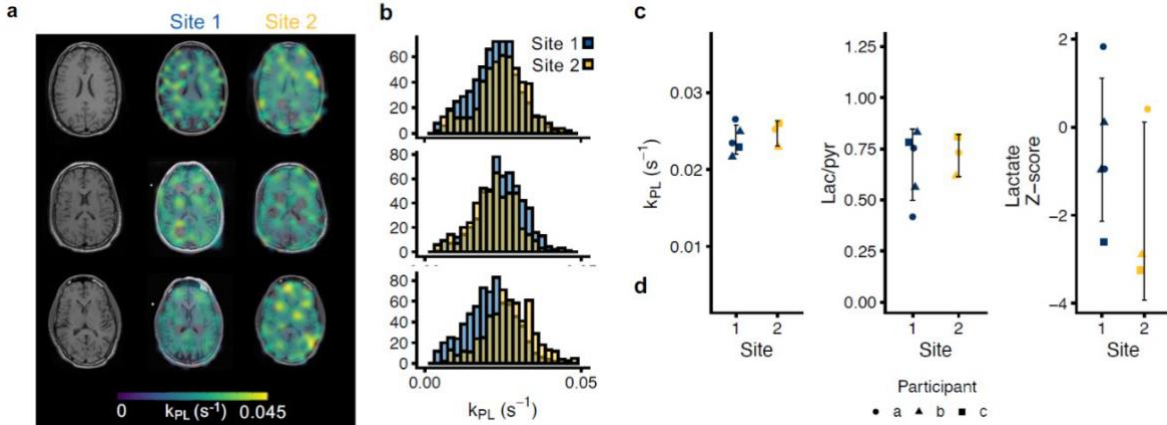
Figure 5.3. Multisite repeatability of hyperpolarized [1-^{13}C]pyruvate MRI. Imaging was performed at two sites under the same protocol (two individuals scanned three times and one scanned twice). Examples of the apparent rate constant of pyruvate-to-lactate conversion ((a), k_{PL}) are shown with corresponding histograms (b). Good site-to-site agreement was observed, particularly of the k_{PL} (c). The data are shown as individual observations of a whole brain region of interest average with one SD.

Table 5.2. Average metabolic metrics in regions of interest compared between the two sites (n = 5 at site 1, 2) using the same single-resolution protocol (Protocol 1).

	Protocol 1					
	Site 1			Site 2		
	k_{PL}	Lactate/ Pyruvate	Lactate Z-Score	k_{PL}	Lactate/ Pyruvate	Lactate Z-Score
Whole brain	0.024 ± 0.0018	0.67 ± 0.17	-	0.024 ± 0.0021	0.63 ± 0.2	-
Cortex	0.025 ± 0.0019	0.75 ± 0.16	-0.5 ± 1.63	0.026 ± 0.0013	0.73 ± 0.32	-1.66 ± 1.72
Deep white matter	0.029 ± 0.0033	0.96 ± 0.22	1.56 ± 1.5	0.024 ± 0.0016	0.96 ± 0.23	0.95 ± 1.4

5.4.4 Inter-Protocol Variation of Hyperpolarized [1-^{13}C]pyruvate MRI

We investigated the repeatability of pyruvate-to-lactate conversion metrics between two protocols (Figure 4; N = 12). Initially, we found that Protocol 1 and 2 differed by 40–50% in their estimation of pyruvate-to-lactate conversion. Protocol 2 used a multi-element coil and a variable-resolution EPI

with longer echo time. To account for this, we performed a subsequent correction of T_2^* decay. The global T_2^* of pyruvate, measured from the non-localized spectra, was longer than that of lactate (15.2 ± 5.9 ms vs. 13.9 ± 5.1 ms). The T_2^* values were shorter with the multi-channel coil than with the volume transceivers (8.9 ± 1.6 ms vs. 18 ± 4.6 ms for pyruvate, $p < 0.001$; 7.5 ± 1.3 ms vs. 16.7 ± 3.4 ms for lactate, $p < 0.001$). This adjustment largely eliminated the difference observed for Protocol 2.
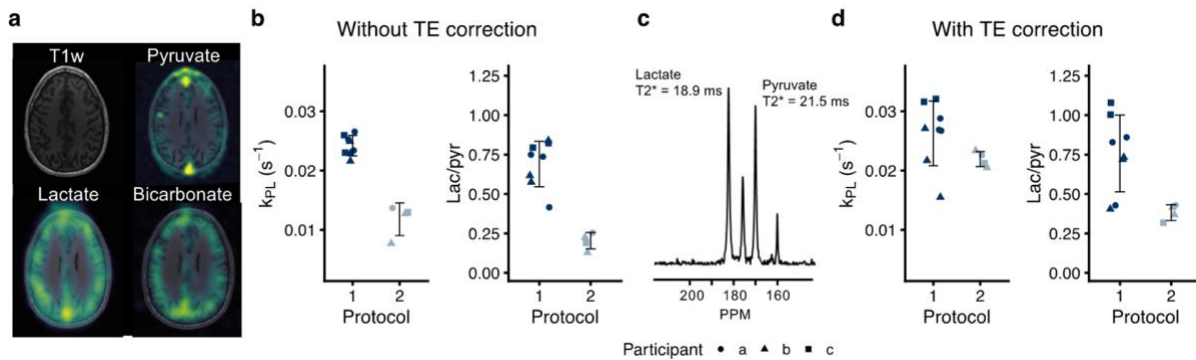
Figure 5.4. Agreement of pyruvate-to-lactate conversion with hyperpolarized [1-^{13}C]pyruvate between two protocols. One individual was imaged five times, one four times, and one three times (12 injections in total, 9 at site 1, 3 at site 2). In addition to the single-resolution echo-planar imaging protocol presented above, the volunteers were imaged with a variable-resolution equivalent ((a), see Table 1). The whole-brain apparent rate constant (k_{PL}) and the model-free whole-brain lac/pyr ratio show good repeatability within each protocol (b). However, the echo time difference between the protocols caused lower pyruvate-to-lactate conversion estimates using the variable-resolution protocol (Protocol 2). Independent T_2^* values of ^{13}C-pyruvate and ^{13}C-lactate were estimated from non-localized spectra acquired after imaging (example in (c)). These were used to adjust for the echo time differences between protocols. The correction improved the agreement of k_{PL} in particular but introduced more variation (d). The data are shown as individual observations, and the error bars represent one SD.

5.5 Discussion

The main finding of this study is the good agreement between sites in the same subjects demonstrating the feasibility of multi-institutional HP ^{13}C-pyruvate MRI studies. The results also support multicenter collaborations combining the data from subjects being scanned at a single site and suggest potential for absolute quantification. These findings are similar to previous results of good same-day repeatability within a single site[25,26], as we found close agreement between

examinations performed over a year, suggesting that the technology is robust to physiological or technical variations over this longer time period. Further, the observed 20–30% relative SDs of k_{PL} across the ROIs were similar between individuals and sites, and it was within the range of variation observed with [^{18}F]2-fluoro-2-deoxy-D-glucose–positron emission tomography (^{18}FDG-PET) in rats and phantoms[27,28]. Of interest, the change in some pathologies such as stroke and inflammation is expected to be significantly more than the relative variation observed here[11,12], while that may not always be the case in other diseases such as cancer[6,8,9], even though aggressive disease may have a distinct metabolic signature[9].

Adding valuable metabolic information to MRI, hyperpolarization is currently in clinical translation[17] and multiple single-site clinical trials are ongoing. Particularly useful in oncology, this technology allows quantification of cancerous metabolism and its response to therapy[17]. To facilitate translation, and to be truly useful, MRI with hyperpolarized [1-^{13}C]pyruvate must be repeatable and comparable across sites. Here, we provide the initial multisite experiences, suggesting good agreement between two sites. However when comparing different protocols, corrections may be needed, as further underlined by the lower apparent k_{PL} observed in a previous study in healthy volunteers[4]. In this study, echo time correction was needed to avoid confounding of the metabolic metrics by the different T_2^* of lactate and pyruvate[29,30]. The correction allowed comparison of single and variable resolution data obtained with different readouts and echo times. However, the T_2^*-estimation from non-localized spectra introduced additional variation from field inhomogeneities, including from outside the brain, as it only provided global estimates. For future studies, local T_2^* values may be estimated with multi-echo or chemical shift ^{13}C-imaging[30] or extrapolated from the proton B_0 maps. This would allow more accurate estimation of T_2^* and local corrections. In extension, shim quality should ideally be comparable between protocols, hardware, and sites, although our data show that

minor differences can be retrospectively accounted for. Of note, the finer resolution data have less partial volume effects, which may still affect the reported repeatability measures in ways that we cannot correct for.

It follows that protocol harmonization and phantom validation of the experimental setup (signal-to-noise ratio, B_1 calibration, and B_0) are important in collaborative efforts. For example, imprecise power calibration would lead to errors in k_{PL} estimates. To address this standardized experiments are needed to assess and correct the biases between protocols and setups. It is particularly important to point out that a harmonized hyperpolarized phantom for qualifying equipment and protocols would ease this process. The EPI sequence used in this study[18] has been applied widely in multiple human studies and as such represents an appealing option for future multicenter clinical trials. The imaging readout can be adjusted in the pre-scan using proton data; however, the EPI suffers from long echo times and so spiral readouts could prove useful in this regard. Further, it is worth noting that it is not fully understood what the optimal timing or flip angle schemes should be, or how point-spread bleeding of signals between voxels influences our metrics, and thus future studies need to evaluate this in better detail.

The lactate-to-pyruvate ratio, the lactate Z-score, and the k_{PL} are popular metrics that attempt to quantify pyruvate-to-lactate conversion. In particular, the lactate-to-pyruvate ratio is an appealing model-free metric[31]. Although these two metrics are proportional, the k_{PL}-fitting accounts for the differences in flip angle, whereas the lactate-to-pyruvate ratio is usually not corrected for the applied flip angles. This probably makes k_{PL} better suited for data aggregation across protocols. The Z-score had similar repeatability to k_{PL} in our analysis. As only one metabolite is analyzed, the Z-score has the advantage of being robust to differences in flip angles and T_2^* decay between resonances.

However, there seemed to be sizeable variation between volunteers, and, important in a comparability context, the Z-score is sensitive to the coil profile. The straightforward Z-score performs best with homogenous coils; alternatively, coil profile correction is warranted[32], which our data did not allow as sensitivity profiles were not acquired. Using a strategy suggested for parametric mapping, an individual Z-score of the k_{PL} may provide a viable compromise that is less sensitive to echo time differences, flip angles, and coil sensitivity[14].

We observed good agreement across examinations performed at different institutions; however, this feasibility study was limited by its small size. Another potential limitation is the fact that the participants were all healthy, young men and thus care must be taken when extending our findings to more diverse populations with varying ethnicity, gender, age, and health status. This is especially a concern in elderly patients, which are likely to be the main users of hyperpolarized MRI. However, it is important to point out that the current study design is not practical for patients or the elderly, and thus multisite repeatability studies are often performed in healthy, young individuals. Due to its small size and uncertain statistical estimates, the current study is best utilized as a primer for future multicenter studies. For example, if an ICC of 0.8 of the kPL between sites is to be confirmed with ±0.2 precision and a 95% confidence level, 14 volunteers should be imaged repeatedly at two sites, or 10 volunteers at three sites[33].

Repeatability between vendors may be a concern in quantitative MRI. We were unable to compare data acquired on systems from more than a single vendor in this pilot study. Although the equipment used in this study is the currently most prevalent in hyperpolarized ^{13}C MRI, it is important to note that including other vendor systems in the coming multicenter studies would greatly improve their impact. It is worth mentioning that we used coils from different vendors,

which did not appear to cause systematic errors. Lastly, we provide no estimates on the repeatability of pyruvate-to-bicarbonate conversion, but we expect that it is comparable to the repeatability of pyruvate-to-lactate conversion.

5.6 Conclusion

Collaborative multisite efforts are a critical step towards overcoming translational barriers and advancing hyperpolarized MRI to benefit patients. By suggesting good repeatability and shedding light on the potential pitfalls, the data provided here clear the path for further multisite studies with hyperpolarized MRI.

References

1. Ardenkjaer-Larsen, J.H.; Fridlund, B.; Gram, A.; Hansson, G.; Hansson, L.; Lerche, M.H.; Servin, R.; Thaning, M.; Golman, K. Increase in Signal-to-Noise Ratio of > 10,000 Times in Liquid-State NMR. Proc. Natl. Acad. Sci. USA 2003, 100, 10158–10163.

2. Wang, Z.J.; Ohliger, M.A.; Larson, P.E.Z.; Gordon, J.W.; Bok, R.A.; Slater, J.; Villanueva-Meyer, J.E.; Hess, C.P.; Kurhanewicz, J.; Vigneron, D.B. Hyperpolarized ^{13}C MRI: State of the Art and Future Directions. Radiology 2019, 291, 273–284.

3. Woitek, R.; McLean, M.A.; Ursprung, S.; Rueda, O.M.; Garcia, R.M.; Locke, M.J.; Beer, L.; Baxter, G.; Rundo, L.; Provenzano, E.; et al. Hyperpolarized Carbon-13 MRI for Early Response Assessment of Neoadjuvant Chemotherapy in Breast Cancer Patients. Cancer Res. 2021, 81, 6004–6017.

4. Grist, J.T.; McLean, M.A.; Riemer, F.; Schulte, R.F.; Deen, S.S.; Zaccagna, F.; Woitek, R.; Daniels, C.J.; Kaggie, J.D.; Matys, T.; et al. Quantifying Normal Human Brain Metabolism Using Hyperpolarized [1–^{13}C]Pyruvate and Magnetic Resonance Imaging. Neuroimage 2019, 189, 171–179.

5. Lee, C.Y.; Soliman, H.; Geraghty, B.J.; Chen, A.P.; Connelly, K.A.; Endre, R.; Perks,W.J.; Heyn, C.; Black, S.E.; Cunningham, C.H. Lactate Topography of the Human Brain Using Hyperpolarized ^{13}C-MRI. Neuroimage 2020, 204, 116202.

6. Miloushev, V.Z.; Granlund, K.L.; Boltyanskiy, R.; Lyashchenko, S.K.; DeAngelis, L.M.; Mellinghoff, I.K.; Brennan, C.W.; Tabar, V.; Yang, T.J.; Holodny, A.I.; et al. Metabolic Imaging of the Human Brain with Hyperpolarized ^{13}C Pyruvate Demonstrates ^{13}C Lactate Production in Brain Tumor Patients. Cancer Res. 2018, 78, 3755–3760.

7. Park, I.; Larson, P.E.Z.; Gordon, J.W.; Carvajal, L.; Chen, H.Y.; Bok, R.; Van Criekinge, M.; Ferrone, M.; Slater, J.B.; Xu, D.; et al. Development of Methods and Feasibility of Using

Hyperpolarized Carbon-13 Imaging Data for Evaluating Brain Metabolism in Patient Studies. Magn. Reson. Med. 2018, 80, 864–873.

8. Autry, A.W.; Gordon, J.W.; Chen, H.-Y.; LaFontaine, M.; Bok, R.; Van Criekinge, M.; Slater, J.B.; Carvajal, L.; Villanueva-Meyer, J.E.; Chang, S.M.; et al. Characterization of Serial Hyperpolarized ^{13}C Metabolic Imaging in Patients with Glioma. NeuroImage Clin. 2020, 27, 102323.

9. Lee, C.Y.; Soliman, H.; Bragagnolo, N.D.; Sahgal, A.; Geraghty, B.J.; Chen, A.P.; Endre, R.; Perks, W.J.; Detsky, J.S.; Leung, E.; et al. Predicting Response to Radiotherapy of Intracranial Metastases with Hyperpolarized ^{13}C MRI. J. Neurooncol. 2021, 152, 551–557.

10. Guglielmetti, C.; Chou, A.; Krukowski, K.; Najac, C.; Feng, X.; Riparip, L.K.; Rosi, S.; Chaumeil, M.M. In Vivo Metabolic Imaging of Traumatic Brain Injury. Sci. Rep. 2017, 7, 17525.

11. Guglielmetti, C.; Najac, C.; Didonna, A.; Van der Linden, A.; Ronen, S.M.; Chaumeil, M.M. Hyperpolarized ^{13}C MR Metabolic Imaging Can Detect Neuroinflammation in Vivo in a Multiple Sclerosis Murine Model. Proc. Natl. Acad. Sci. USA 2017, 114, E6982–E6991.

12. Bøgh, N.; Olin, R.B.; Hansen, E.S.; Gordon, J.W.; Bech, S.K.; Bertelsen, L.B.; Sánchez-Heredia, J.D.; Blicher, J.U.; Østergaard, L.; Ardenkjær-Larsen, J.H.; et al. Metabolic MRI with Hyperpolarized [1-^{13}C]Pyruvate Separates Benign Oligemia from Infarcting Penumbra in Porcine Stroke. J. Cereb. Blood Flow Metab. 2021, 41, 2916–2920.

13. Grist, J.T.; Miller, J.J.; Zaccagna, F.; McLean, M.A.; Riemer, F.; Matys, T.; Tyler, D.J.; Laustsen, C.; Coles, A.J.; Gallagher, F.A. Hyperpolarized 13C MRI: A Novel Approach for Probing Cerebral Metabolism in Health and Neurological Disease. J. Cereb. Blood Flow Metab. 2020, 40, 1137–1147.

14. Kranzusch, R.; aus dem Siepen, F.;Wiesemann, S.; Zange, L.; Jeuthe, S.; Ferreira da Silva, T.; Kuehne, T.; Pieske, B.; Tillmanns, C.; Friedrich, M.G.; et al. Z-Score Mapping for Standardized Analysis and Reporting of Cardiovascular Magnetic Resonance Modified Look-Locker Inversion

Recovery (MOLLI) T1 Data: Normal Behavior and Validation in Patients with Amyloidosis. J. Cardiovasc. Magn. Reson. 2020, 22, 6.

15. Grech-Sollars, M.; Hales, P.W.; Miyazaki, K.; Raschke, F.; Rodriguez, D.; Wilson, M.; Gill, S.K.; Banks, T.; Saunders, D.E.; Clayden, J.D.; et al. Multi-Centre Reproducibility of Diffusion MRI Parameters for Clinical Sequences in the Brain. NMR Biomed. 2015, 28, 468–485.

16. Nelson, S.J.; Kurhanewicz, J.; Vigneron, D.B.; Larson, P.E.; Harzstark, A.L.; Ferrone, M.; van Criekinge, M.; Chang, J.W.; Bok, R.; Park, I.; et al. Metabolic Imaging of Patients with Prostate Cancer Using Hyperpolarized [1-^{13}C]Pyruvate. Sci. Transl. Med. 2013, 5, 198ra108.

17. Kurhanewicz, J.; Vigneron, D.B.; Ardenkjaer-Larsen, J.H.; Bankson, J.A.; Brindle, K.; Cunningham, C.H.; Gallagher, F.A.; Keshari, K.R.; Kjaer, A.; Laustsen, C.; et al. Hyperpolarized ^{13}C MRI: Path to Clinical Translation in Oncology. Neoplasia 2019, 21, 1–16.

18. Gordon, J.W.; Chen, H.Y.; Autry, A.; Park, I.; Van Criekinge, M.; Mammoli, D.; Milshteyn, E.; Bok, R.; Xu, D.; Li, Y.; et al. Translation of Carbon-13 EPI for Hyperpolarized MR Molecular Imaging of Prostate and Brain Cancer Patients. Magn. Reson. Med. 2019, 81, 2702–2709.

19. Gordon, J.W.; Autry, A.W.; Tang, S.; Graham, J.Y.; Bok, R.A.; Zhu, X.; Villanueva-Meyer, J.E.; Li, Y.; Ohilger, M.A.; Abraham, M.R.; et al. A Variable Resolution Approach for Improved Acquisition of Hyperpolarized ^{13}C Metabolic MRI. Magn. Reson. Med. 2020, 84, 2943–2952.

20. Grist, J.T.; Hansen, E.S.S.; Sánchez-Heredia, J.D.; McLean, M.A.; Tougaard, R.; Riemer, F.; Schulte, R.F.; Kaggie, J.D.; Ardenkjaer- Larsen, J.H.; Laustsen, C.; et al. Creating a Clinical Platform for Carbon-13 Studies Using the Sodium-23 and Proton Resonances. Magn. Reson. Med. 2020, 84, 1817–1827.

21. Qin, Q. Point Spread Functions of the T2 Decay in K-Space Trajectories with Long Echo Train. Magn. Reson. Imaging 2012, 30, 1134–1142.

22. Zhu, Z.; Zhu, X.; Ohliger, M.A.; Tang, S.; Cao, P.; Carvajal, L.; Autry, A.W.; Li, Y.; Kurhanewicz, J.; Chang, S.; et al. Coil Combination Methods for Multi-Channel Hyperpolarized ^{13}C Imaging Data from Human Studies. J. Magn. Reson. 2019, 301, 73–79.

23. Mammoli, D.; Gordon, J.; Autry, A.; Larson, P.E.Z.; Li, Y.; Chen, H.Y.; Chung, B.; Shin, P.; Van Criekinge, M.; Carvajal, L.; et al. Kinetic Modeling of Hyperpolarized Carbon-13 Pyruvate Metabolism in the Human Brain. IEEE Trans. Med. Imaging 2019, 39, 320–327.

24. Koo, T.K.; Li, M.Y. A Guideline of Selecting and Reporting Intraclass Correlation Coefficients for Reliability Research. J. Chiropr. Med. 2016, 15, 155–163.

25. Granlund, K.L.; Tee, S.S.; Vargas, H.A.; Lyashchenko, S.K.; Reznik, E.; Fine, S.; Laudone, V.; Eastham, J.A.; Touijer, K.A.; Reuter, V.E.; et al. Hyperpolarized MRI of Human Prostate Cancer Reveals Increased Lactate with Tumor Grade Driven by Monocarboxylate Transporter 1. Cell Metab. 2019, 31, 105–114.

26. Tang, S.; Meng, M.V.; Slater, J.B.; Gordon, J.W.; Vigneron, D.B.; Stohr, B.A.; Larson, P.E.Z.; Wang, Z.J. Metabolic Imaging with Hyperpolarized 13C Pyruvate Magnetic Resonance Imaging in Patients with Renal Tumors-Initial Experience. Cancer 2021, 127, 2693–2704.

27. Proesmans, S.; Raedt, R.; Germonpré, C.; Christiaen, E.; Descamps, B.; Boon, P.; De Herdt, V.; Vanhove, C. Voxel-Based Analysis of [^{18}F]-FDG Brain PET in Rats Using Data-Driven Normalization. Front. Med. 2021, 8, 744157.

28. Fahey, F.H.; Kinahan, P.E.; Doot, R.K.; Kocak, M.; Thurston, H.; Poussaint, T.Y. Variability in PET Quantitation within a Multicenter Consortium. Med. Phys. 2010, 37, 3660–3666.

29. Chen, H.-Y.; Gordon, J.W.; Bok, R.A.; Cao, P.; von Morze, C.; van Criekinge, M.; Milshteyn, E.; Carvajal, L.; Hurd, R.E.; Kurhanewicz, J.; et al. Pulse Sequence Considerations for Quantification of Pyruvate-to-Lactate Conversion k_{PL} in Hyperpolarized ^{13}C Imaging. NMR Biomed. 2019, 32, e4052.

30. Ma, J.; Chen, J.; Reed, G.D.; Hackett, E.P.; Harrison, C.E.; Ratnakar, J.; Schulte, R.F.; Zaha, V.G.; Malloy, C.R.; Park, J.M. Cardiac Measurement of Hyperpolarized ^{13}C Metabolites Using Metabolite-Selective Multi-Echo Spiral Imaging. Magn. Med. 2021, 86, 1494–1504.

31. Hill, D.K.; Orton, M.R.; Mariotti, E.; Boult, J.K.R.; Panek, R.; Jafar, M.; Parkes, H.G.; Jamin, Y.; Miniotis, M.F.; Al-Saffar, N.M.S.; et al. Model Free Approach to Kinetic Analysis of Real-Time Hyperpolarized ^{13}C Magnetic Resonance Spectroscopy Data. PLoS ONE 2013, 8, e71996.

32. Hansen, R.B.; Sánchez-Heredia, J.D.; Bøgh, N.; Hansen, E.S.S.; Laustsen, C.; Hanson, L.G.; Ardenkjaer-Larsen, J.H. Coil Profile Estimation Strategies for Parallel Imaging with Hyperpolarized ^{13}C MRI. Magn. Reson. Med. 2019, 82, 2104–2117.

33. Bonett, D.G. Sample Size Requirements for Estimating Intraclass Correlations with Desired Precision. Stat. Med. 2002, 21, 1331–1335.

Chapter 6

Investigating Cerebral Perfusion with High Resolution Hyperpolarized [1-^{13}C]Pyruvate MRI

Jasmine Y Hu, Sana Vaziri, Nikolaj Bøgh, Yaewon Kim, Adam W Autry, Robert A Bok, Yan Li, Christoffer Laustsen, Peder EZ Larson, Susan M Chang, Duan Xu, Daniel B Vigneron, and Jeremy W Gordon

6.1 Abstract

The purpose of this study was to investigate high-resolution hyperpolarized (HP) ^{13}C pyruvate MRI for measuring cerebral perfusion in the human brain. HP [1-^{13}C]pyruvate MRI was acquired in five subjects with a multi-resolution EPI sequence with 7.5×7.5 mm^2 resolution for pyruvate. Perfusion parameters were calculated from pyruvate MRI using block-circulant singular value decomposition and compared to relative cerebral blood flow calculated from ASL. To examine regional perfusion patterns, correlations between pyruvate and ASL perfusion were performed for whole brain, gray matter, and white matter voxels. High resolution 7.5×7.5 mm^2 pyruvate images were used to obtain cerebral perfusion parameters that were positively correlated with ASL perfusion values ($p < 0.0001$). White matter exhibited the highest correlation between pyruvate and ASL perfusion, while gray matter voxels and whole brain voxels also exhibited significant positive correlation.

Acquiring HP ^{13}C pyruvate metabolic images at high resolution allows for finer spatial delineation of brain structures and can be used to obtain cerebral perfusion parameters. Pyruvate perfusion parameters were positively correlated to proton ASL perfusion values, indicating a relationship between the two perfusion measures. This HP ^{13}C study demonstrated that hyperpolarized pyruvate MRI can assess cerebral metabolism and perfusion within the same study.

6.2 Introduction

Hyperpolarized (HP) carbon-13 pyruvate is an emerging tool for non-invasive imaging of metabolism in cancer and disease research, including brain tumors and traumatic brain injury[1–4]. In the brain, HP [1-^{13}C]pyruvate is injected intravenously and rapidly converted to either lactate or bicarbonate, which provides a measure of metabolic preference for either glycolysis or oxidative phosphorylation respectively. Both lactate and bicarbonate are produced in normal brain metabolism, and an increase in lactate and decrease in bicarbonate has been observed in brain tumor lesions[1,2]. By measuring changes in metabolism, HP pyruvate is an emerging imaging tracer for measuring metabolic reprogramming in brain tumors.

Perfusion is also an important metric in brain tumors and has been imaged using ^{1}H dynamic susceptibility contrast (DSC), dynamic contrast-enhanced (DCE), and arterial spin labeling (ASL)[5]. DSC and DCE involve intravenous gadolinium contrast to measure cerebral blood flow (CBF) and capillary permeability respectively, while ASL labels inflowing blood to measure CBF. HP pyruvate imaging is similar to these imaging techniques, involving rapid imaging of a contrast agent that perfuses into tissue and is metabolized. HP pyruvate has been investigated preclinically for measuring cerebral perfusion in brain tumor xenografts[6] and cardiac perfusion[7]. Recent improvements to in-plane spatial resolution[8] (from 15×15 to 7.5×7.5 mm^2) for clinical research

HP pyruvate studies have enabled better localization and quantitation of metabolic rate constants[9]. A prior study of measuring pyruvate-to-lactate conversion rates (k_{PL}) at both spatial resolutions demonstrated a mean difference of 75% in k_{PL} for voxels near arteries and veins due the ability of separating pyruvate vascular signals from intracellular pyruvate in brain parenchyma with the finer spatial resolution[9]. The improved ability to depict the vasculature at the higher spatial resolution indicated that this approach might also be used to provide regional perfusion metrics within the same imaging study. The purpose of this study was to investigate high-resolution hyperpolarized (HP) ^{13}C pyruvate MRI for measuring cerebral perfusion in the human brain with the motivation that assessing both metabolism and perfusion within a single HP MRI could ultimately be valuable for monitoring changes in disease progression and response. To assess cerebral perfusion with HP pyruvate, high-resolution HP [1-^{13}C]pyruvate studies were acquired in healthy human brains and the resulting pyruvate perfusion parameters were compared to ^1H ASL perfusion values.

6.3 Methods

A total of 5 HP brain studies were performed in four healthy human volunteer subjects with informed consent according to University of California San Francisco IRB and FDA IND approved protocols. The mean age of the subjects was 41.2 years (range 37-47 years) and all subjects were male. Pyruvate solutions were prepared and injected as described previously[9]. Studies were performed on a 3T MR scanner (MR750, GE Healthcare) using an integrated 8 channel ^1H/24 channel ^{13}C phased array receiver with an 8-rung low-pass ^{13}C volume transmit coil (Rapid Biomedical, Würzburg, Germany). Hyperpolarized ^{13}C data were acquired with a metabolite-selective imaging approach, using a singleband spectral-spatial RF pulse for excitation (passband FWHM = 130 Hz, stopband = 868 Hz) and a single-shot symmetric echoplanar readout for encoding[10]. Scan parameters were 125 ms TR, 30.7 ms TE, 32 × 32 matrix size, ±19.23 kHz BW, 1.064 ms echo-

spacing, and eight slices with an axial orientation. Pyruvate was excited with a 20° flip angle and lactate and bicarbonate were excited with a 30° flip angle. The slice thickness was 15 mm. The in-plane spatial resolution for each metabolite was changed by independently scaling the encoding gradients, resulting in 7.5×7.5 mm^2 resolution for pyruvate and 15×15 mm^2 resolution for lactate and bicarbonate. For one subject, a second HP pyruvate study was acquired with 15×15 mm^2 resolution for all metabolites. Twenty time points were acquired with a 3 second temporal resolution for a total scan time of one minute. Data acquisition started 5 seconds after the end of the saline injection for the first two subjects and immediately after the end of the saline injection for the latter two subjects. Immediately following imaging, a non-localized spectrum was acquired to confirm the center frequency was set correctly. For proton perfusion, 3D pulsed continuous ASL was acquired with TR = 4846 ms, TE = 10.5 ms, FOV = 256 mm, BW = 125 kHz, 2025 ms post label delay, and $128 \times 128 \times 72$ matrix size ($2 \times 2 \times 4$ mm^3 resolution). For anatomic reference, [1]H 3D inversion-recovery spoiled gradient-recalled echo (IR-SPGR) was acquired with the dual-tuned coil. [1]H 3D IR-SPGR scan parameters were 6.7 ms TR, 2.5 ms TE, 450 ms IR time, $25.6 \times 25.6 \times 18.6$ cm^2 FOV, $256 \times 256 \times 124$ matrix size ($1 \times 1 \times 1.5$ mm^3 resolution).

The ^{13}C EPI data were reconstructed using the Orchestra toolbox (GE Healthcare). Multichannel data were pre-whitened[11] and then coil combined using pyruvate to estimate the coil weights[12]. Denoising was performed on the coil-combined data using global-local higher-order singular value decomposition (GL-HOSVD) as described in Kim et al. for hyperpolarized ^{13}C MRI[13]. Lactate and bicarbonate images were cropped and zero padded to match the pyruvate FOV and matrix size, and signal values were normalized to voxel volume to account for the different acquisition resolution. To obtain relative cerebral blood flow (rCBF) maps, ASL perfusion-weighted images were divided by proton density images[14]. ASL rCBF maps were resampled to the pyruvate voxel size using tri-linear

interpolation. Gray and white matter masks were segmented on T1-weighted IR-SPGR images, with the cortex being excluded from the white matter masks using the Automated Anatomical Atlas 3[15]. Voxels containing at least 90% brain, 50% gray matter, or 50% white matter were included in Pearson correlation analysis. Proton images were used in the FSL FAST algorithm[16] to generate brain masks, and the proton images were also summed in the slice dimension to match the carbon slice thickness.

To remove coil shading, bias correction using N4ITK[17] was performed on HP ^{13}C images. To obtain ^{13}C bias fields, lactate area-under-curve (AUC) images were brain-masked and input to the N4ITK algorithm using 3 layers of 100 iterations, convergence threshold of 0 to run all iterations, B-spline order of 3, and a shrink factor of 1. The resulting bias fields were then used to correct HP ^{13}C images before perfusion calculation. ASL rCBF maps did not require bias-correction because of the division of proton density images from the same coil. To visually compare pyruvate and ASL rCBF maps at similar resolutions, pyruvate rCBF maps for one subject were zerofilled twice to match ASL in-plane resolution and Fermi filtered to remove ringing artifacts.

HP pyruvate perfusion parameters were obtained by analyzing the dynamic pyruvate images with the Dynamic Susceptibility Contrast MRI toolbox (https://github.com/marcocastellaro/dsc-mri-toolbox). Up to four voxels were automatically selected to fit an arterial input function[18]. Relative cerebral blood volume (rCBV) was calculated by taking the integral of the dynamic pyruvate signal normalized by the arterial input function. rCBF and mean transit time (MTT) were calculated using block-circulant singular value decomposition and MTT was corrected for depolarization using a single T1 = 30 s[19]. Total carbon perfusion parameters were also calculated using dynamic pyruvate, lactate, and bicarbonate images corrected for respective flip angles and summed over metabolites.

Voxels with pyruvate or total carbon rCBF greater than 0.25 arbitrary units (a.u.) were excluded from correlation because the voxel locations were within the superior sagittal sinus or cerebral arteries. Normalized rCBF values were calculated using min-max normalization to compare pyruvate and ASL rCBF values. Kinetic rate constants for each voxel were computed using an inputless two-site model to generate quantitative maps of pyruvate-to-lactate conversion (k_{PL})[9,20]. Pyruvate AUC maps were also generated and bias-corrected with the same bias fields used for dynamic HP ^{13}C images. Voxel values including ASL rCBF, pyruvate rCBF, pyruvate rCBV, k_{PL}, and pyruvate AUC were compared using Pearson correlation and paired two-tailed t-tests.

6.4 Results

The dynamic time-course of high-resolution 7.5×7.5 mm^2 pyruvate images in Figure 6.1 shows the arrival and perfusion of the pyruvate bolus into the cerebral vessels and brain tissue. The arterial pyruvate signal quickly decreased within the first 20 s after the bolus arrival, while the venous signal in the superior sagittal sinus continued through the 60 s acquisition. Pyruvate signal was higher in gray matter than in white matter.
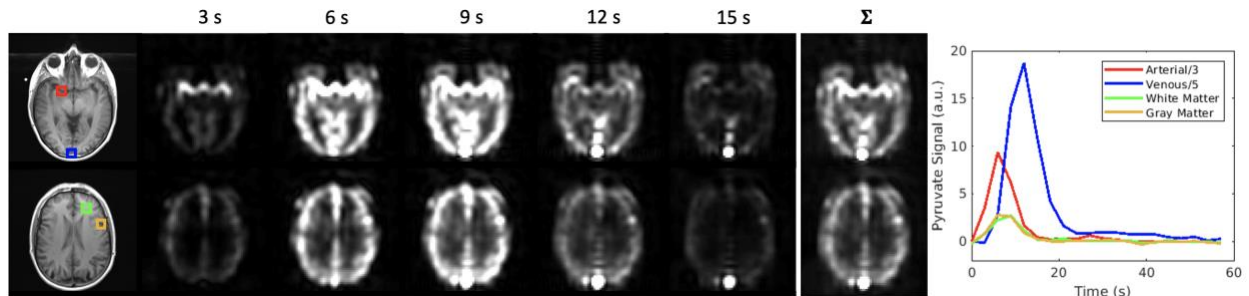
Figure 6.1. Dynamic 7.5×7.5 mm^2 [1-^{13}C]pyruvate images, area-under-curve images (Σ), and time-course plot of arterial, venous, white matter and gray matter voxels in subject 2. Pyruvate signal in the middle cereberal arteries quickly decreased within the first 20 s of the bolus arrival, while the venous signal in the superior sagittal sinus continued through the acquisition. Pyruvate signal was higher in gray matter than in white matter. Pyruvate images were zerofilled once for display and intensity units are arbitrary.

High-resolution pyruvate images were used to calculate rCBF maps, shown in Figure 6.2 along with

ASL rCBF maps. Both rCBF maps exhibit higher flow in the gray matter than in the white matter.

Pyruvate rCBF maps have large signals from the middle cerebral arteries and the anterior and

posterior portions of the superior sagittal sinus. This blood vessel weighting is even more

pronounced in pyruvate rCBF maps obtained from coarse-resolution images as shown in

Supplementary Figure S6.1, with the highest differences located near the arteries, veins, and gray

matter. Total carbon rCBF was also calculated from summed pyruvate, lactate, and bicarbonate

images and the resulting rCBF values shown in Supplementary Figure S6.2 were approximately 1.28

times higher than rCBF values calculated from pyruvate alone.
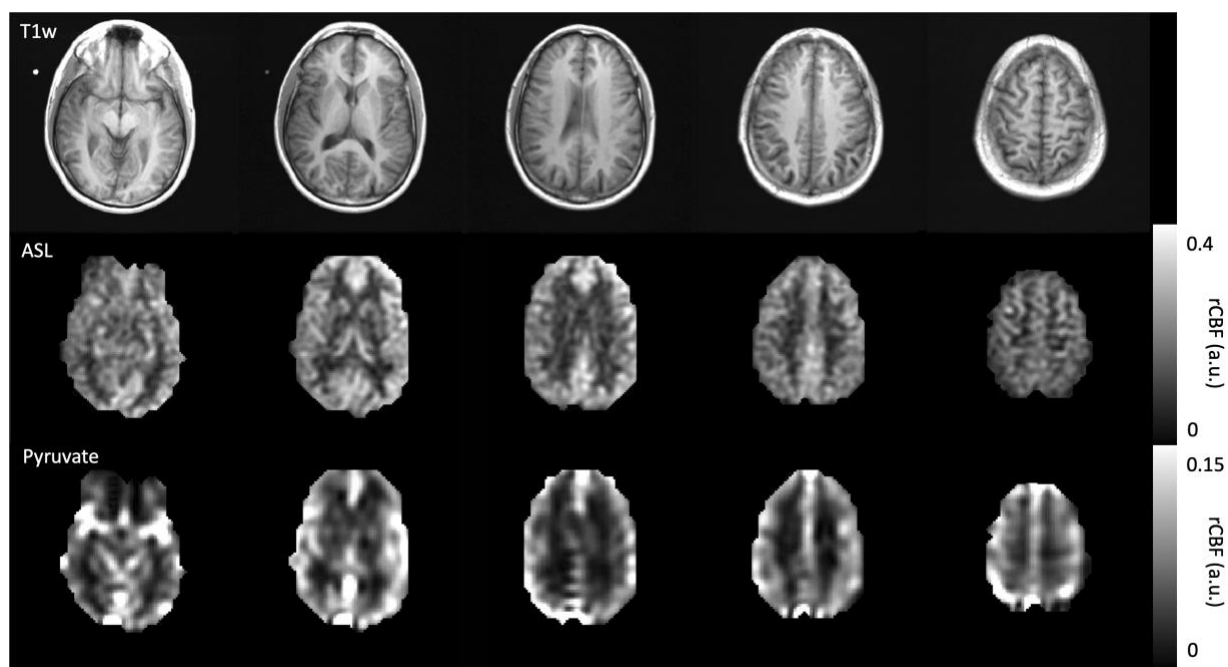
Figure 6.2. Relative CBF (rCBF) maps from ASL and [1-^{13}C]pyruvate with reference T1w images from subject 2. Both rCBF maps exhibit higher flow in the gray matter than in the white matter. Pyruvate rCBF maps have large signals from the middle cerebral arteries and superior sagittal sinus. ASL maps are summed in the slice direction to match the pyruvate slice thickness and brain-masked. Pyruvate images are zerofilled twice to match ASL in-plane resolution, Fermi filtered to remove ringing artifacts, and brain-masked. All units are arbitrary.

To compare perfusion between ASL and pyruvate-derived metrics on a regional basis, we generated

linear correlation coefficients and scatterplots shown in Figures 6.3 and 6.4. Figure 6.3 summarizes

correlations from all subjects (n = 4) and all multi-resolution studies (n = 5), by respective mask

(3024 whole brain, 1169 gray matter, and 575 white matter voxels, all from 2 central slices of the

brain). Voxels with pyruvate rCBF > 0.25 a.u. were excluded due to their being within the superior

sagittal sinus and cerebral arteries. White matter voxels exhibited the highest correlation between

pyruvate and ASL rCBF, and gray matter voxels were also moderately correlated with more spread

than white matter. Voxels with high ASL rCBF and low pyruvate rCBF were located in the

precuneus region. Correlation coefficients were consistent across individual studies and brain masks

as summarized in Table 6.1.
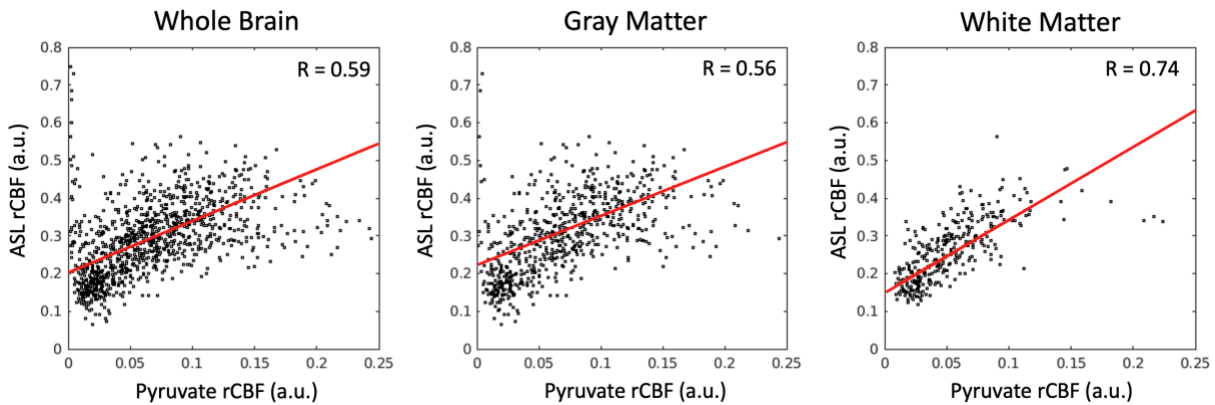
Figure 6.3. Pyruvate rCBF versus ASL rCBF linear correlation coefficients and scatterplots for voxels from all subjects (n = 4) acquired at high resolution (n = 5), by respective mask (3024 whole brain, 1169 gray matter, and 575 white matter voxels all from 2 central slices of the brain). Voxels with pyruvate rCBF > 0.25 arbitrary units (a.u.) were excluded due to their being within the superior sagittal sinus and cerebral arteries. White matter voxels exhibited the highest correlation between pyruvate and ASL rCBF, and gray matter voxels were also moderately correlated with more spread than white matter. Voxels with high ASL rCBF and low pyruvate rCBF (far upper left of whole brain and gray matter plots) were located in the precuneus region. All correlation coefficients were significant ($p < 10^{-4}$) and all units are arbitrary.

Table 6.1. Subject correlation coefficients between pyruvate rCBF and ASL rCBF. All correlation coefficients are significant ($p < 10^{-5}$). Studies 4 and 5 are acquisitions of the same subject two years apart.

Study	Whole brain	Gray matter	White matter
1	0.62	0.41	0.66
2	0.39	0.37	0.58
3	0.62	0.55	0.79
4	0.65	0.50	0.76
5	0.64	0.75	0.76
Mean ± SD	0.58 ± 0.11	0.52 ± 0.15	0.71 ± 0.09

To explore the high correlations within white matter further, Figure 6.4 shows correlation plots and coefficients for ASL versus pyruvate perfusion and metabolic parameters from white matter voxels from study 4. Pyruvate rCBF and rCBV were highly correlated to ASL rCBF, whereas pyruvate-to-lactate conversion rate (k_{PL}) was not significantly correlated to ASL rCBF. Pyruvate area-under-curve (AUC) was weakly correlated with pyruvate rCBV. Pyruvate rCBF and pyruvate rCBV were highly correlated to each other.

To directly examine the differences between ASL and pyruvate rCBF on a voxel-wise basis, we calculated the percent difference of normalized ASL and pyruvate rCBF shown in Figure 6.5. Normalized ASL and pyruvate rCBF measurements are more closely matched in white matter than in gray matter. Overall normalized ASL rCBF is higher than normalized pyruvate rCBF, particularly in the precuneus region.
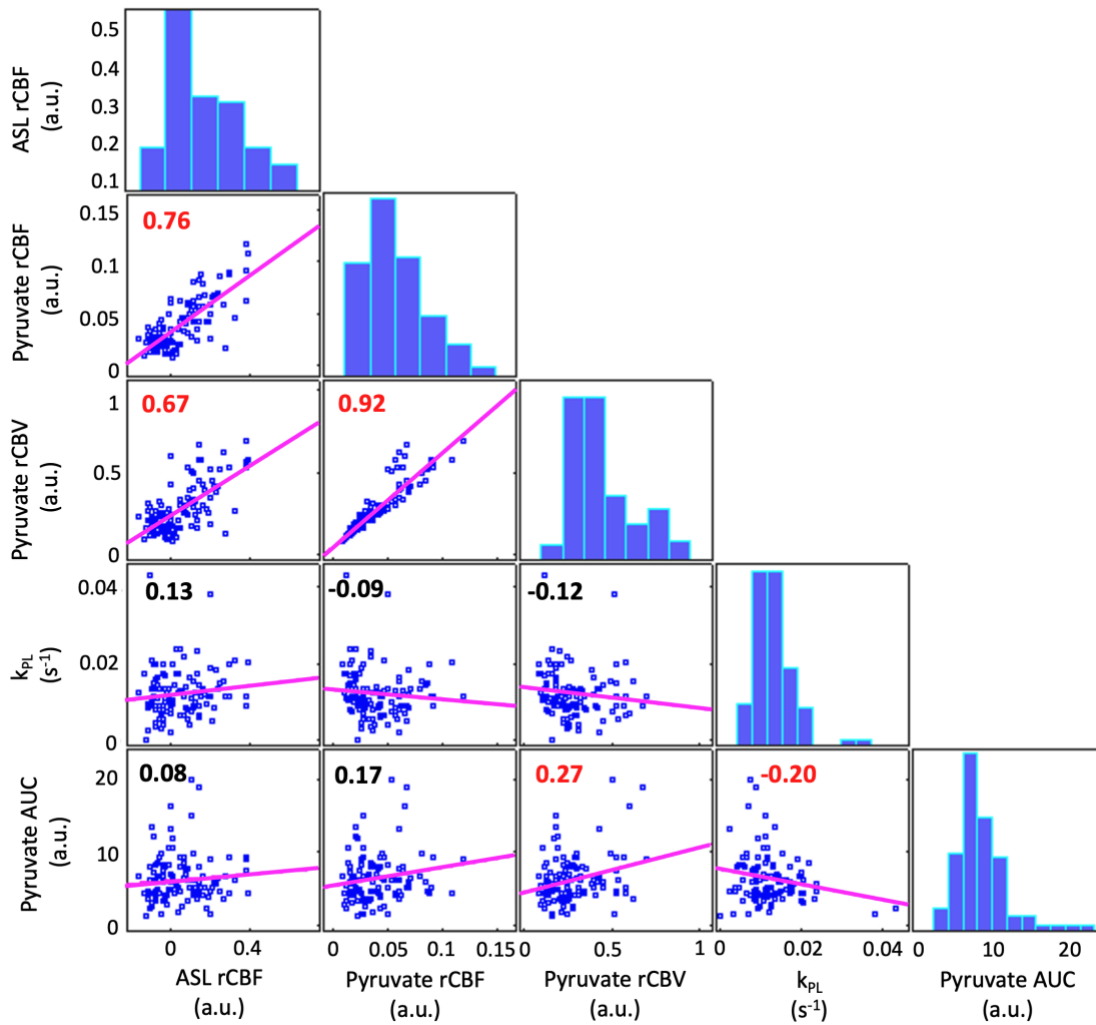
Figure 6.4. Correlation plots and coefficients for ASL versus pyruvate perfusion and metabolic parameters from white matter voxels in study 4. Red coefficient values indicate $p < 0.05$. Pyruvate rCBF and rCBV were highly correlated to ASL rCBF, whereas pyruvate to lactate conversion (k_{PL}) was not significantly correlated to ASL rCBF and pyruvate perfusion metrics. Pyruvate area-under-curve (AUC) was weakly correlated with pyruvate rCBV which affirms the contribution of perfusion to the AUC. Pyruvate rCBF and pyruvate rCBV are highly correlated to each other, which is due to their calculation from the same input data.
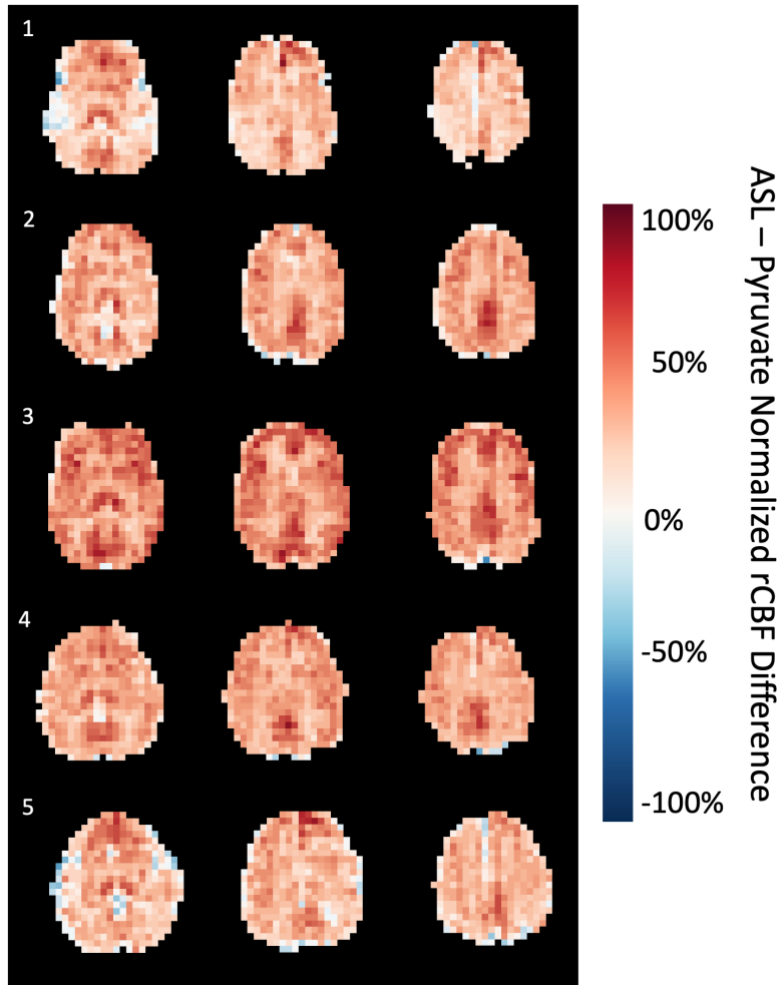
Figure 6.5. Percent difference map of normalized ASL and pyruvate rCBF for all high-resolution studies. Studies 4 and 5 are acquisitions of the same subject two years apart. Normalized ASL and pyruvate rCBF measurements are more closely matched in white matter than in gray matter. The precuneus region is consistently elevated for normalized ASL rCBF as compared to pyruvate rCBF.

6.5 Discussion

In this study, we utilized high resolution pyruvate images to obtain cerebral perfusion and metabolism parameters. The highest pyruvate signal and flow was in blood vessels, which was reflected in pyruvate rCBF maps by high weighting near the middle cerebral arteries and the anterior and posterior portions of the superior sagittal sinus. Pyruvate rCBF maps exhibited higher flow in gray matter than in white matter, similar to what was observed in ASL rCBF maps. When examining

regional differences between ASL and pyruvate rCBF, normalized white matter rCBF was closer to normalized ASL rCBF than gray matter rCBF. This pattern was continued in the linear correlations between ASL and pyruvate rCBF, where white matter rCBF values exhibited the highest correlations with ASL rCBF for individual studies and for all studies combined. This correlation difference between gray and white matter may be due to the distribution and thickness of each brain matter type in relation to the voxel size of HP pyruvate image acquisition. 7.5×7.5 mm^2 is larger than the thickness of cortical gray matter (average 2.5 mm, range 1-4.5 mm)[21]. Gray matter voxels can also include cerebral blood vessels which can have much higher signals, though we have attempted to exclude those voxels using a pyruvate rCBF threshold. The white matter region is large in comparison to gray matter, which makes it a consistent region to record measurements. In addition to partial volume effects, increased pyruvate metabolism in gray matter as compared to white matter could contribute to the extent of pyruvate and ASL rCBF correlation for each region[22,23]. HP lactate and bicarbonate signals in the precuneus were among the highest in a topography study of normal human brains[23], suggesting that elevated metabolism in the precuneus[24,25] could affect the HP pyruvate signal. We further explored perfusion relationships in white matter by correlating ASL rCBF and additional pyruvate perfusion and metabolic parameters. ASL and pyruvate perfusion parameters were not correlated with k_{PL}, indicating that the kinetic modeling is not strongly influenced by perfusion for healthy volunteers. Pyruvate AUC was weakly correlated to both ASL and pyruvate perfusion metrics which affirms the contribution of perfusion to AUC.

HP pyruvate can be used to obtain both cerebral perfusion and metabolism measurements, but this study had some limitations. In addition to perfusion, the HP pyruvate signal is affected by magnetization utilization, T_1 decay, and metabolism during the acquisition time frame. The use of the arterial input function to calculate perfusion metrics normalizes for magnetization utilization and

T_1 decay, and we assumed that the impact of metabolism on the bulk pyruvate signal is negligible. To verify the impact of metabolism, we have used the total carbon-13 signal from all HP metabolites to also calculate perfusion and have found that the resulting measurements are linearly scaled compared to those calculated from only pyruvate signals. Lactate AUC images were used in N4ITK bias correction to correct coil shading in HP images. Pyruvate AUC images were not used because doing so resulted in a bias field heavily weighted by large pyruvate signals in the anterior and posterior portions of the superior sagittal sinus.

This work is the first to use high resolution HP pyruvate images to estimate perfusion in human brains. Preclinical studies have used HP pyruvate to measure cerebral perfusion[6,7], as well as co-polarizations of pyruvate and urea for simultaneous metabolism and perfusion measurements[26,27]. ^{13}C-labeled urea is a perfusion agent that is currently under investigation in human studies and is a promising method of improving the HP perfusion measurements shown here. Because urea functions as a metabolically inactive and extracellular perfusion agent, its signal represents blood flow and perfusion without the effects of metabolic conversion[28,29]. With the combination of high-resolution imaging[8], denoising[13], and bias correction[17], HP pyruvate provides spatially detailed and unique perfusion measurements that have further opportunities for enhancement with co-polarized urea. This study compared HP pyruvate and ASL perfusion, but it would also be valuable to compare HP pyruvate to dynamic susceptibility contrast (DSC) MR since both these methods use a bolus of contrast agent. While we cannot investigate this comparison in volunteer subjects, we are applying HP pyruvate perfusion in studies with brain tumor patients who receive DSC MR as standard of care.

6.6 Conclusion

Acquiring HP ^{13}C pyruvate metabolic images at high resolution allows for finer spatial delineation of brain structures and can be used to obtain cerebral perfusion parameters. Pyruvate perfusion parameters were positively correlated to proton ASL perfusion values, indicating a relationship between the two perfusion measures. This HP ^{13}C study showed that hyperpolarized pyruvate MRI can be used to assess cerebral metabolism and perfusion within the same study.

6.7 Supplementary Information

Supplementary Figure S6.1. Comparison of pyruvate rCBF from coarse (15 × 15 mm²) and high resolution (7.5 × 7.5 mm²) [1-^{13}C]pyruvate datasets from the same subject. Pyruvate rCBF from coarse resolution images was on average 5% higher than pyruvate rCBF from high resolution images, with the highest differences located near the arteries, veins, and gray matter.

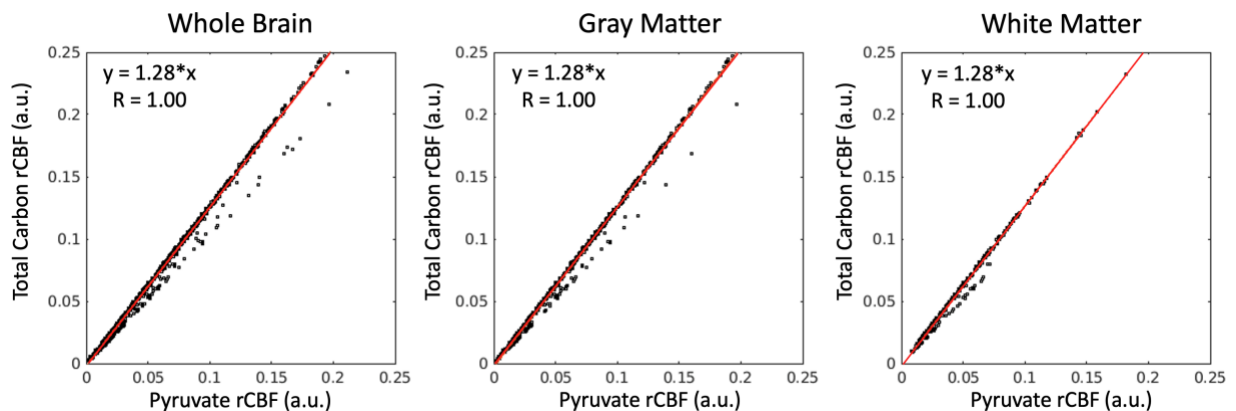**Supplementary Figure S6.2.** Pyruvate rCBF versus total carbon rCBF correlation coefficients and scatterplots for voxels from all subjects (n = 4) acquired at high resolution (n = 5), by respective mask (3006 whole brain, 1162 gray matter, and 575 white matter voxels all from 2 central slices of the brain). Total carbon rCBF was calculated using summed pyruvate, lactate, and bicarbonate images. The linear regression fits are plotted in red. Total carbon rCBF was approximately 1.28 times higher than pyruvate rCBF due to the additional signal contribution from lactate and bicarbonate. Some voxels do not have lactate and bicarbonate signal, so the total carbon and pyruvate rCBF linear relation for those voxels was closer to 1. All units are arbitrary.

References

1. Autry AW, Gordon JW, Chen HY, et al. Characterization of serial hyperpolarized 13C metabolic imaging in patients with glioma. *NeuroImage: Clinical*. 2020;27:102323. doi:10.1016/j.nicl.2020.102323

2. Park I, Larson PEZ, Gordon JW, et al. Development of methods and feasibility of using hyperpolarized carbon-13 imaging data for evaluating brain metabolism in patient studies: Hyperpolarized Carbon-13 Metabolic Imaging of Patients With Brain Tumors. *Magn Reson Med*. 2018;80(3):864-873. doi:10.1002/mrm.27077

3. Miloushev VZ, Granlund KL, Boltyanskiy R, et al. Metabolic Imaging of the Human Brain with Hyperpolarized [13]C Pyruvate Demonstrates [13]C Lactate Production in Brain Tumor Patients. *Cancer Res*. 2018;78(14):3755-3760. doi:10.1158/0008-5472.CAN-18-0221

4. Hackett EP, Pinho MC, Harrison CE, et al. Imaging Acute Metabolic Changes in Patients with Mild Traumatic Brain Injury Using Hyperpolarized [1-13C]Pyruvate. *iScience*. 2020;23(12):101885. doi:10.1016/j.isci.2020.101885

5. Villanueva-Meyer JE, Mabray MC, Cha S. Current Clinical Brain Tumor Imaging. *Neurosurgery*. 2017;81(3):397-415. doi:10.1093/neuros/nyx103

6. Park I, Lupo JM, Nelson SJ. Correlation of Tumor Perfusion Between Carbon-13 Imaging with Hyperpolarized Pyruvate and Dynamic Susceptibility Contrast MRI in Pre-Clinical Model of Glioblastoma. *Mol Imaging Biol*. 2019;21(4):626-632. doi:10.1007/s11307-018-1275-y

7. Fuetterer M, Busch J, Traechtler J, et al. Quantitative myocardial first-pass cardiovascular magnetic resonance perfusion imaging using hyperpolarized [1-13C] pyruvate. *J Cardiovasc Magn Reson*. 2018;20(1):73. doi:10.1186/s12968-018-0495-2

8. Gordon JW, Autry AW, Tang S, et al. A variable resolution approach for improved acquisition of hyperpolarized ^{13}C metabolic MRI. *Magn Reson Med*. 2020;84(6):2943-2952. doi:10.1002/mrm.28421

9. Hu JY, Kim Y, Autry AW, et al. Kinetic analysis of multi-resolution hyperpolarized 13 C human brain MRI to study cerebral metabolism. *Magn Reson Med*. 2022;88(5):2190-2197. doi:10.1002/mrm.29354

10. Gordon JW, Chen HY, Autry A, et al. Translation of Carbon-13 EPI for hyperpolarized MR molecular imaging of prostate and brain cancer patients. *Magn Reson Med*. 2019;81(4):2702-2709. doi:10.1002/mrm.27549

11. Pruessmann KP, Weiger M, Börnert P, Boesiger P. Advances in sensitivity encoding with arbitrary k-space trajectories. *Magn Reson Med*. 2001;46(4):638-651. doi:10.1002/mrm.1241

12. Zhu Z, Zhu X, Ohliger MA, et al. Coil combination methods for multi-channel hyperpolarized 13C imaging data from human studies. *Journal of Magnetic Resonance*. 2019;301:73-79. doi:10.1016/j.jmr.2019.01.015

13. Kim Y, Chen HY, Autry AW, et al. Denoising of hyperpolarized 13 C MR images of the human brain using patch-based higher-order singular value decomposition. *Magn Reson Med*. Published online June 25, 2021. doi:10.1002/mrm.28887

14. Buxton RB, Frank LR, Wong EC, Siewert B, Warach S, Edelman RR. A general kinetic model for quantitative perfusion imaging with arterial spin labeling. *Magnetic Resonance in Medicine*. 1998;40(3):383-396. doi:10.1002/mrm.1910400308

15. Rolls ET, Huang CC, Lin CP, Feng J, Joliot M. Automated anatomical labelling atlas 3. *NeuroImage*. 2020;206:116189. doi:10.1016/j.neuroimage.2019.116189

16. Zhang Y, Brady M, Smith S. Segmentation of brain MR images through a hidden Markov random field model and the expectation-maximization algorithm. *IEEE Trans Med Imaging*. 2001;20(1):45-57. doi:10.1109/42.906424

17. Tustison NJ, Avants BB, Cook PA, et al. N4ITK: improved N3 bias correction. *IEEE Trans Med Imaging*. 2010;29(6):1310-1320. doi:10.1109/TMI.2010.2046908

18. Peruzzo D, Bertoldo A, Zanderigo F, Cobelli C. Automatic selection of arterial input function on dynamic contrast-enhanced MR images. *Computer Methods and Programs in Biomedicine*. 2011;104(3):e148-e157. doi:10.1016/j.cmpb.2011.02.012

19. Johansson E, Månsson S, Wirestam R, et al. Cerebral perfusion assessment by bolus tracking using hyperpolarized 13C. *Magnetic Resonance in Medicine*. 2004;51(3):464-472. doi:10.1002/mrm.20013

20. Mammoli D, Gordon J, Autry A, et al. Kinetic Modeling of Hyperpolarized Carbon-13 Pyruvate Metabolism in the Human Brain. *IEEE Trans Med Imaging*. 2020;39(2):320-327. doi:10.1109/TMI.2019.2926437

21. Fischl B, Dale AM. Measuring the thickness of the human cerebral cortex from magnetic resonance images. *Proceedings of the National Academy of Sciences*. 2000;97(20):11050-11055. doi:10.1073/pnas.200033797

22. Grist JT, McLean MA, Riemer F, et al. Quantifying normal human brain metabolism using hyperpolarized [1–13C]pyruvate and magnetic resonance imaging. *NeuroImage*. 2019;189:171-179. doi:10.1016/j.neuroimage.2019.01.027

23. Lee CY, Soliman H, Geraghty BJ, et al. Lactate topography of the human brain using hyperpolarized 13C-MRI. *NeuroImage*. 2020;204:116202. doi:10.1016/j.neuroimage.2019.116202

24. Goyal MS, Vlassenko AG, Blazey TM, et al. Loss of Brain Aerobic Glycolysis in Normal Human Aging. *Cell Metab*. 2017;26(2):353-360.e3. doi:10.1016/j.cmet.2017.07.010

25. Vaishnavi SN, Vlassenko AG, Rundle MM, Snyder AZ, Mintun MA, Raichle ME. Regional aerobic glycolysis in the human brain. *Proc Natl Acad Sci U S A*. 2010;107(41):17757-17762. doi:10.1073/pnas.1010459107

26. Qin H, Tang S, Riselli AM, et al. Clinical translation of hyperpolarized ^{13}C pyruvate and urea MRI for simultaneous metabolic and perfusion imaging. *Magnetic Resonance in Med*. 2022;87(1):138-149. doi:10.1002/mrm.28965

27. Lau AZ, Miller JJ, Robson MD, Tyler DJ. Simultaneous assessment of cardiac metabolism and perfusion using copolarized [1-^{13}C]pyruvate and ^{13}C-urea. *Magn Reson Med*. 2017;77(1):151-158. doi:10.1002/mrm.26106

28. von Morze C, Larson PEZ, Hu S, et al. Investigating tumor perfusion and metabolism using multiple hyperpolarized (13)C compounds: HP001, pyruvate and urea. *Magn Reson Imaging*. 2012;30(3):305-311. doi:10.1016/j.mri.2011.09.026

29. von Morze C, Larson PEZ, Hu S, et al. Imaging of Blood Flow Using Hyperpolarized [13C]Urea in Preclinical Cancer Models. *J Magn Reson Imaging*. 2011;33(3):692-697. doi:10.1002/jmri.22484

Chapter 7

Further Methods to Improve and Characterize HP MRI Acquisition and Analysis

Jasmine Y Hu, Yaewon Kim, Hsin-Yu Chen, Adam W Autry, Michael A Ohliger, Peder EZ Larson, Daniel B Vigneron, Jeremy W Gordon

7.1 Hyperpolarizer Quality Control Statistics

7.1.1 Background

For HP pyruvate MRI, the hyperpolarized ^{13}C-pyruvate contrast agent needs to be dissolved quickly, under high pressure and high temperature gradients, and checked for quality control criteria before injection into a human. The injection cannot be administered if the dissolution fluid path is blocked or leaking or if the pyruvate dose does not pass quality control (QC). The quality control criteria include pyruvate concentration, polarization percentage, system-measured pH, pH from an external pH strip, and electron paramagnetic agent (EPA) concentration. The EPA concentration needs to be sufficiently low, pyruvate concentration and polarization percentage sufficiently high, and pH readings near neutral to be safe and approved by a pharmacist or doctor for injection. Since pyruvic acid is mixed with a fixed amount of neutralizing buffer, the pyruvate concentration and pH should be correlated.

Historically there have been failures associated with specific fluid path manufacturing lots, and problems with the system-measured quality measures. The goal of this project was to determine what factors affect the success or failure of a dissolution and whether the quality control (QC) system is reporting reasonable values.

7.1.2 Data Summary

The data consists of 424 samples over 3 years. The data can be assumed as normally distributed since there is a large number of samples. What is known before dissolution (predictor variables) are the manufacturing lot numbers for fluid tubes, the loaded channel in the dissolution system, and the time constant and amplitude of the pyruvate signal. What is known after dissolution (response variables) includes success or failure of dissolution and the quality control metrics including pyruvate concentration, EPA concentration, pH, total fluid volume, and the polarization percentage.

7.1.3 Methods

All statistics were computed in R and RStudio (2020, RStudio, PBC, Boston, MA). To determine which factors affect dissolution success, logistic regression was used to estimate the effects of lot numbers, channel numbers, pyruvate time constants, and signal amplitudes on the success or failure of dissolution. The lot numbers and channel numbers are categorical variables and the time constants and signal amplitudes are continuous. The success or failure of dissolution is binary and there are multiple predictor variables, so logistic regression was deemed appropriate for determining which predictors had a significant effect on the response.

Paired scatter plots and linear regression was performed with the QC measurements to judge whether the QC system was reporting reasonable values. It is expected that pyruvate concentration will be negatively correlated with pH since pyruvate is used in an acidic form and that the system-

measured pH and pH strip-pH are positively correlated if the system makes accurate pH measurements. If the linear regression coefficients and scatter plots match up with expectations, then the QC system is reporting reasonable values. The QC measurements are all independent, continuous variables, so multivariate linear regression was considered to be appropriate to compare the effects of multiple measurements on one measurement (pyruvate). The paired scatterplots enabled comparison of variables to each other, not just pyruvate.

7.1.4 Results and Discussion

For performing the logistic regression with dissolution success and all predictors (lot number, channel number, time constant, signal amplitude) none of the predictor variables had a significant effect on the dissolution success. Channel 2 had a 0.06 p-value, which was close to the 0.05 significance cutoff. In comparison with the other predictors the lot numbers had low coefficient values and high p-values, likely due to there being few repetitions of the same lot number (around 30 per lot). Since the lot numbers did not seem to be important in determining the relationship between the dissolution success and the predictors, the regression was performed again without the lot numbers. For this reduced variable regression Channel 2 had a 0.02 p-value and coefficient value of -0.725, so having the pyruvate placed in channel 2 decreased the odds of dissolution success by 50%.

Examining the plot of the QC output measurements in Figure 7.1.1, there is a clear correlation between the two pH readings. The pyruvate concentration seems to have slightly negative correlations with the pH readings. A linear regression confirms these observations, with the polarization percentage and pH readings exhibiting significant effects on the pyruvate concentration. The polarization percentage had a -0.6 effect on pyruvate concentration and the QC system and external strip pH readings had -10 and -6 effects on pyruvate concentration respectively after the

effects from all other variables were removed. The remaining EPA concentration had no effect on

pyruvate concentration. The R squared value was 0.4 for both the non-adjusted and adjusted values.
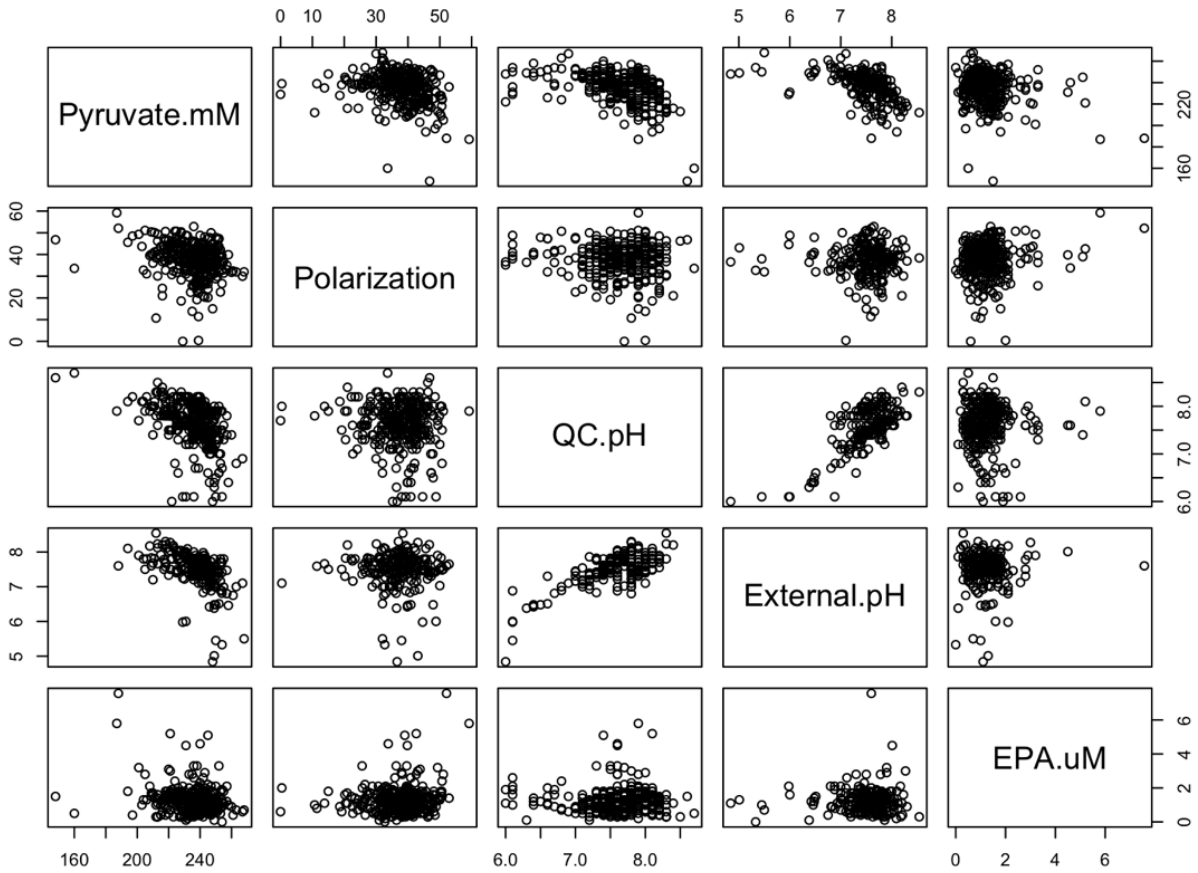
Figure 7.1.1. Matrix scatter plot of pyruvate concentration in mM, polarization percentage, quality control (QC) pH, external pH, and electron paramagenetic agent (EPA) concentration in uM. The pyruvate versus pH graphs have a negative linear correlation and there is positive correlation between the two pH measurements.

Polarization slightly increased (30% to 45%) from 2017 to 2019 and then decreased during 2019

(Figure 7.1.2). Pyruvate concentrations were consistent from 2017 on except for a drop in in the first

half of 2019.
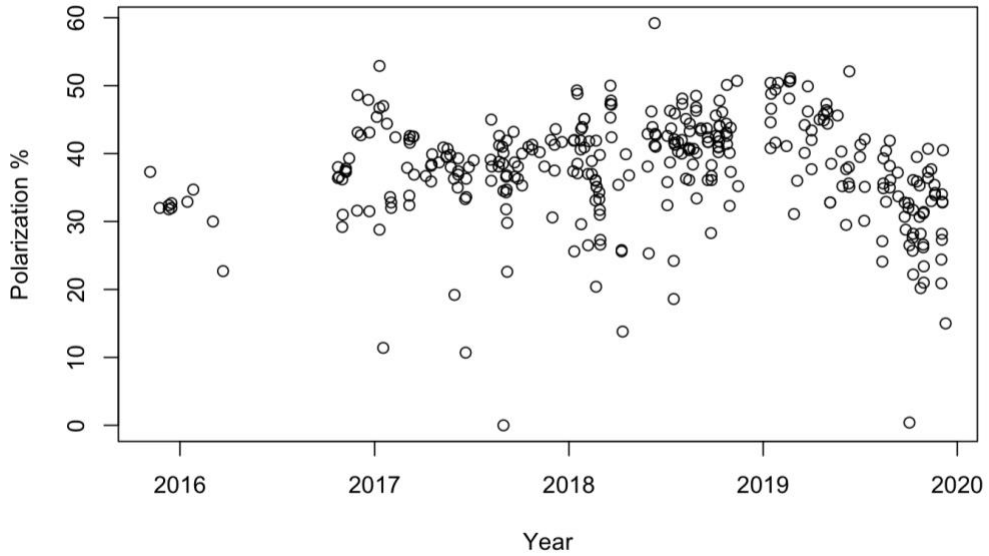
Figure 7.1.2. Polarization percentage over time. Polarization percentages exhibit a positive trend from 2017 to the beginning of 2019, whereafter the polarization has a negative trend.
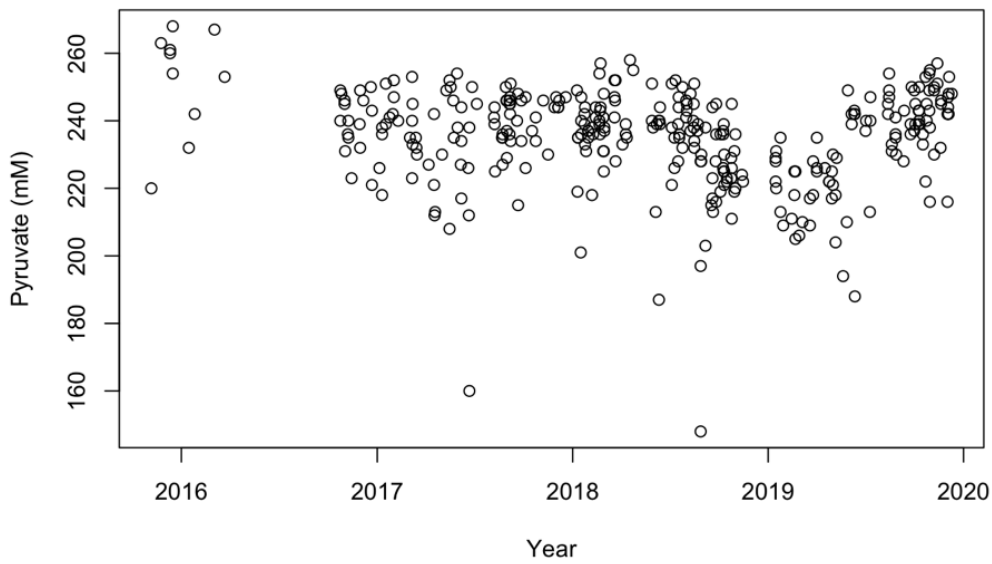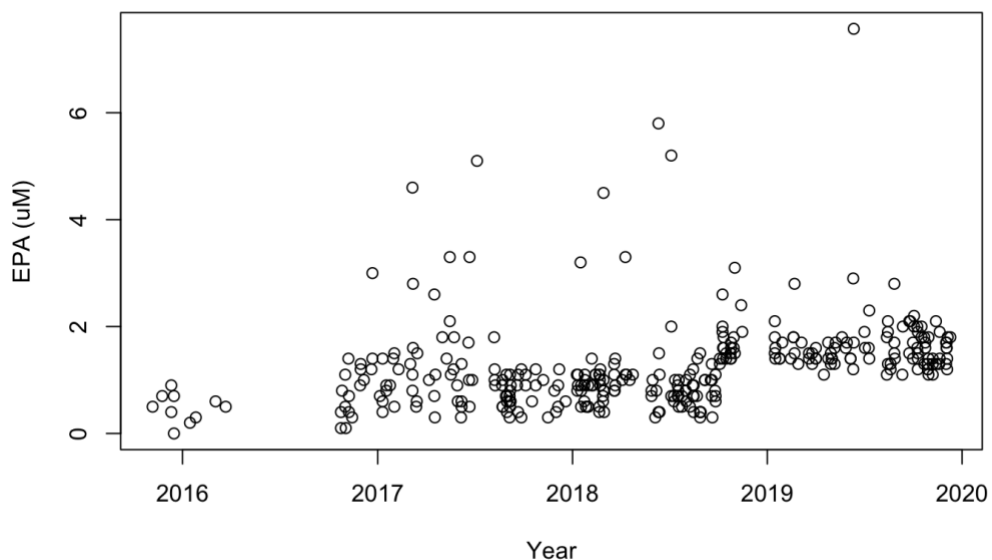

Figure 7.1.3. Pyruvate concentration over time. Pyruvate concentrations stay consistent at around 220-250 mM from 2017-2018, drop in the first part of 2019, and then return to the previous stable range.

pH readings from the QC system and external pH strips were stable over time, with decreasing variability from 2018 on and mean of ~7.5.
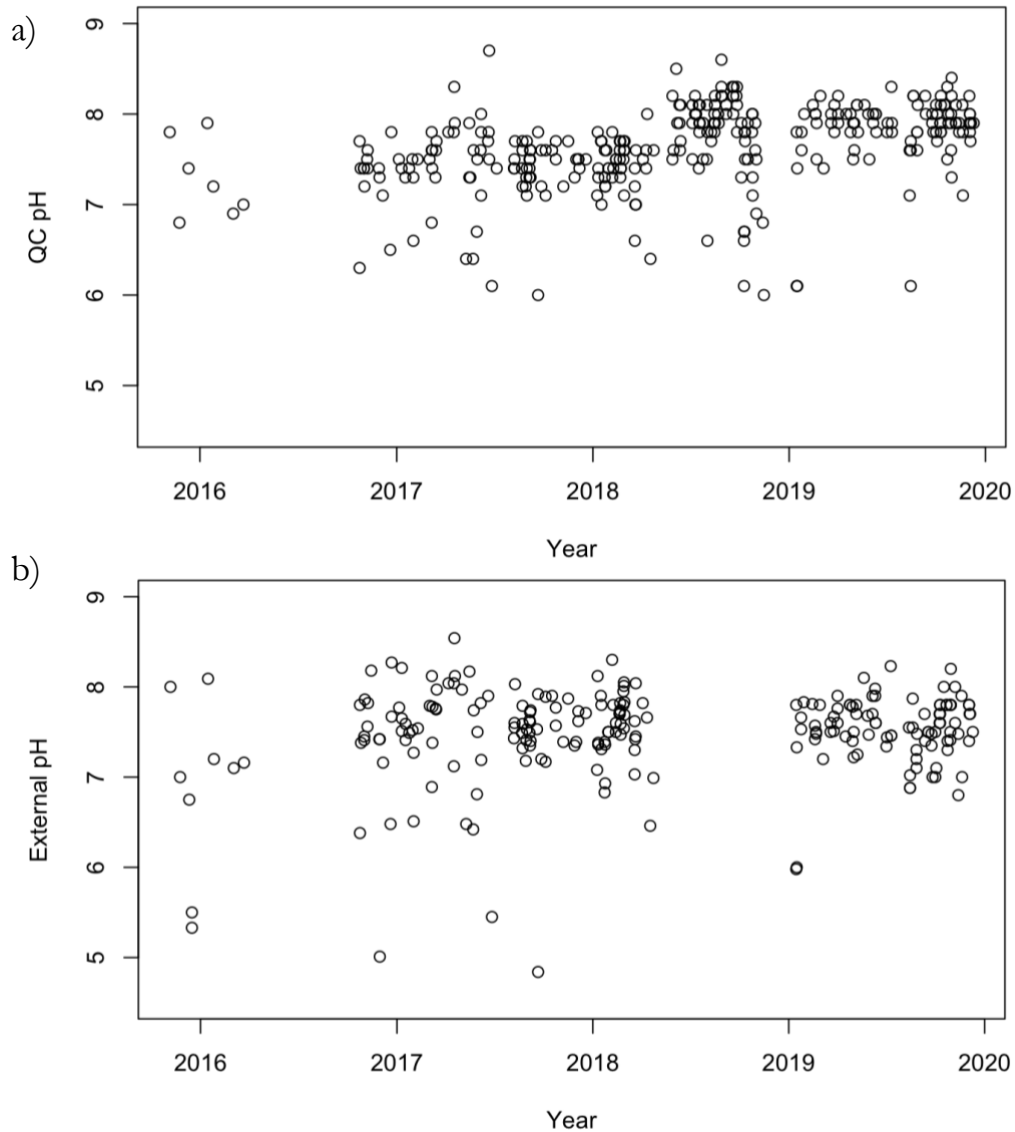
Figure 7.1.4. Two types of pH readings over time. (a) QC pH readings in 2017 were closer to neutral at around 7.5, and the pH readings from late 2018 onwards were more acidic at around 8.0. (b) External pH readings are similar to QC pH readings but with more variability, and readings from the last half of 2018 were missing.

EPA readings were stable from 2017 to 2018 with some high outliers, and in 2019 the mean

concentrations increased to ~1.5 uM.

Figure 7.1.5. Electron paramagnetic agent (EPA) concentration over time. The EPA concentrations were lower in 2017 and 2018 than in 2019.

7.1.5 Conclusion

Contrary to expectations, the lot number did not have a significant effect on the dissolution success. This may have been due to the low number of samples per lot number. However, channel 2 did have a 50% negative effect on the dissolution success. The QC values were reasonable with respect to the expectations that the two pH measurements should match and the pyruvate concentration should be related to the pH value. This analysis did not identify any clear recurring problems with the dissolutions or QC system measurements.

7.2 Spectral-Spatial Pulse Frequency Response Characterization

7.2.1 Introduction

Fast MRI scanning techniques, including echo-planar imaging (EPI), utilize high gradient amplitudes and rapidly switching gradients that can cause discomfort for subjects in the form of peripheral nerve stimulation (PNS). PNS is the excitation of peripheral nerves due to electric voltage induced by rapidly changing magnetic gradients and is commonly perceived as a twitching or tingling sensation in the body usually near the ends of the gradients. Nerve depolarization occurs at a certain threshold based on anatomy, and whether the nerve is depolarized depends on the strength and duration of the electric stimulus. According to Faraday's law, the electric field intensity is proportional to the rate of change of the magnetic gradient field. To reduce PNS, the gradient waveform can be modified to have a slower rate of change or shorter duration.

For the human HP MRI studies discussed in this dissertation, a spectral-spatial (SPSP) pulse and EPI are used for acquisition. The EPI readout gradients cannot be adjusted further at the expense of time or spatial resolution, but there is some remaining flexibility in the SPSP design. Some subjects have reported PNS during HP ^{13}C MRI studies, so Dr. Jeremy Gordon at UCSF designed a new SPSP pulse for human brain studies with shorter duration to reduce PNS. It is important to verify newly designed pulses to ensure the frequency responses match expectations, and to ensure that the pulse does not have unintended effects like excitation of an undesirable molecule. The pyruvic acid used in the injected contrast agent for HP MRI forms pyruvate hydrate in the injection solution[1], but pyruvate hydrate is not metabolically active. The objective of this study was to characterize and

compare the spectral and spatial frequency responses of the old and new SPSP pulses in simulation and phantom data.

7.2.2 Methods

The frequency responses for both SPSP pulses were simulated in MATLAB[2] to examine differences in spatial and spectral profiles. The old and new SPSP pulses were designed for different flip angles and slice thicknesses, so the RF and gradient amplitudes were scaled to match the new pulse. The frequency responses were normalized by their respective maximum values and then plotted on the same frequency axes for comparison. In addition, the frequency responses were simulated at different center frequencies corresponding to pyruvate, lactate, bicarbonate, and alanine and the results were plotted at the pyruvate, lactate, bicarbonate, alanine, and pyruvate hydrate frequencies to check for unwanted overlaps in excitation.

Phantom studies were performed on a 3T MR scanner (MR750, GE Healthcare) using the built in ^{1}H body coil for excitation and an integrated 8 channel ^{1}H/24 channel ^{13}C phased array receiver coil (Rapid Biomedical, Würzburg, Germany). The phantom was a 20 cm diameter sphere containing water. Acquisition was performed with a blipped EPI sequence with a 30° flip angle, 24 × 24 cm field of view, 36 slices with 5 mm thickness, 32 × 32 matrix, 2 s TR, and 13.9 ms TE. The sequence was run a total of 5 times at resonance frequencies shifted from the ^{1}H frequency (0, 40, 80, 120, and 160 ΔHz). Images were reconstructed using sum of squares coil combination and the average phantom signal over all slices at each shifted frequency was compared between the two pulses.

7.2.3 Results and Discussion

In simulation, the respective pulse lengths for the old and new SPSP pulses were 25 and 18 ms respectively. The spatial frequency responses for the two pulses are shown in Figure 7.2.1 and are

nearly identical. Figure 7.2.2 shows the spectral responses for the two pulses, with a wider

bandwidth for the new pulse as compared to the old pulse. A closer view of the spectral responses

also shows that the new pulse has slightly reduced sensitivity at the central frequency compared to

the old pulse.
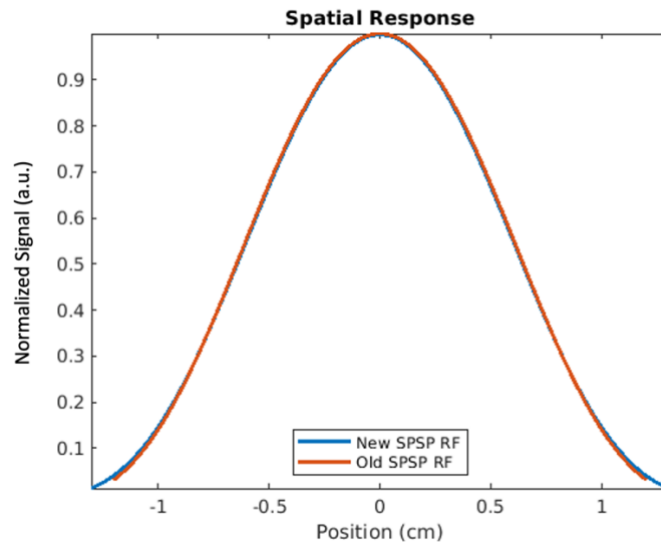
**Figure 7.2.1.** Nearly identical spatial responses of new and old SPSP RF pulses.
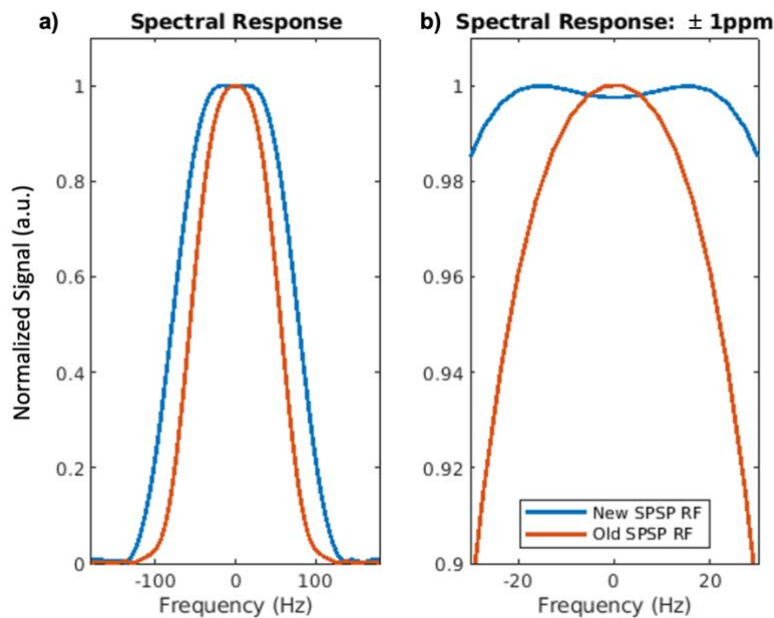
Figure 7.2.2. Spectral responses for two SPSP pulses. Spectral responses for new and old SPSP pulses within (a) 200 Hz and (b) 30 Hz from the center frequency. The new SPSP pulse has a larger bandwidth and slightly reduced sensitivity at the center frequency compared to the old SPSP pulse.

The frequency response for the new SPSP pulse simulated with multiple center frequencies was also plotted at different molecular frequencies as shown in Figure 7.2.3. This matrix shows the expected excitation profile at each relevant molecular frequency and enables the identification of unwanted excitation at metabolite frequencies other than the targeted center frequency. Pyruvate hydrate is partially excited by the SPSP pulses centered at lactate and alanine frequencies, so adjustment of the SPSP pulse is warranted to avoid exciting a molecule not involved in the metabolism under study. Since alanine is not imaged for brain studies due its absence in brain tissue, this pulse could be used for brain imaging after a slight change to avoid the small excitation of pyruvate hydrate during lactate excitation.

The imaging data also exhibits increased bandwidth for the new SPSP pulse by the increased signal intensity at resonance frequencies shifted from the ^{1}H frequency (Figure 7.2.4) and at slices shifted from the center of the phantom (Figure 7.2.5).
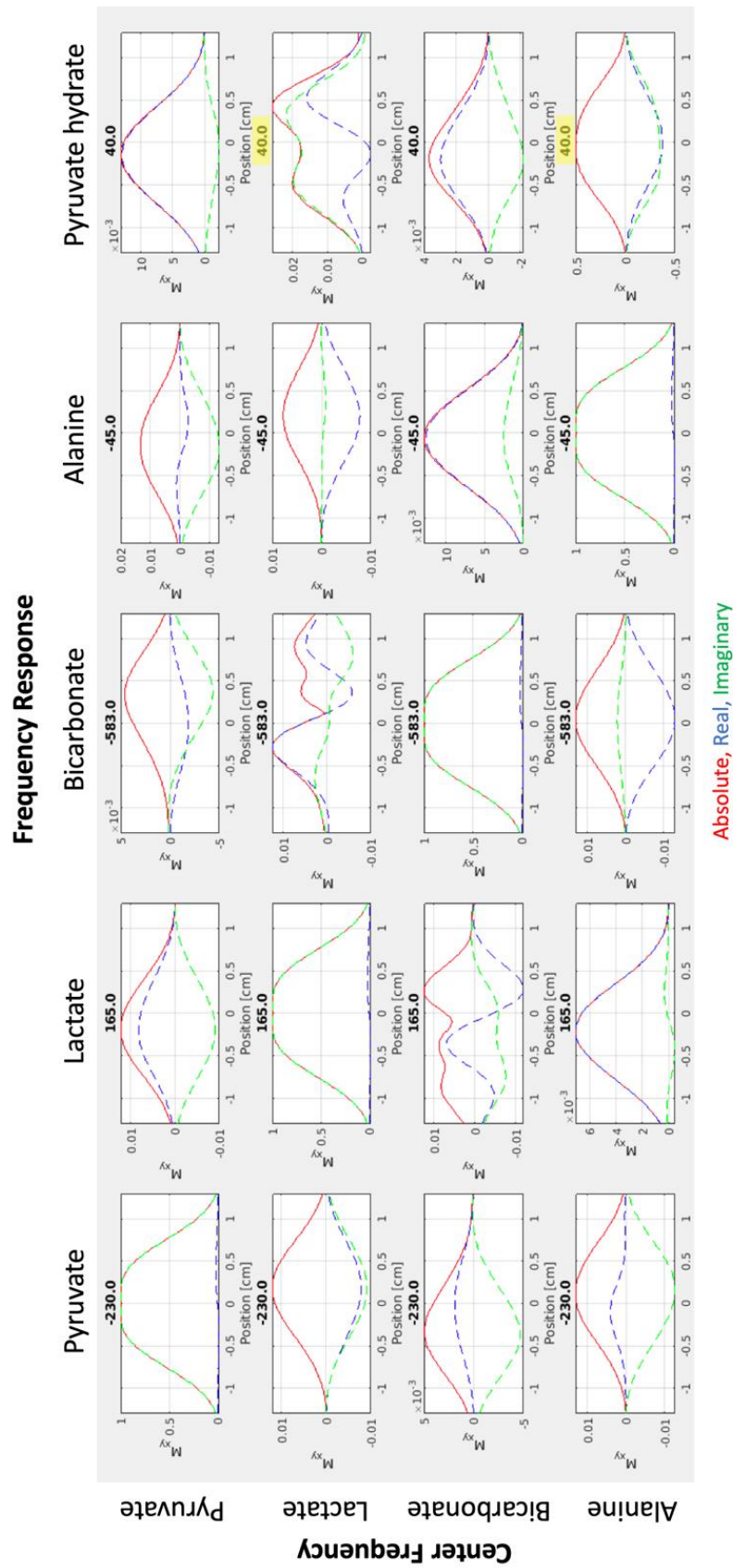
Figure 7.2.3. Matrix of simulated frequency responses for the new SPSP pulse at different molecular frequencies, including pyruvate, lactate, bicarbonate, alanine, and pyruvate hydrate. The major vertical axis indicates which molecular frequency the SPSP pulse is centered at, and the major horizontal axis indicates the frequency response of the SPSP pulse at each molecular frequency. The yellow highlighted plots in the pyruvate hydrate column indicate undesired excitation of pyruvate hydrate when the SPSP pulse is centered at the lactate and alanine frequencies.
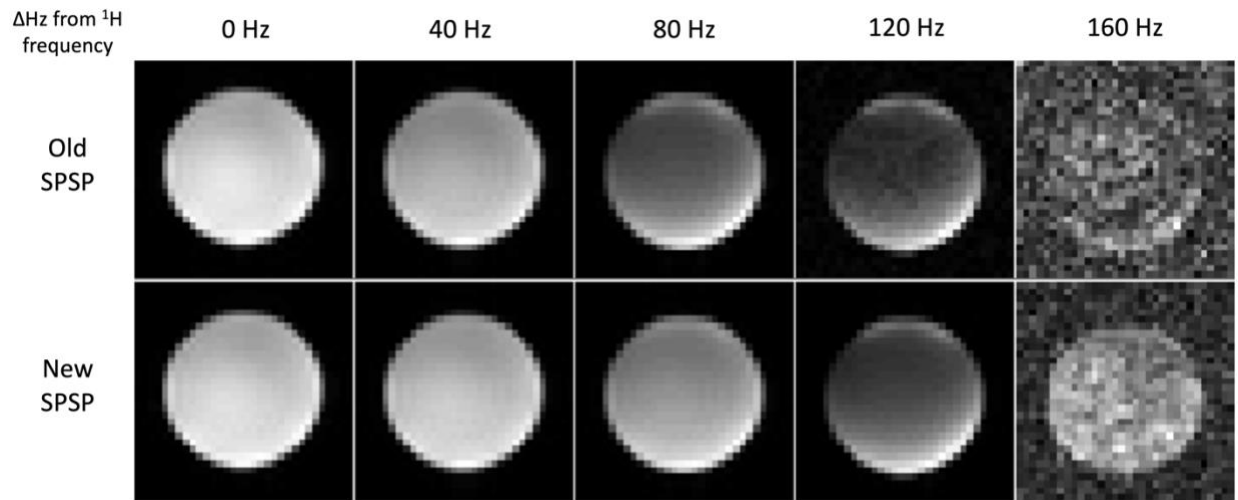
Figure 7.2.4. Center slice of spherical phantom filled with water measured at 0 to 160 Hz off-resonance from the water frequency. Compared to the old spectral-spatial pulse (SPSP), the new SPSP has increased bandwidth as evidenced by increased phantom signal at all shifted frequencies.
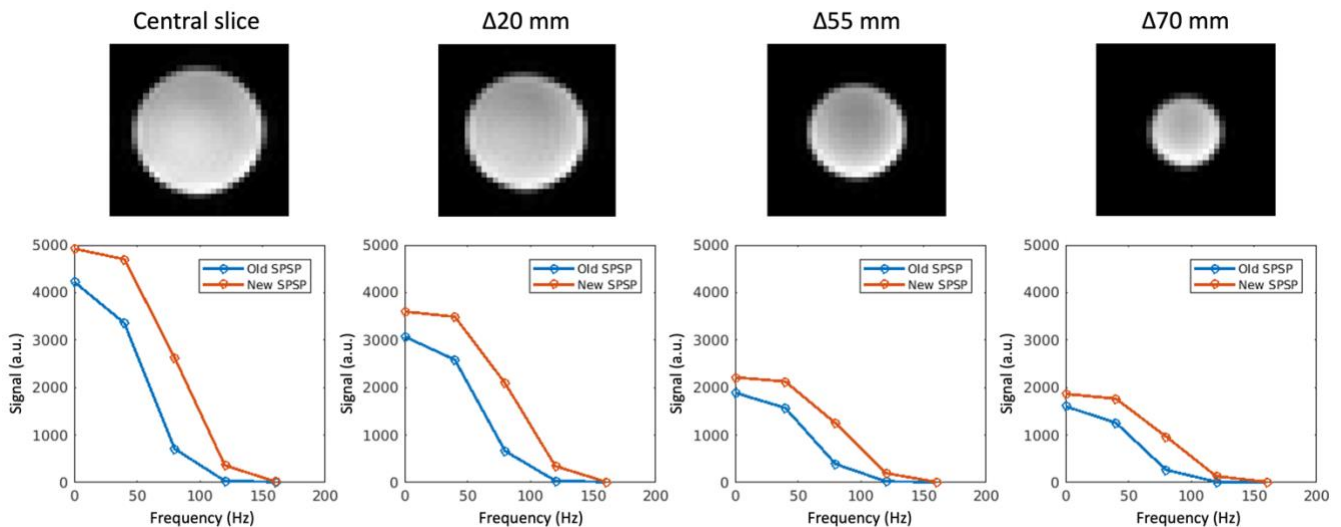
Figure 7.2.5. Reference images and frequency profiles of two SPSP pulses in a spherical water phantom for four slices of increasing distance from the center of the phantom. The new SPSP pulse exhibits higher average signal intensity for all slices as compared to the old SPSP pulse.

Figure 7.2.6 shows the simulated and measured frequency response curves for the two pulses and

verifies that the measured signals match the simulated responses.
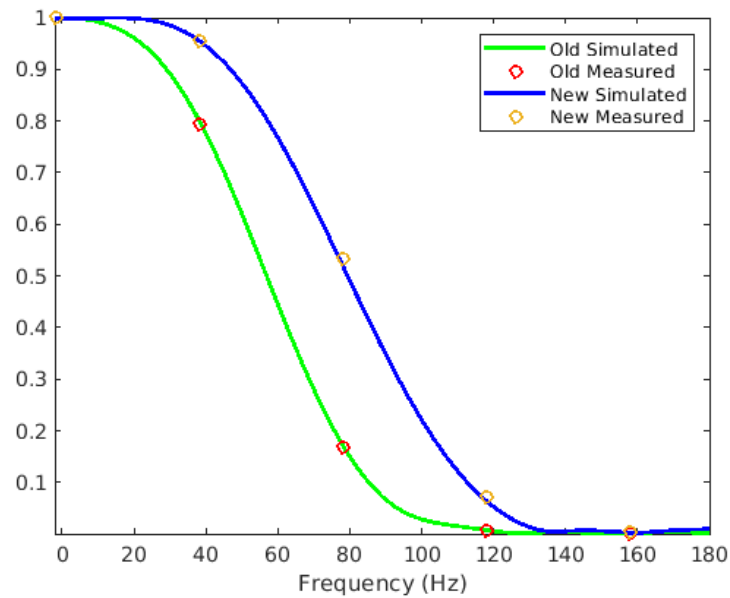
Figure 7.2.6. Simulated frequency response curves and measured values of old and new spectral-spatial pulses (SPSP). The new SPSP pulse has wider spectral frequency bandwidth than the old SPSP pulse in both simulation and phantom measurement.

7.2.4 Conclusion

The newly designed SPSP pulse has increased spectral bandwidth and reduced duration as verified in simulation and phantom imaging, which was designed to maintain the spatial excitation profile for HP MRI and reduce the PNS experienced by study subjects. Slight adjustment of the pulse is needed to ensure that non-target molecules are not excited when the pulse is centered at desired metabolite frequencies.

# 7.3 Effects of Sensitivity Map Interpolation on Reconstruction

7.3.1 Introduction

After hyperpolarized magnetic resonance imaging (HP MRI) is acquired, the raw data needs to be reconstructed from multiple coil channels, and in the case of multi-resolution imaging, multiple fields of view (FOV). To optimally combine the signal from multiple coils, coil sensitivity maps are used in the reconstruction process. Coil sensitivity maps represent the distribution of spatial magnetic field generated by each powered coil[1]. The coil's magnetic field depends on the composition of biological tissue near the coil, so coil sensitivity maps are usually derived using acquired MRI data. For multi-resolution HP MRI, sensitivity maps are generated from the pyruvate images (7.5 × 7.5 mm², 240 × 240 mm² FOV) and interpolated to match the lactate and bicarbonate images (15 × 15 mm², 480 × 480 mm² FOV)[2,3]. There are different methods and orders of processing that could affect the quality of the final sensitivity maps, including using convolution with an averaging filter, bicubic or nearest neighbor methods for interpolation, and interpolating before versus after sensitivity map generation. These sensitivity maps have a direct impact on the signal to noise ratio (SNR) of the reconstructed images, so it is important to verify which processing routine produces good quality images with high SNR. The objective of this study was to experiment with different sensitivity map interpolation methods and orders of processing to identify which routine produces the highest SNR images.

7.3.2 Methods

Sensitivity maps were generated and applied to three multi-resolution HP MRI EPI studies from Chapter 4. Pyruvate images were acquired with 7.5 × 7.5 × 15 mm³ resolution, 32 × 32 matrix size,

and 240 × 240 mm^2 FOV; lactate and bicarbonate images were acquired with 15 × 15 × 15 mm^3 resolution, 32 × 32 matrix size, and 480 × 480 mm^2 FOV. First the raw HP pyruvate MRI data was prewhitened to optimally weight the data from each coil element based on the ratio of signal to the square of the noise[4]. Then prewhitened pyruvate data was convolved with a 3 × 3 averaging filter of ones for a dataset referred to as averaged pyruvate. Using either the prewhitened raw pyruvate or averaged pyruvate data and either bicubic or nearest neighbor interpolation, the two methods (Pre-process and Post-process) outlined in Figure 7.3.1 were used to generate eight sets of sensitivity maps for lactate and bicarbonate coil combination. For pyruvate coil combination, two sets of sensitivity maps were generated using either raw or averaged pyruvate images.
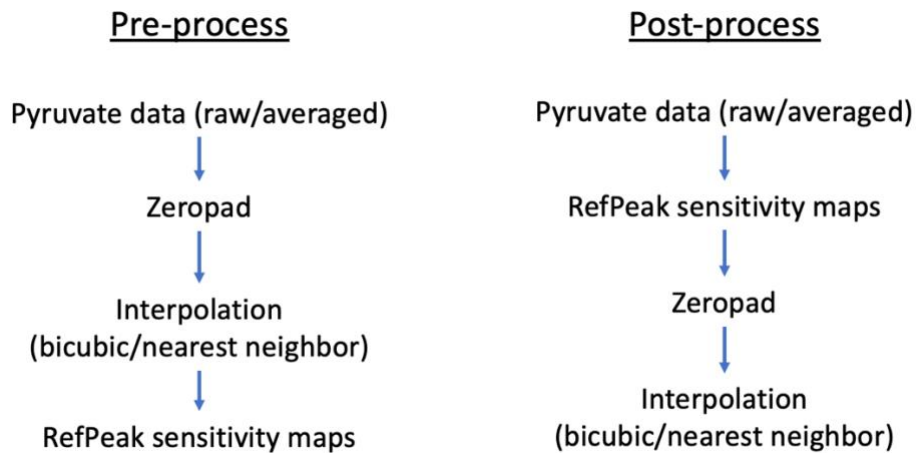

Figure 7.3.1. Flowchart for two methods of processing steps to obtain sensitivity maps for metabolites acquired at multiple resolutions.

After coil-combination, the lactate and bicarbonate images were cropped to the pyruvate FOV. Area-under-curve (AUC) maps were calculated by summing the images over the time dimension. Signal to noise ratio (SNR) maps were calculated by dividing the AUC maps with the standard deviation of a noise-only image from the last timepoint and most superior slice. Maximum SNR values were calculated from three slices centered on the brain for each subject.

7.3.3 Results and Discussion

Sensitivity maps generated from raw HP pyruvate MRI data using either the Pre-process or Post-process method are shown in Figure 7.3.2. For all the slices and coil elements displayed, the Pre-process sensitivity maps exhibit higher noise than the Post-process sensitivity maps. The elevated noise levels are also apparent in the scatterplots from Figure 7.3.3, which show sensitivity map voxel values from inside and outside a brain mask. The higher noise levels also increased the sensitivity map voxel values inside the brain mask.
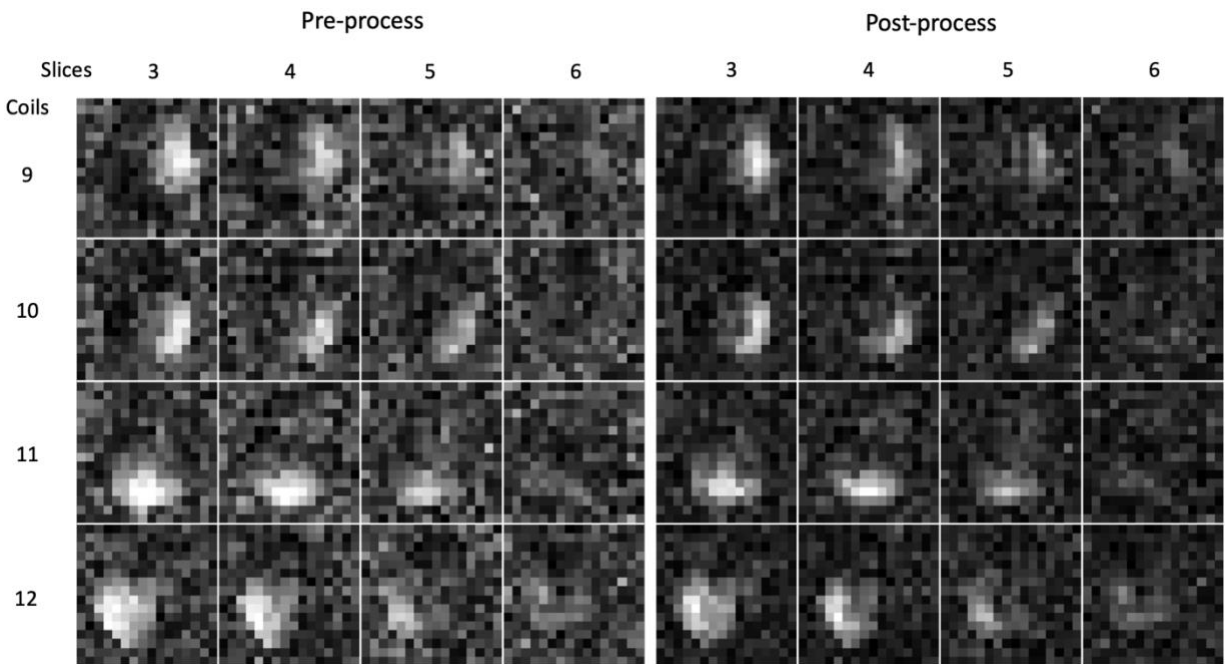
Figure 7.3.2. Sensitivity maps from raw HP pyruvate MRI obtained using either the Pre-process or Post-process method. The Pre-process sensitivity maps have higher noise and signal compared to the Post-process sensitivity maps.

The sensitivity maps generated from either raw or averaged pyruvate have a similar trend in that the raw pyruvate sensitivity maps have higher signal and noise values, which resulted in increased overall voxel values in the coil-combined pyruvate images shown in Figure 7.3.4.
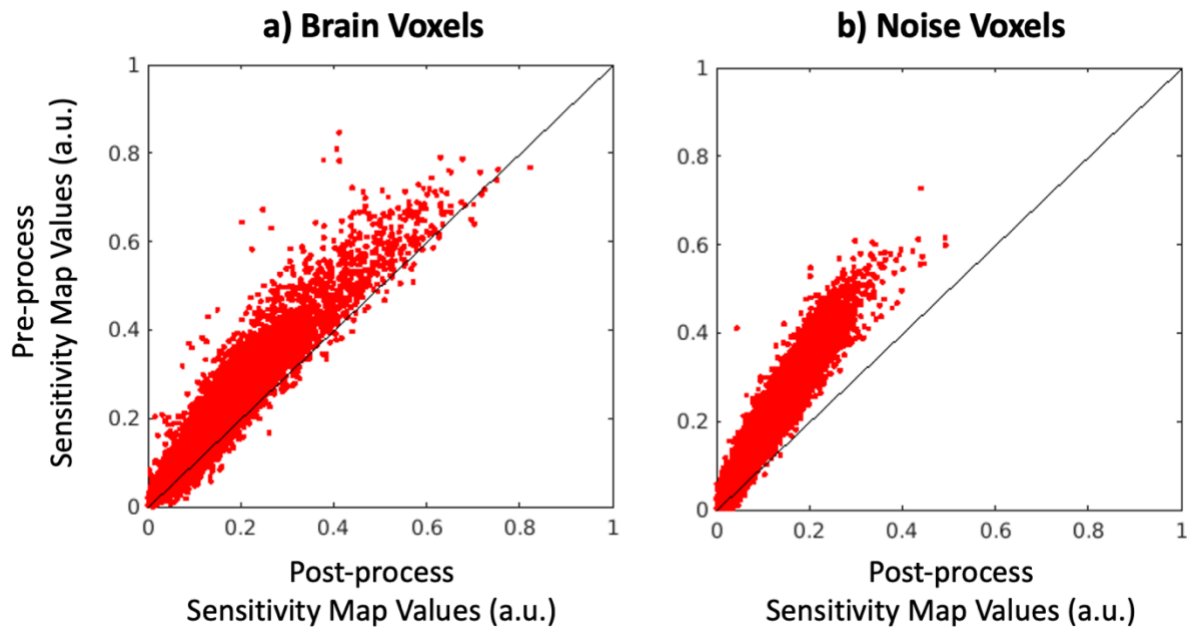
**Figure 7.3.3.** Scatterplots of sensitivity map values from raw pyruvate Pre-process or Post-process methods in (a) brain signal voxels and (b) noise voxels from a representative study. Higher noise was observed for the Pre-process method than the Post-process method, which accounts for the bias in brain voxel values between methods. All units are arbitrary.
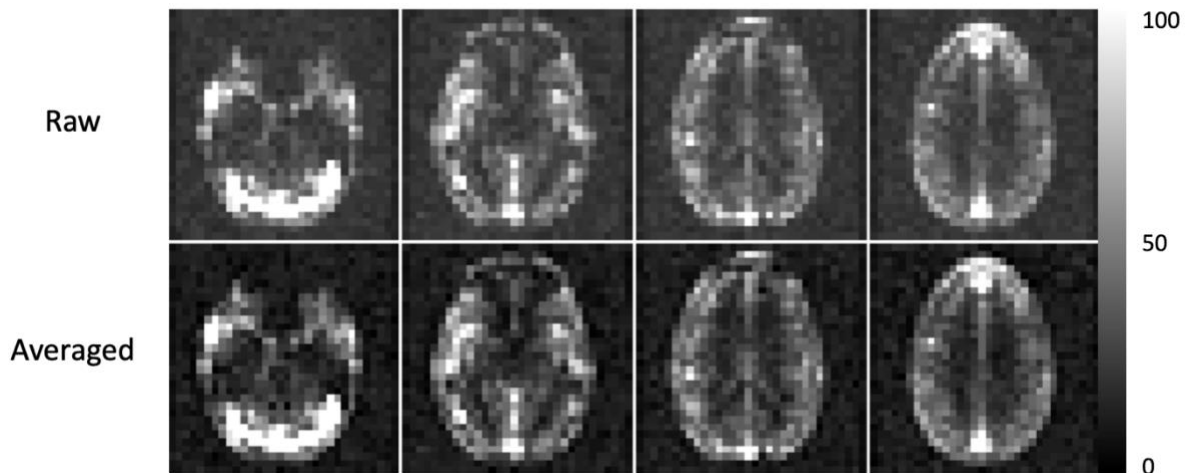

Figure 7.3.4. Area under curve (AUC) maps for pyruvate images coil-combined using sensitivity maps from a representative study. Slightly higher apparent signal and noise was observed for pyruvate images coil-combined using raw pyruvate sensitivity maps versus averaged pyruvate sensitivity maps. Units are arbitrary.
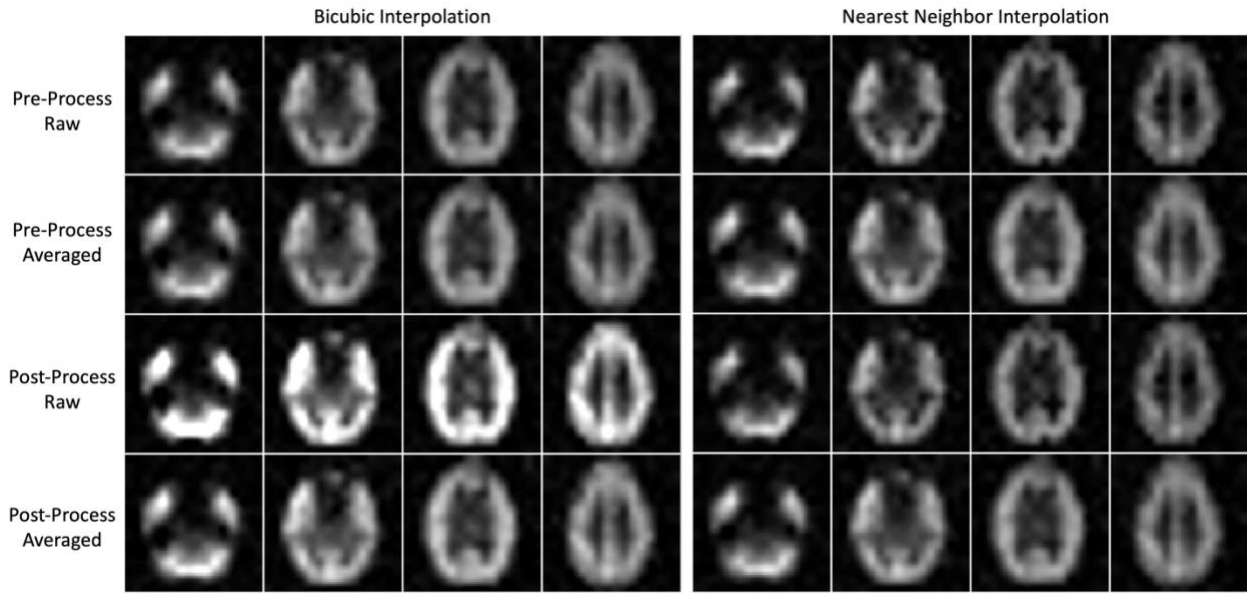
Figure 7.3.5. Lactate SNR maps for multiple sensitivity map generation methods and interpolation methods. Lactate images were coil-combined using the eight different sensitivity maps, then zerofilled four times for display.
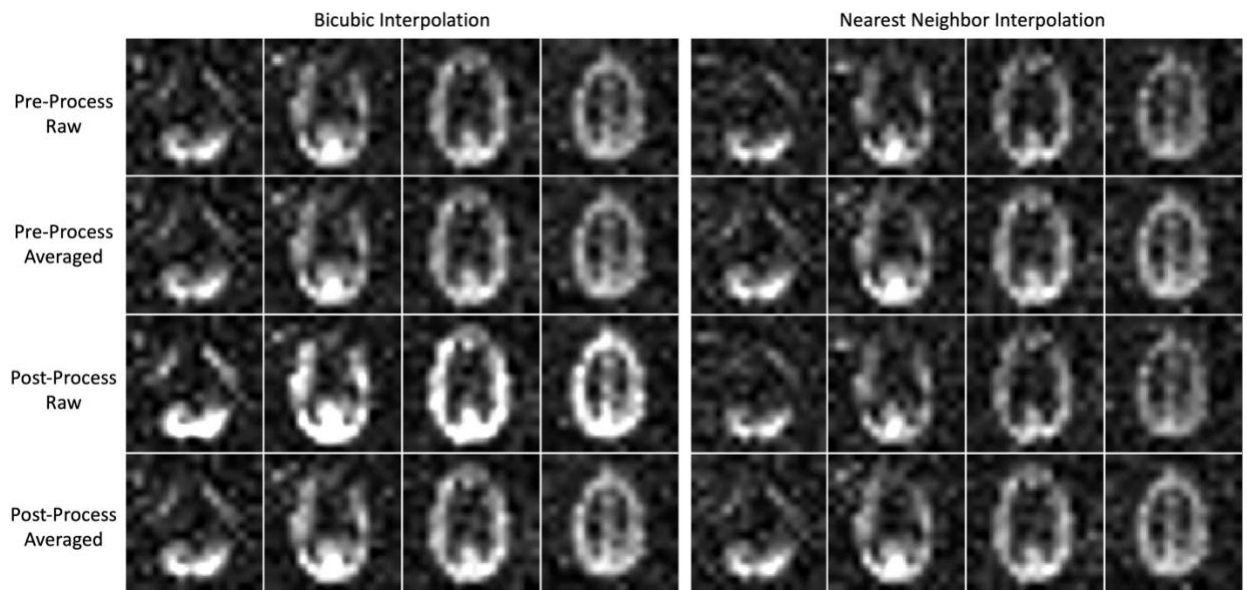
Figure 7.3.6. Bicarbonate SNR maps for multiple sensitivity map generation methods and interpolation methods. Bicarbonate images were coil-combined using the eight different sensitivity maps, then zerofilled four times for display.

The signal and noise levels of sensitivity maps directly affects the signal to noise ratio (SNR) of the coil-combined images, so it is important to generate sensitivity maps with high SNR to conserve the signal in the acquired images. Figures 7.3.5 and 7.3.6 show lactate and bicarbonate SNR maps after

coil combination using the eight different sets of sensitivity maps. Bicubic interpolation produces

higher SNR maps than nearest neighbor interpolation, which is most apparent in the lower SNR

bicarbonate maps. The Post-process method, using raw pyruvate images and bicubic interpolation,

produces the highest mean SNR lactate and bicarbonate images out of all the other sensitivity maps

as shown in Table 7.3. For pyruvate images, the highest mean SNR was obtained using averaged

pyruvate sensitivity maps.

Table 7.3. Average and standard deviation of maximum SNR from three HP MRI studies for various sensitivity map and interpolation methods.

	Bicubic	Nearest Neighbor
Lactate		
Pre-process		
Raw	16.6 ± 6.3	16.4 ± 5.8
Averaged	16.9 ± 6.5	17.1 ± 6.5
Post-process		
Raw	28.4 ± 9.7	16.4 ± 5.8
Averaged	19.5 ± 7.2	17.1 ± 6.5
Bicarbonate		
Pre-process		
Raw	6.9 ± 2.7	6.8 ± 2.8
Averaged	7.0 ± 2.9	7.2 ± 2.9
Post-process		
Raw	10.6 ± 3.8	6.8 ± 2.8
Averaged	7.8 ± 2.9	7.2 ± 2.9
Pyruvate		
Raw	190 ± 86	
Averaged	222 ± 104	

7.3.4 Conclusion

The sensitivity map method that produced lactate and bicarbonate images with the highest SNR was

the Post-process method, which uses zero padded and interpolated sensitivity maps. Zero padding

and interpolation of the sensitivity maps, rather than zero padding and interpolating the pyruvate

images before sensitivity map generation, conserved the most lactate and bicarbonate signal and

minimized noise. Using raw pyruvate images as input to the sensitivity map generation and bicubic

interpolation produced the highest SNR lactate and bicarbonate images as compared to averaged

pyruvate input and nearest neighbor interpolation.

References

Section 7.2

1. Golman, K., in 't Zandt, R., & Thaning, M. (2006). Real-time metabolic imaging. *Proceedings of the National Academy of Sciences*, 103(30), 11270-11275.

2. MATLAB. (2021). Version 9.10.0.2015706 (R2021a). Natick, Massachusetts: The MathWorks Inc.

Section 7.3

1. Hoult, D. I., & Lauterbur, P. C. (1979). The sensitivity of the zeugmatographic experiment involving human samples. *Journal of Magnetic Resonance* (1969), 34(2), 425-433.

2. Zhu, Z., Zhu, X., Ohliger, M. A., Tang, S., Cao, P., Carvajal, L., ... & Gordon, J. W. (2019). Coil combination methods for multi-channel hyperpolarized 13C imaging data from human studies. *Journal of Magnetic Resonance*, *301*, 73-79.

3. Gordon, J. W., Autry, A. W., Tang, S., Graham, J. Y., Bok, R. A., Zhu, X., ... & Larson, P. E. (2020). A variable resolution approach for improved acquisition of hyperpolarized 13C metabolic MRI. *Magnetic resonance in medicine*, *84*(6), 2943-2952.

4. Hall, E. L., Stephenson, M. C., Price, D., & Morris, P. G. (2014). Methodology for improved detection of low concentration metabolites in MRS: optimised combination of signals from multi-element coil arrays. *Neuroimage,* 86, 35-42.

Publishing Agreement

It is the policy of the University to encourage open access and broad distribution of all theses, dissertations, and manuscripts. The Graduate Division will facilitate the distribution of UCSF theses, dissertations, and manuscripts to the UCSF Library for open access and distribution. UCSF will make such theses, dissertations, and manuscripts accessible to the public and will take reasonable steps to preserve these works in perpetuity.

I hereby grant the non-exclusive, perpetual right to The Regents of the University of California to reproduce, publicly display, distribute, preserve, and publish copies of my thesis, dissertation, or manuscript in any form or media, now existing or later derived, including access online for teaching, research, and public service purposes.

DocuSigned by:

Jasmine Hu

8E02FF4B764144D...

Author Signature

3/13/2023

Date